Measurement of the smallest neutrino mixing angle using reactor antineutrino events with neutron capture on hydrogen at RENO

Sang Yong KIM

Under the supervision of
Professor Jonghee Yoo

A Dissertation submitted to the Graduate
Faculty of Seoul National University
in partial fulfillment of the requirement
for the Degree of Doctor of Philosophy

Department of Physics and Astronomy
Graduate School of Natural Science
Seoul National University
Seoul, KOREA

August 2022

Measurement of the smallest neutrino mixing angle using reactor antineutrino events with neutron capture on hydrogen at RENO

지도교수 유 종 희

이 논문을 이학 박사 학위논문으로 제출함

2022년 8월

서울대학교 대학원

물리 천문 학부

김 상 용

김상용의 박사 학위논문을 인준함

2022년 8월

위 원 장	양 운 기	(인)
부 위 원 장	유 종 희	(인)
위 원	김 선 기	(인)
위 원	정 성 훈	(인)
위 원	유 인 태	(인)

Abstract

The reactor experiment for neutrino oscillation (RENO) has successfully measured the smallest neutrino mixing angle theta13 using reactor electron antineutrino ($\bar{\nu}_e$) from Hanbit nuclear power plant at Yonggwang in Korea. We have been collecting data using two identical near and far detectors since August 2011. The identical detectors are essential to significantly reducing systematic uncertainty of the absolute reactor neutrino flux. Each RENO detector consists of four layers of cylindrical vessels with different liquids. They are the target, gamma-catcher, buffer, and veto components from the innermost. The reactor antineutrinos interact with free protons in the liquid scintillator and produce a positron and a neutron via the inverse beta decay (IBD) process. The positron is detected immediately as a prompt signal, and the neutron is thermalized and captured by Hydrogen (H) or Gadolinium(Gd) as a delayed signal. Because of high environmental radioactivity below 3.5 MeV, the neutron captures on H(n-H) emitting a 2.2 MeV γ-ray are hardly detected, while the neutron captures on Gd(n-Gd) producing a few γ-rays with a total energy of $\sim$8 MeV are rather free from the ambient background. Due to the sufficient statistics of collected n-H data equivalent to the n-Gd data, we have successfully measured the neutrino mixing angle θ_{13} as well. An improved analysis was performed to extract the n-H IBD signal of reactor antineutrinos against high backgrounds. The independent measurement of θ_{13} using the n-H data sample provides a systematic cross-check of the n-Gd result. Based on a rate-only analysis, we obtain $\sin^2 2\theta_{13} = 0.086 \pm 0.006(\text{stat.}) \pm 0.010(\text{syst.})$. This thesis reports the results of θ_{13} measurement using 2900 days of n-H data at RENO.

Contents

List of Figures

List of Tables

Chapter 1

Introduction

In the last 100 years, impressive achievements have been made in the neutrino sector, from postulating their existence to the discovery of neutrino oscillations. In particular, the neutrino oscillation indicates the existence of neutrino mass and opens a window to new physics beyond the Standard Model (SM). This requires modification of SM and understanding the mechanism of their extremely small masses. Neutrino oscillation will provide a valuable means of exploring new physics in the Grand Unification scale as well as understanding the flavor dynamics and extra dimensions.

1.1 Overview

Neutrino oscillation is a flavor transformation from one lepton type to another type. The current Standard Model cannot explain the neutrino mixing phenomenon because mixing is only possible between neutrinos of nonzero masses. The neutrino oscillation is the consequence of the neutrino flavor being a linear combination of the mass eigenstates. Thus neutrino oscillation provides motivation for revision of the current Standard Model. A framework of three flavors(ν_e, ν_μ, ν_τ) is the basic model describing neutrino mixing phenomenon. Current neutrino mixing paradigm can be expressed by three mixing angles (θ_{12}, θ_{23}, θ_{13}), three mass differences (Δm^2_{21}, Δm^2_{31}, and Δm^2_{32}), and one phase (δ_{CP}) [1, 2]. International experimental programs are underway to make precision measurements of neutrino oscillation parameters. The mixing angle θ_{12} is well measured by solar neutrino experiments [3, 4, 5] and a reactor neutrino experiment [6, 7]. The mixing angle θ_{23} is less precisely measured by atmospheric neutrino experiments [8, 9, 10], long-baseline accelerator experiments [11, 12, 13], and reactor experiments [14, 15, 16]. Both angles are relatively large compared to the mixing angles in the quark sector.

In 1998, the Super-Kamiokande experiment discovered neutrino oscillation and mixing angle θ_{23} [3]. The interesting thing is that angle θ_{23} is close to the maximal value. The Sudbury Neutrino Observatory (SNO) discovered solar neutrino oscillation in 2001, and the mixing angle θ_{12} was obtained [4, 17]. The remained unknown last angle, the smallest mixing angle θ_{13}, was found in the RENO, Daya Bay, and Double Chooz experiments from the disappearance of the electron antineutrino from the reactor [15, 14, 16]. These reactor neutrino experiments have the advantages of measuring θ_{13} due to insignificant matter effects and unnecessary beam facility construction. The RENO Collaboration made the first measurement of θ_{13} based on a far-to-near ratio in 2012 [15] and a more precise measurement of both θ_{13} and $|\Delta m^2_{ee}|$, a mixture of $|\Delta m^2_{31}|$ and $|\Delta m^2_{32}|$, obtained from energy- and baseline-dependent disappearance in 2016 [18] and 2018 [19]. This thesis presents an independent measurement of θ_{13} using reactor neutrino events with neutron capture on Hydrogen (n-H) based on 2900 days of data. This measurement obtains a θ_{13} value of $\sin^2(2\theta_{13}) = 0.086 \pm 0.006(stat.) \pm 0.010(syst.)$ which is in good agreement with the previous n-Gd data measurements.

1.2 Neutrino Oscillations

A neutrino flavor α is a combination of different mass eigenstates as given by

$$|\nu_\alpha\rangle = \sum_i U^*_{\alpha i} |\nu_i\rangle \tag{1.1}$$

where the mass eigenstates are also Hamiltonian eigenstates. Therefore, the neutrino evolution in time is described by

$$|\nu_\alpha(t)\rangle = \sum_i U^*_{\alpha i} e^{-iE_i t} |\nu_i\rangle \tag{1.2}$$

A flavor eigenstate at a time can be expressed in terms of all flavor eigenstates.

$$|\nu_\alpha(t)\rangle = \sum_{\beta=e,\mu,\tau} U^*_{\alpha i} e^{-iE_i t} U_{\beta i} |\nu_\beta\rangle \tag{1.3}$$

Therefore, the transition probability of ν_α to ν_β $(\alpha, \beta = e, \mu, \tau)$ with an energy of E after traversing a distance L in vacuum can be calculated as follows:

$$P(\nu_\alpha \to \nu_\beta) = \delta_{\alpha\beta} - 2\mathrm{Re}\sum_{j>i} U_{\alpha i} U^*_{\alpha j} U^*_{\beta i} U_{\beta j} \left(1 - \exp\left\{ i\Delta m^2_{ji} L \frac{2}{E} \right\}\right), \tag{1.4}$$

where $\Delta m^2_{ji} \equiv m^2_j - m^2_i$ is the neutrino mass squared difference. If three flavor eigenstates exist, the matrix U is given U is described by a 3×3 matrix. As the

quark flavor mixing is described by the Cabibbo-Kobayashi-Maskawa (CKM) matrix [20], the three neutrino flavor mixing can be parametrized by the Pontecorvo-Maki-Nakagawa-Sakata (PMNS) matrix [21].

$$U = \begin{pmatrix} 1 & 0 & 0 \\ 0 & c_{23} & s_{23} \\ 1 & -s_{23} & c_{23} \end{pmatrix} \begin{pmatrix} c_{13} & 0 & s_{13}e^{i\delta} \\ 0 & 1 & 0 \\ -s_{13}e^{-i\delta} & 0 & c_{13} \end{pmatrix} \begin{pmatrix} c_{12} & s_{12} & 0 \\ -s_{12} & c_{12} & 0 \\ 0 & 0 & 1 \end{pmatrix} \quad (1.5)$$

$$= \begin{pmatrix} c_{12}c_{13} & s_{12}c_{13} & s_{13}e^{-i\delta} \\ -s_{12}c_{23} - c_{12}s_{23}s_{13}e^{i\delta} & c_{12}c_{23} - s_{12}s_{23}s_{13}e^{i\delta} & s_{23}c_{13} \\ s_{12}s_{23} - c_{12}c_{23}s_{13}e^{i\delta} & -c_{12}s_{23} - s_{12}c_{23}s_{13}e^{i\delta} & c_{23}c_{13} \end{pmatrix},$$

where $c_{ij} = \cos\theta_{ij}$, $s_{ij} = \sin\theta_{ij}$, θ_{ij} is a mixing angle, and δ is a Dirac CP violating phase. Several international experimental programs using solar, atmospheric, reactor, and accelerator neutrinos have reported oscillations among different flavors of neutrinos, providing prosperous information on the flavor structure of the lepton sector. The current best values of neutrino oscillation parameters with an error of one standard deviation (1σ) are summarized as follows [22]:

$$\begin{aligned} \sin^2\theta_{23} &= 0.545 \pm 0.021 \text{ (normal)} \quad (1.6) \\ &\text{or } 0.547 \pm 0.021 \text{ (inverted)} \\ \sin^2\theta_{12} &= 0.307^{+0.013}_{-0.012} \\ \sin^2\theta_{13} &= (2.18 \pm 0.07) \times 10^{-2} \\ \Delta m^2_{32} &= (2.453 \pm 0.034) \times 10^{-3}\text{eV}^2 \text{ (normal)} \\ &\text{or } (-2.546^{+0.034}_{-0.040}) \times 10^{-3}\text{eV}^2 \text{ (inverted)} \\ \Delta m^2_{21} &= (7.53 \pm 0.18) \times 10^{-5}\text{eV}^2 \end{aligned}$$

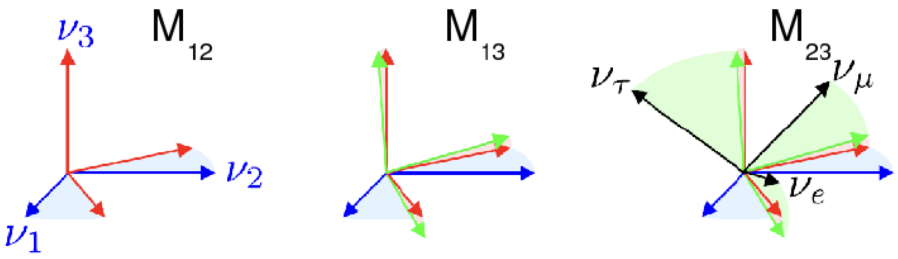

Figure 1.1: A schematic picture of neutrino mixing angles. Neutrino mixing angles are defined as the angles between axes of flavor eigenstates(ν_e, ν_μ and ν_τ) and mass eigenstates(ν_1, ν_2 and ν_3) [23].

Experiment	Year	Reactor Power (MW_{th})	Baselines (m)	N_{obs} $/N_{exp}$
ILL [25]	1980-1981	57	8.8	0.96 ± 0.12
Goesgen [26, 27, 28]	1981-1985	2800	37.9	1.02
			45.9	1.05 ± 0.06
			64.7	0.98 ± 0.06
Rovno [29, 30, 31]	1983-1991	1375	18, 25	0.964 ± 0.07
Krasnoyarsk [32]	1987-1994	-	57,231	0.99 ± 0.05
Bugey [33]	1995	2800	15	0.99 ± 0.05
			40	0.99 ± 0.05
			95	0.92 ± 0.14
Chooz [34]	1997	8500	1000	1.01 ± 0.04
Palo Verde [35, 36]	1999	11600	890, 750	1.01 ± 0.10
RENO [15, 37]	2012	16400	294, 1383	0.941 ± 0.015
Daya Bay [14, 38]	2012	17400	560, 1640	0.940 ± 0.011
Double Chooz [16, 39]	2013	8500	400, 1050	0.925 ± 0.012

Table 1.1: List of short-baseline reactor neutrino experiments

1.3 Reactor Neutrino Oscillation

Nuclear power plants have played an important role in experimental neutrino physics. In 1956, the neutrino was discovered at the Savannah River Reactor by Frederick Reines, Clyde Cowan, and their researchers [24]. KamLAND observed the disappearance of reactor antineutrinos and neutrino oscillation-induced distortions in the energy spectrum because of the mixing angle θ_{12} [6, 7]. By the low-energy reactor neutrino, the mixing angle can be measured by a short-baseline experiment without matter effects and CP violation. The reactor neutrino experiment does not need to construct neutrino beam facilities that require huge human resources and costs. Using these advantages, RENO, Daya Bay, and Double-Chooz experiments measured the smallest mixing angle θ_{13} based on an observed reactor neutrino rate with respect to its expectation in 2002 [15, 14, 16].

As summarized in Table 1.1, past reactor experiments found that a single detector located less than 1 km from a reactor was not enough to measure neutrino disappearance. They encountered some problems in measuring neutrino oscillation. The major problem was the instability of the Gd-doped liquid scintillator (LS). For example, the Palo Verde and CHOOZ experiments [34] struggled with Gd-doped LS deteriorated and turned yellow a few months after deployment, which reduced the detection efficiency [40, 41]. The other problem was a rather

large systematic uncertainty associated with a single detector measurement. To prevent the deterioration of Gd-doped LS, researchers have developed a new chemical synthesis of the Gd-doped LS with good liquid scintillator properties, like transparency, absorptance, wavelengths emittance in the different specific wavelengths, and long-term stability [42, 43, 44]. Deploying multiple identical detectors in different locations concerning reactors crucially reduces the systematic uncertainties associated with detectors and reactors. This method allows a far-to-near detector comparison to find the disappearance of reactor $\bar{\nu}_e$. To implement these improvements, the second generation of reactor experiment, Daya Bay, Double Chooz, and RENO, deployed multiple identical detectors at different locations concerning the reactors to test the disappearance of a reactor, which will allow the calculation of the disappearance of $\bar{\nu}_e$ from the ratio of the observed $\bar{\nu}_e$ rates. Adapted these strategies, the experiments successfully measured θ_{13} Daya Bay [14], RENO [15], and Double-Chooz [16], reported the measurement of θ_{13}.

1.3.1 Reactor Neutrino

The reactor electron antineutrinos ($\bar{\nu}_e$) are emitted by nuclear fission and β-decay. Figure 1.2 shows a Feynman diagram of the β-decay interaction. A down (d) quark of neutron transforms into an up (u) quark by weak interaction. The emitted W^- boson changes into an electron and an electron antineutrino.

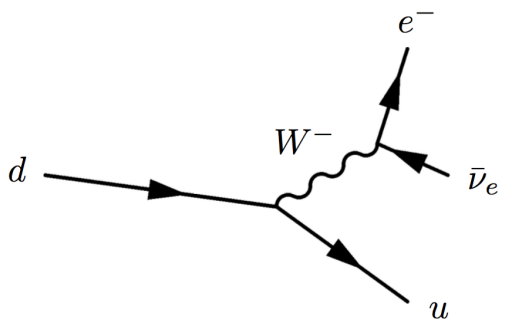

Figure 1.2: A neutron β-decay Feynman diagram. A neutron decays with weak interaction and transforms a proton, an electron, and an electron antineutrino.

The four isotopes of the reactor main fuel components, ^{235}U, ^{239}Pu, ^{241}Pu, and ^{238}U, produce roughly six electron antineutrino from each fission [45, 46, 47, 48] in the each fissions and release an average of ∼200 MeV of energy [49]. Thus, the neutrino intensity can be estimated to be $\sim 2 \times 10^{20}/(GW_{th} \cdot s)$.

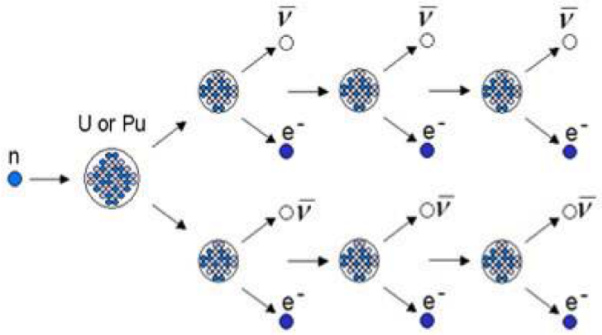

Figure 1.3: Neutrino production of a reactor fuel fission process [50].

The reactor antineutrino energy spectrum varies according to the thermal power of the plant and the fission fraction of the main fuel components with four isotopes. The thermal power changes over time. The fission fraction changes with fuel burning, as shown in the left of Figure 1.4. Each isotope's antineutrino energy spectrum per fission is individually different from isotopes, as shown in the right of Figure 1.4. The expected flux and energy spectrum can be estimated by merging all operation data.

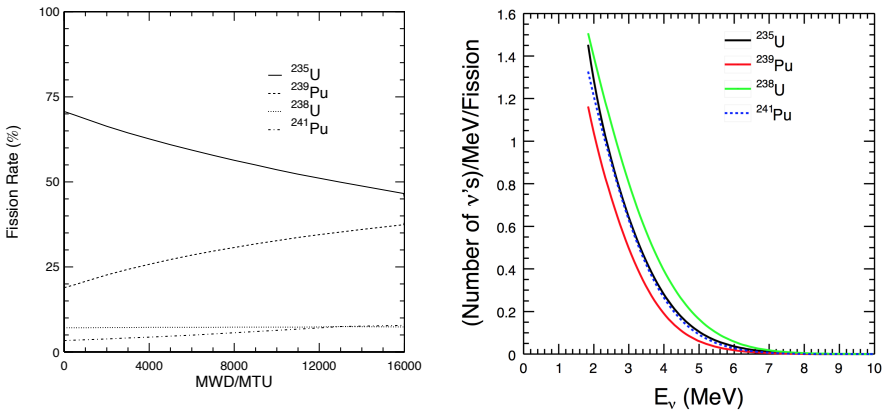

Figure 1.4: (Left) Evolution of fission fraction for four major isotopes during fuel burn-up. The horizontal axis is megawatt days per metric ton of uranium (MWD/MTU). (Right) Normalized neutrino energy spectrum from the fission of each isotopes [51, 52]. The threshold energy of IBD is 1.8 MeV.

1.3.2 Detection of Reactor Neutrino

An electron antineutrino interacts with a free proton via the inverse beta decay (IBD) process, producing a positron and a neutron

$$\bar{\nu}_e + p \rightarrow e^+ + n, \tag{1.7}$$

where a Feynman diagram of IBD is shown in Figure 1.5.

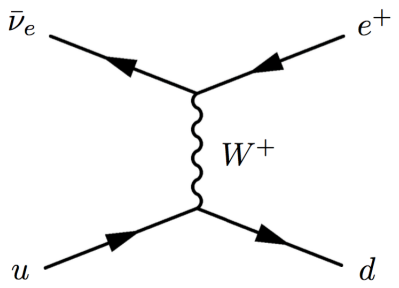

Figure 1.5: An inverse β-decay Feynman diagram. An electron antineutrino interacts with u quark and produces a proton and a d quark.

The antineutrino energy is directly related to the positron energy by

$$E_{\bar{\nu}_e} = E_{e^+} + (m_n - m_p) + \mathcal{O}(E_{\bar{\nu}_e}/m_n) \simeq E_{e^+} + 1.293 \text{ MeV} \tag{1.8}$$

where E_{e^+} is outgoing positron energy with the inverse neutron decay, m_n is the neutron, and m_p is the proton mass. The positron takes its energy and then annihilates, yielding two photons, each with a minimum of 0.511 MeV. Experimentally visible energy is E_{e^+} and additionally obtain+0.511 MeV. Thus the minimum energy is 1.022 MeV. A proton in the following process subsequently captures an outgoing neutron:

$$n + p \rightarrow D + \gamma, \tag{1.9}$$

where D is deuterium. The neutron capture meantime is ~ 200 μs.

Suppose a neutron is captured by Gd, the capture cross-section becomes more prominent, and additional gamma rays are produced with a total energy of approximately 8 MeV. Therefore, The reactor neutrino experimental signal consists of prompt energy deposited 1$\sim$8 MeV by the positron kinetic energy and the annihilated e^+e^- masses, followed by $\sim$ 2.2 MeV energy of gamma from neutron capture on Hydrogen $\sim$200 μs later or by $\sim$8 MeV energy of gammas from neutron capture on Gd $\sim$30 μs later. Adapting this advantage of the coincidence between

prompt and delayed signals is essential for background control. Figure 1.6 shows the reactor neutrino signal process via IBD, producing both prompt and delayed signals.

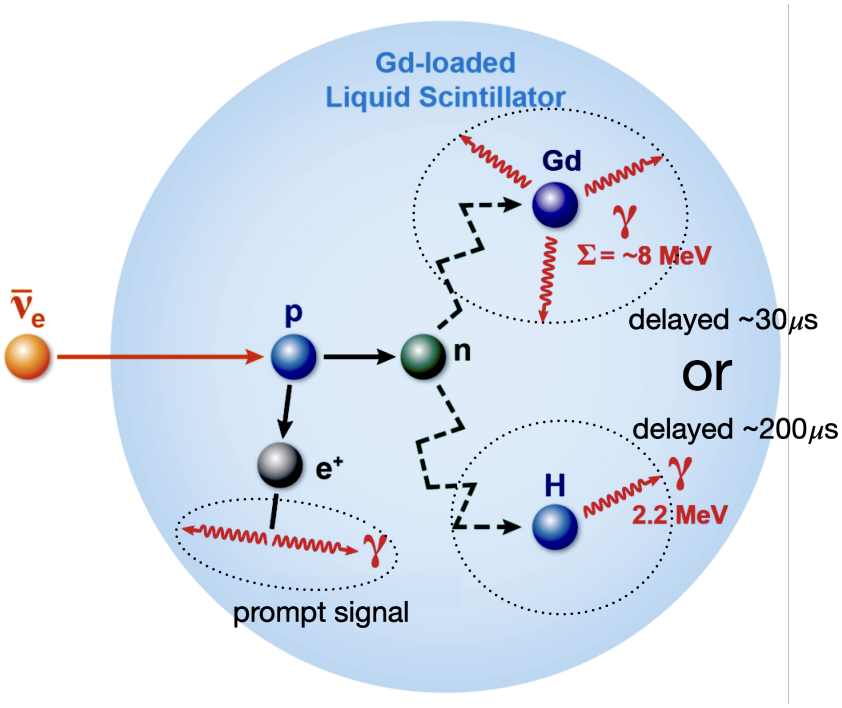

Figure 1.6: An electron antineutrino would be detected by a corresponding signal of prompt positron annihilation and a delayed neutron captured by Gd or H [53]. The positron takes away most of the kinetic energy of the electron antineutrino.

The IBD process's cross-section takes the form of [54],

$$\sigma(E_{e^+}) \simeq \frac{2\pi^2\hbar^3}{m_e^5 f \tau_n} p_{e^+} E_{e^+}, \tag{1.10}$$

where p_{e^+} is the momentum of the positron, m_e is the positron mass, τ_n is the free neutron lifetime, and $f = 1.7152$ is the neutron decay space factor [55].

Figure 1.7 shows reactor neutrino flux, IBD cross-section, and measured spectrum at detector with arbitrary units in Ref. [56]. The most feasible neutrino energy interacting at the detector is ~ 3.8 MeV.

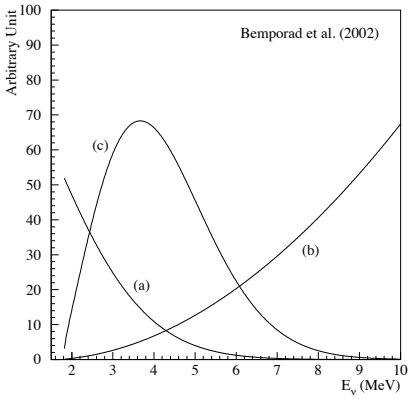

Figure 1.7: Reactor $\bar{\nu}_e$ flux, IBD cross-section, and interaction spectrum at a detector based on such reaction in Ref. [56]. The cut-off at 1.8 MeV is due to the minimum neutrino energy required for the IBD process.

1.3.3 Reactor Neutrino Oscillation Probability

By having low energy of reactor neutrino, under 12 MeV, the reactor neutrino cannot produce muons or taus through charged current interaction. Therefore, the reactor experiment should only observe the disappearance of reactor electron antineutrino by measuring the survival probability $P(\bar{\nu}_e \to \bar{\nu}_e)$. The survival probability does not depend on the CP phase δ in Ref. [57]. Moreover, due to the low neutrino energy and short baseline, the matter effect is insignificant in the reactor experiment [58]. Therefore, the neutrino survival probability in the vacuum can be accepted to model the neutrino oscillation in the reactor experiment. If the mass hierarchy was $m_1 < m_2 < m_3$, the probability $P(\bar{\nu}_e \to \bar{\nu}_e)$ is written as [59].

$$
\begin{aligned}
P(\bar{\nu}_e \to \bar{\nu}_e) &= 1 - 4\sum_{j>k} |U_{ej}|^2 |U_{ek}|^2 \sin^2\left(\frac{\Delta m^2_{jk} L}{4E}\right) \qquad (1.11)\\
&= 1 - \cos^4\theta_{13}\sin^2 2\theta_{12}\sin^2\left(\frac{\Delta m^2_{21} L}{4E}\right)\\
&- \sin^2 2\theta_{13}\left(\cos^2\theta_{12}\sin^2\left(\frac{\Delta m^2_{31} L}{4E}\right) + \sin^2\theta_{12}\sin^2\left(\frac{\Delta m^2_{32} L}{4E}\right)\right)\\
&\simeq 1 - \cos^4\theta_{13}\sin^2 2\theta_{12}\sin^2\left(\frac{\Delta m^2_{21} L}{4E}\right) - \sin^2 2\theta_{13}\sin^2\left(\frac{\Delta m^2_{ee} L}{4E}\right)
\end{aligned}
$$

where,

$$\Delta m^2_{ee} = \cos^2\theta_{12}\Delta m^2_{31} + \sin^2\theta_{12}\Delta m^2_{32} \tag{1.12}$$

Equation 1.11 is composed of two quadratic components; Δm^2_{21} and Δm^2_{ee}. Figure 1.8 shows survival probability as a function of baseline, L (km). The Δm^2_{21} term is insignificant, which is the short baseline. The other term (Δm^2_{ee}) has a full contribution in the few-kilometer baseline. The first local minimum point is located ∼1.5 km away from the core of the reactor. Thus, when the far detector is located in the ∼1.5 km from the plant, the θ_{13} will be effectively measured.

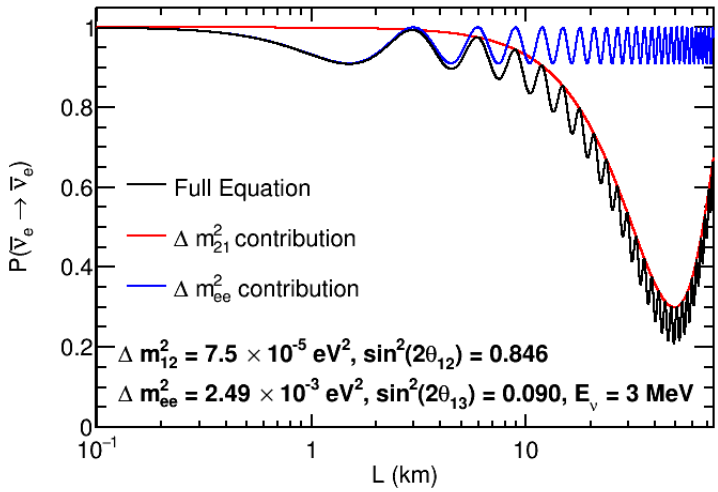

Figure 1.8: Survival probability $P(\bar{\nu_e} \to \bar{\nu_e})$ depended on distance. The first local minimum point is located ∼1.5 km away from the reactor core. The red line indicates the Δm^2_{21}. The blue line represents the Δm^2_{ee} term in Equation 1.11. The black line is the sum of the previous two terms(red and blue lines). At the first local minimum point, the Δm^2_{21} contribution term is insignificant.

1.3.4 Determination of Mixing Angle θ_{13}

In presented Equation 1.11, mixing angle θ_{13} determines the survival probability magnitude within the short baseline range. The detection of angle θ_{13} enhances our understanding of neutrino oscillation. Moreover, the angle θ_{13} can be a cornerstone for CP violation and determining neutrino mass ordering in neutrino oscillation [60, 61]. The mass hierarchy of neutrino may be directly measured by a reactor experiment with a significant value of θ_{13} and a ∼50 km baseline, such as the Jiangmen underground neutrino observatory (JUNO) [62]. The δ_{CP} for CP

phase angle invariably shown in the $U_{e3} = \sin\theta_{13}e^{-i\delta_{CP}}$. Therefore, the mixing angle θ_{13} has a crucial key to estimating the value of phase angle δ_{CP} [63].

1.4 RENO Experiment

The RENO is the reactor neutrino experiment to measure neutrino oscillation with mixing angle θ_{13} and mass difference $|\Delta m^2_{ee}|$. The experiment was conducted near the Hanbit nuclear power plant at YeongGwang in Korea. The RENO Collaboration has continued data-taking since August 2011. Two identical near and far detectors (ND and FD) are located 294 and 1383 m, respectively, from the center of six reactor cores of the power plant. They detect IBD events of $\bar{\nu}_e$ interactions with free protons in the hydrocarbon LS. The power plant complex consists of six pressurized water reactors, each with a maximum thermal output of 2.8 GW_{th}, that is situated in a linear array spanning 1.3 km with equal spacings. The reactor neutrino flux weighted baseline is 410.6 m for ND and 1445.7 m for FD.

In early April 2012, the experiment successfully determined the θ_{13} by observing the deficit of reactor neutrinos [15]. In 2016, the measurement result of θ_{13} and $|\Delta m^2_{ee}|$ from rate and shape analysis was published [18]. In 2018, the RENO Collaboration reported a precise measurement of θ_{13} and $|\Delta m^2_{ee}|$ based on ∼2200 days of n-Gd data sample [19].

1.5 This measurement

It is rather difficult to measure the θ_{13} value from the IBD data sample with a delayed signal of neutron capture on H (n-H) because of its high background. As of June 2019, the RENO experiment has collected about 2,900 days of n-H data with a data-taking efficiency higher than ∼95%. The n-H IBD candidates suffer from more accidentally paired backgrounds due to a larger coincidence time window than the IBD candidates with a delayed signal of neutron capture on Gd (n-Gd). In addition, the n-H delayed signal with an emitted 2.2 MeV γ-ray is swamped by the high environmental radioactivity below 3.5 MeV, while the n-Gd delayed signal with γ-rays of a total energy ∼8 MeV is free from the ambient γ-ray background. The target volume of the n-H IBD sample is 2.8 times larger than that of the n-Gd IBD sample, which utilizes 16.5 tons of Gd-doped LS. This provides 2.3 times more IBD yield for the n-H IBD sample than n-Gd. The total number of free protons in the Gd-unloaded LS is estimated to be $(2.110\pm0.015)\times10^{10}$ while it is $(1.189\pm0.008)\times10^{10}$ in the Gd-doped LS. However, because of tight selection criteria against high backgrounds, the detection efficiency is as large as 21.8%,

roughly 29% of the n-Gd efficiency, and thus the observed n-H IBD candidates become less relevant to the n-Gd sample.

RENO reported a measurement of the θ_{13} value using $\sim$1500 days of the n-H IBD candidates [64]. This was possible due to successful extraction of the n-H delayed signal from the high accidental background, based on careful purification of liquid scintillator and detector materials, use of low–radioactivity PMT glass, and effective selection criteria. This thesis presents a more precisely measured θ_{13} value using $\sim$2900 days of the n-H IBD candidates, providing a systematic cross-check on the measured value as an independent measurement. With the increased data sample, the statistical error of this measurement is reduced by roughly 40% relative to the previous measurement. Based on improved background uncertainties and additional removal of PMT noise events, the systematic error is reduced significantly by roughly 60%.

The subsequent chapters are arranged as follows: Chapter 2 describes the experimental setup and RENO detectors. Chapter 3 describes the expected flux and spectrum of reactor antineutrinos and Monte Carlo simulation. Chapter 4 describes the reconstruction of the event vertex and energy. Chapter 5 elicits the energy calibration of the near and far detectors. Chapters 6 to 9 present a rate analysis of 2,900 days of n-H data. Chapters 6 and 7 describe the IBD selection criteria and the background estimation, respectively. Chapter 8 discusses systematic uncertainties. Chapter 9 presents a rate measurement of θ_{13}. Conclusions and discussions are given in Chapter 10.

Chapter 2

Setup of the RENO Experiment

2.1 Overview

The Hanbit Nuclear power plant, which has six reactors with the world's second-largest thermal output of 16.4 GWh, is one of the best neutrino sources for searching the neutrino oscillation parameters. mixing angle θ_{13}. The Reactor Experiment for Neutrino Oscillation (RENO) is an experiment to measure the neutrino oscillation mixing angle θ_{13} using electron antineutrino, which is emitted from the Habit nuclear power plant in Yonggwang, Korea. The power plant, which has six reactors producing a total thermal output of 16.4 GWh and is the second largest in the world, is an intense source of low-energy antineutrinos suitable for measuring neutrino oscillation parameters. The RENO has two identical detectors, with each having a 16-ton liquid scintillator. One detector is located at a near site, at a distance of 294 m from the center of the reactor array, and the other is located at a far site, at a distance of 1384 m away from the center of the reactor array. The two detectors are designed identically to cancel out a number of systematic uncertainties by normalizing the neutrino fluxes at the far detector (FD) and the near detector (ND). The RENO detectors have a layered structure similar to those in other reactors neutrino experiments, such as those in the Daya Bay and Double Chooz experiments. The RENO detectors consist of a target, γ-catcher, buffer, and veto, arranged from the center to the outer part of the detector. The photomultiplier tubes (PMTs) for detecting neutrino interaction are located in the buffer layer. A cross-sectional view of one of the RENO detectors is shown in Figure 2.1

The "target"is a gadolinium (Gd) doped liquid scintillator and is constructed of a transparent and cylindrical vessel made of acrylic plastic. An inverse beta

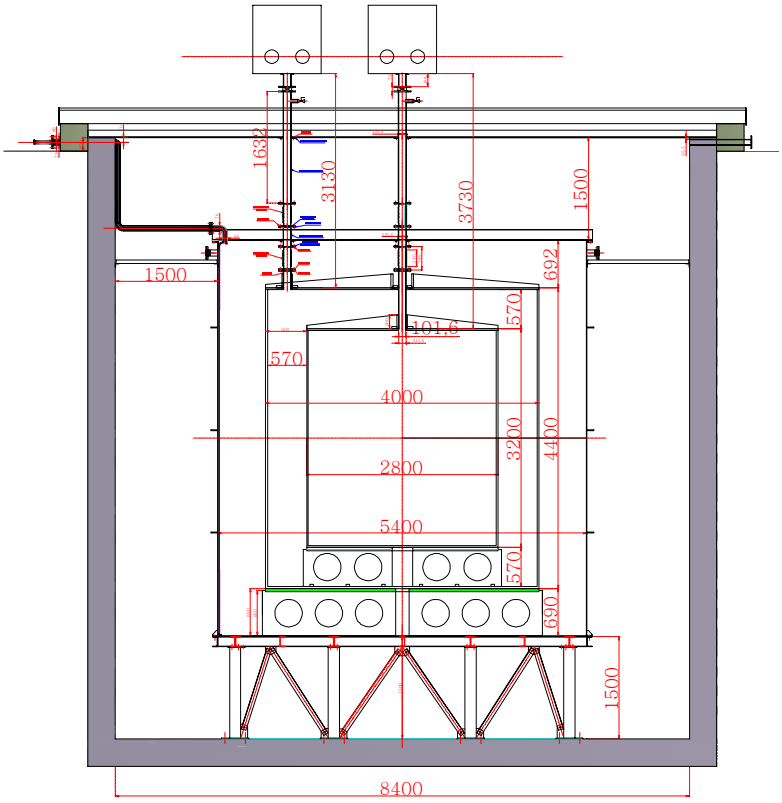

Figure 2.1: Cross-sectional view of one of the RENO detectors. The order of the sections from the centerline is as follows: Gd doped liquid scintillator-filled target, only liquid scintillator-filled γ catcher in a transparent acrylic vessel, mineral oil-filled buffer in a stainless steel vessel, and ultrapure water-filled veto layer. The inner detectors (ID) and outer detectors (OD) PMTs are installed on buffer and veto vessels, respectively, and facing inward.

decay (IBD) event proceeds as a pair of a positron and a neutron. The positron loses energy via a scintillating process before it is converted into two γs by a pair annihilation. The neutron thermalizes and is then captured by the Gd nucleus, producing several γs. The γs produced close to the boundary of the target can escape the target without completely depositing their energy in the scintillator. Not to lose the energy carried by escaping γs from the target, a "γ-catcher" is employed, which is another liquid scintillator layer surrounding the target. Unlike the target, the liquid scintillator in this γ-catcher is not loaded with Gd because this layer is intended to augment the target in the energy measurement of the γs emitted in the target. The transparent cylindrical acrylic encloses the γ-catcher liquid, similar to the target. The γ-catcher is surrounded by a non-scintillating liquid region, known as the "buffer". Mineral-oil is adapted as a buffer and is filled in a cylindrical stainless steel vessel. The PMTs are installed on the inner buffer vessel surface. The buffer reduces external γs, mostly originating from ambient radioactive isotopes contained in the PMTs, entering the scintillating volume. The outermost region of the RENO detector is the "veto", which is water Cherenkov detection. The "veto" plays a role in reducing background γs or neutrons from the surrounding environment as well as from background events induced by cosmic muons. The veto container consists of 40-cm-thick concrete, and the cover is stainless steel. The PMTs are installed on the inner veto detector for detecting Cherenkov light from high-energy cosmic rays. Many design parameters were decided by optimal performance using Monte Carlo simulation. The simulation study considered ambient background γs from the PMTs and surrounding rocks, cosmogenic events reaching the detector, as well as IBD events from the reactor antineutrinos. More details of the detector compositions are summarized in Table 2.1

Detector Component	Outer Diamete (mm)	Outer Height (mm)	Material	Volume (m^3)	Mass (tons)
Target	2750	3150	Gd-loaded LS	18.70	16.08
Target Vessel	2800	3200	Acrylic	0.99	1.18
γ-catcher	3940	4340	LS	33.19	28.55
γ-catcher Vessel	4000	4400	Acrylic	2.38	2.83
Buffer	5388	5788	Oil	76.46	64.22
Buffer Vessel	5400	5800	SUS	1.05	8.39
Veto	8388	8788	Water	352.61	352.61

Table 2.1: Features of the detector mechanical structure.

Figure 2.2: Hanbit nuclear power plant located in Yonggwang, 250 km south of Seoul. Three other nuclear power plant sites are also located in the south-eastern part of Korea

The data acquisition (DAQ) system of RENO is devised to collect the charge and time of PMT hits. The FD and ND had to be identical; we built them with the same PMT configuration and readout system. The RENO DAQ adapted electronics from the Super-Kamiokande experiment.

2.2 Experimental Arrangement

2.2.1 Hanbit Nuclear Power Plant

The RENO detectors are located around the Hanbit (previously known as Yonggwang) nuclear power plant, operated by the Korea Hydro and Nuclear Power Co., Ltd (KHNP) in Yonggwang, the southwest coastal region in South Korea, approximately 250 km from Seoul, as shown in Figure 2.2. The power plant has six reactors linearly aligned at equal distances of ∼260 m, as shown in Figure 2.3. These reactors are pressurized water reactors (PWR). The reactor fuel cycle changes from 12 months to 24 months and the refuelings are performed during plant shutdowns. The total thermal output of the six reactor cores is 16.8 GW_{th}, with each reactor core generating approximately equal power.

Figure 2.3: The Arrangement of the RENO experimental site. The red dots are reactors, and the yellow dots are detectors. Six reactors are equally spaced at approximately 1280 m distances. ND and FD are located at a distance of 290 m and 1380 m from the center of the reactor array, respectively. This picture was taken from Google EarthTM and was copyrighted therein. © 2015 Google, DigitalGlobe

Reactor No.	ND (m)	FD (m)
1	667.9	1556.5
2	451.8	1456.2
3	304.8	1395.9
4	336.1	1381.3
5	513.9	1413.8
6	739.1	1490.1

Table 2.2: Distances of each power plant core from ND and FD.

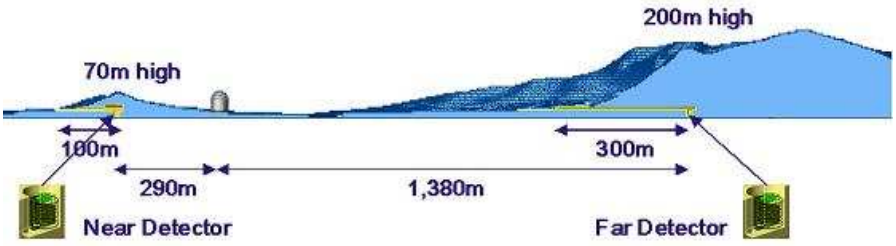

Figure 2.4: A Cross-sectional view of the RENO experimental site. ND is constructed under a 70 m mountain, and FD is constructed under a 200 m high mountain nearby the power plants.

2.2.2 FD and ND

One of the main sources of systematic uncertainties is the uncertainty resulting from the neutrino flux of the reactor. To minimize the effects of this problem, two identical detectors, FD and ND, are engaged. Each detector contains 18.7 m^3 of liquid scintillator doped with 0.1% of gadolinium as a "target". The far to near ratio measurement using the two identical detectors significantly reduces the systematic uncertainties in the measurement of θ_{13} owing to the cancellation of their correlated uncertainties. Figure 2.3 shows the layout of the six reactors and two detectors, and Table 2.2 shows the distances between reactors and detectors. ND and FD are located at a distance of 294 m and 1384 m from the center of the reactor array, respectively. The ND is located under a 70 m high (above mean sea level) ridge with an overburden of 110 meter water equivalent (mwe), and the FD is located under a 260 m high mountain with an overburden of 450 mwe as shown in Figure 2.4.

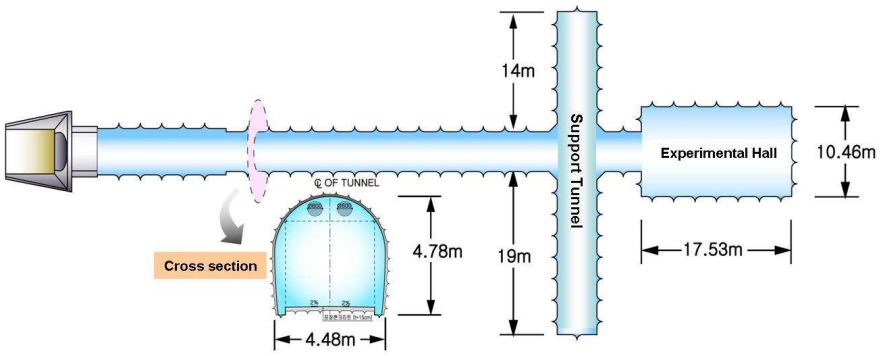

Figure 2.5: The access tunnel and the experimental hall sectional views. The tunnels were constructed using the NATM.

2.2.3 Underground Facility and Experiment Halls

The underground laboratories are constructed with two horizontal tunnels, which have a length of 100 m for ND and 300 m for FD, as represented in Figure 2.5. The tunnels were constructed using the New Austrian tunneling method (NATM). Cross-sectional views of the tunnel and the experimental hall are shown in Figure 2.5, and a three-dimensional (3D) cross-sectional view of the experimental hall is shown in Figure 2.6. The access tunnels of ND and FD sites are 95 m and 272 m long, respectively. Figure 2.5 shows a cross-sectional view of the access tunnel. There is a gradient toward the experimental hall as 0.3% for both tunnels to provide natural drainage. The tunnels can accommodate the passage of a 10-ton truck.

2.3 Detector Components

The RENO detectors, FD and ND are identical and consist of a cylindrical target with a radius of 137.5 cm and a height of 315 cm, providing a volume of 18.7 m^3. The detectors consist of a target, γ-catcher, buffer, and veto arranged concentrically from the centerline to the edge of the detector. A cross-sectional view of the detector is shown in Figure 2.7.

2.3.1 Target and γ-catcher

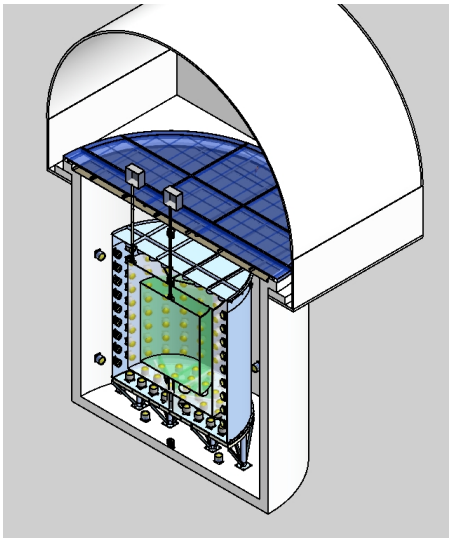

Figure 2.6: The experimental hall sectional view.

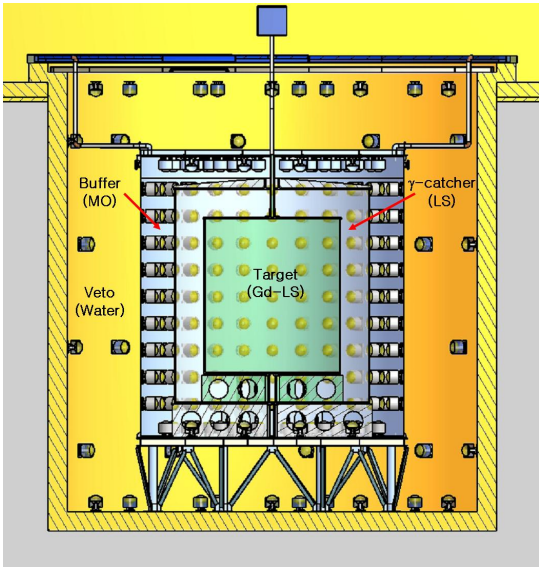

Figure 2.7: The RENO detector sectional view. The target is filled with the liquid scintillator doped with Gd in a transparent acrylic vessel, surrounded by a 33.2 m^3 unloaded liquid scintillator of γ-catcher and a 76.5 m^3 non-scintillating buffer. 354 and 67 10-inch PMTs are installed on the buffer and veto vessel walls, respectively.

Structure

The most central layers, target, and γ-catcher, are enclosed in acrylic vessels, which are transparent to optical photons with above 400 nm wavelengths. Two main topics for this configuration were considered: the chemical compatibility between the contents and the vessel and mechanical stability. Considering the chemical compatibility, the liquid scintillating material is required to avoid the chemical interaction with the vessel for both the target and the γ-catcher during the experiment. At the same time, the γ-catcher vessel is required to be chemically inert to the mineral oil in the buffer layer. Extensive studies have been carried out on the chemical compatibility of these materials for the Chooz experiment and others. The RENO collaboration also conducted diverse R&D activities on the chemical interaction of acrylic plastic and other materials used in the experiment. The vessels are required to mechanically resist the stresses of being subjected to and maintain their structural integrities during all phases of the experiment. When the liquid is loaded into the vessels, the vessel volume slightly changes from its original volume. This change is required to be maintained within the specified thickness tolerance of 25 mm. The target vessel mass is 1.2 tons. The target vessel volume is 19.2 m^3, and the total mass of the target vessel, target liquid, and the supporting structure is 17.3 tons. The supporting structure is also made of the same acrylic plastic, and the target vessel is installed on this supporting structure inside the γ-catcher vessel. Within both the filled target and the γ-catcher, the net load on the target supporting structure is 328 kg due to buoyancy. At the center of the top of the vessel is a pipe connecting the target volume to the outside of the detector to fill the target liquid and insert radioactive calibration sources.

The γ-catcher has a similar design to the target but has a volume of approximately 3 times larger. The γ-catcher vessel is a transparent cylinder with a height of 4.4 m, a diameter of 4.0 m, and a wall thickness of 3 cm. The γ-catcher vessel is also installed on the supporting structure of acrylic plastic inside the buffer vessel. A pipe connects the top of the γ-catcher vessel and the outside of the detector for filling liquid and inserting the calibration source. The mass of the γ-catcher vessel is 2.8 tons. The total mass of the γ-catcher vessel and the γ-catcher liquid scintillator is 31.4 tons. When the γ-catcher is immersed in the buffer liquid, the total load on the γ-catcher supporting structure is 2.2 tons.

Acrylic Vessels

The target and γ-catcher vessels consist of polymethylmethacrylate (PMMA), a transparent acrylic plastic. The molecular formula of PMMA is (C5O2H8)n, and

Properties	Value
Density	1.19 g/cm^3
Melting point	130-140 °C
Refractive index	1.491
Transmittance	92%

Table 2.3: Mechanical and optical properties of cast acrylic, such as Plexiglas GS-233 from Degussa GmbH, Germany and R-Cast from Reynolds Co., USA.

it is also known by trade names such as Plexiglas, R-Cast, and Lucite. The properties of PMMA are shown in Table 2.3. Using additional ingredients in PMMA, ultraviolet (UV) light below 400 nm can be absorbed. The target and γ-catcher vessels, made of cast acrylic sheets (Plexiglas, GS-233), were supplied by Degussa GmbH, Germany. The cast acrylic sheet has better mechanical and chemical properties than the extruded acrylic sheet. The vessels were manufactured by KOA Tech in Korea. For convenient production, these vessels are manufactured in several pieces and assembled mostly at the manufacturing site. The vessel parts are bonded by polymerization, and the joined sections are treated with an annealing process. The manufacturing precision of the vessels is 0.1% in volume (2 mm in 1 dimension); hence, there can be only a 0.14% difference in the volume of the target vessel between FD and ND. This difference can be measured and corrected by a mass flow meter and weight measurement.

Chimney

Both target and γ-catcher have a chimney for filling liquids and transporting calibration sources to and out of the target or the γ-catcher from the top lid of the veto vessel. The chimney consists of transparent acrylic tubing with a diameter of $\sim$4 inch, and a flexible convoluted polytetrafluoroethylene (PTFE) tube connects the buffer vessel and the acrylic tubing for stress relief. The chimney connecting the top lid with the buffer consists of stainless steel pipes extending to the top cover of the veto vessel.

2.3.2 Buffer

The buffer vessel is a stainless steel cylinder with a height of 5.8 m and a diameter of 5.4–m; it contains the target, γ-catcher, and buffer liquid. The buffer vessel is filled with non-scintillating oil to protect the internal scintillating volume from external background sources, including the radioactivity in the PMTs. The buffer

vessel also provides a mounting surface for the 354 inward-facing PMTs, optically isolated from the veto volume. The size of the buffer vessel was determined using Monte Carlo (MC) simulations. The buffer vessel is required to be chemically inert against the mineral oil inside and the water outside. In addition, it is required to withstand the stress arising from the load resulting from the liquids and structures contained by the vessel. The buffer vessel is made of 304L stainless steel with a thickness of 6 mm for the top lid and barrel section and 12 mm for the bottom plate to provide increased mechanical support. The external view of the buffer vessel is described in Figure 2.8. The surface of the vessel is not polished. When the detector is filled with the required liquids, the buffer vessel experiences a buoyant force due to the difference in density between the organic liquids inside the buffer vessel and water in the veto layer. The estimated buoyant force is 11.5 tons, and the supporting structure of the buffer vessel is designed to support this force. The buffer vessels are manufactured by Nivak Industrial Co., Ltd., Korea. They are transported as segmented pieces to the experimental site and assembled in the halls. The barrel section comprises six segments, with top and bottom plates, each consisting of three parts. The bottom plate is welded to the barrel section, and the top plate is bolted to the barrel section. A total of 354 10-inch PMTs are located on the inner walls of the buffer vessel, 234 PMTs on the barrel section, and 60 PMTs on the top and bottom plates each, as shown in Figure 2.9. The PMTs are located upright on the walls using the PMT holding structure described in Sect. 2.3.4.

2.3.3 Veto

Design Criteria

The veto system is located outside of the buffer tank exactly adjacent to it. The main background of the experiment is due to cosmic muons, and it is very crucial to identify the entering muons because they can produce neutrons via muon–nucleus interaction in the detector. There are also correlated backgrounds from ^{9}Li/^{8}He in the target and γ-catcher produced by cosmic muons. Although the veto system is not included in the trigger, the signals of a cosmic muon in the veto system are used to identify cosmic muon-related backgrounds for each candidate event from the neutrino interaction. The veto vessel is required to be chemically compatible with water and sufficiently strong to support all three inner chambers before filling the liquids.

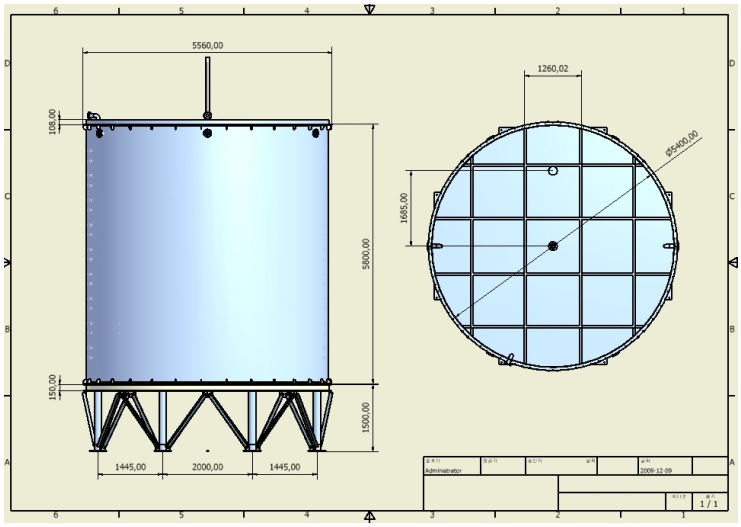

Figure 2.8: External view of the buffer vessel. The vessel consists of stainless steel with 304L, and the supporting structure consists of nickel-plated steel pipes and rods.

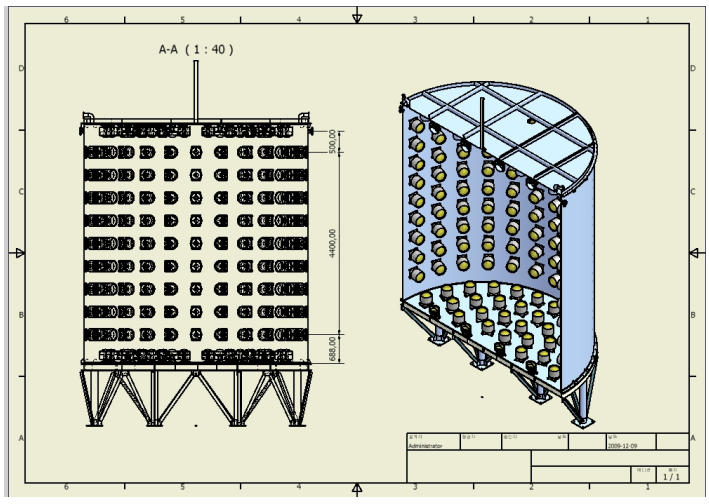

Figure 2.9: Internal detector PMT array in the buffer vessel. A total of 354 10-inch PMTs are installed on the wall of the vessel using PMT holders.

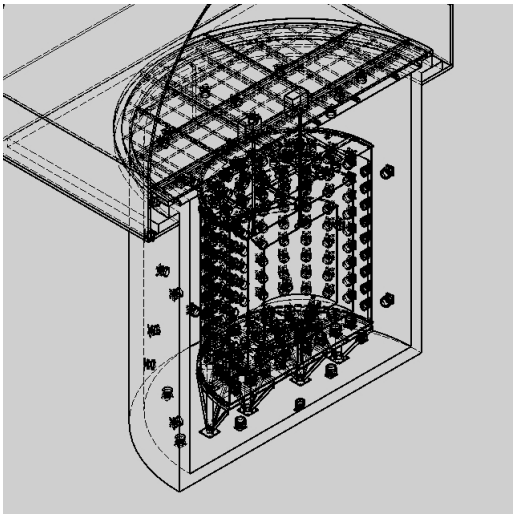

Figure 2.10: Transparent view of PMT arrays showing both the inner and outer PMTs.

Structure

The height and inner diameter of the veto vessel are 8.8 m and 8.4 m, respectively. The vessel is constructed with a concrete wall of thickness of 40 cm. The inner surface of the concrete vessel is waterproofed with epoxy resin. The purified water is continuously circulated by a water purification system. There are a total of 67 10-inch PMTs (R7081 Hamamatsu) installed on the inner surface of the veto vessel. These PMTs are waterproof because veto is filled with water. The buffer vessel's external surface and the veto vessel's internal surface are coated with Tyvek (TiO_2) to increase the collection capability of Cherenkov photons in the water. Figure 2.10 shows the final PMT arrangements of both buffer and veto vessels.

2.3.4 PMT

PMT Requirements and Specification

The scintillation lights from the target and γ-catcher are detected by the PMTs attached to the internal surface of the buffer vessel. About 150 photoelectrons are detected for a 1 MeV event occurring at the center of the target. As the minimum energy of positron from IBD is 1.022 MeV, the average number of

photoelectrons per PMT in the buffer layer is approximately 0.5. Therefore, the PMTs are required to distinguish single photoelectrons with high resolution, so the peak-to-valley ratio and the single photoelectron resolution of the PMTs are important parameters. The non-scintillating buffer region is required mainly to shield the γ-catcher and the target from the radioactivity of the PMTs, which needs to be studied to obtain information on the rate of background originating from PMTs. The PMT background events are mostly in the low-energy region of less than 2 MeV and can be incorrectly identified as signals by accidental coincidence with neutron-like background events. As the PMTs are immersed in a layer of mineral oil, it is also important that the complete PMT assembly is required to be chemically inert to mineral oil. The oil proofing is required to be stable for the duration of the experiment. We measured the quantum efficiencies of all PMTs with a relative accuracy of less than 5%. The outlying PMTs were excluded from installation in the detectors.

After considering several performance parameters, such as single photoelectron resolution, afterpulse rate, radioactivity in the PMT, and overall detector performance-to-cost ratio, 10-inch low-background R7081-Low PMTs by Hamamatsu were chosen for RENO. Their specifications are shown in Table 2.4.

	R7081
Gain($\times 10^7$)	1.0 @ 1500 V
QE @ peak (nm)	25% @390
DC (nA)	50
Size (inch)	10
Weight (g)	1150
Rise Time (ns)	4.3
TTS (ns)	2.9
Afterpulse	2%
Peak-to-valley ratio	3.5

Table 2.4: Specifications of the Hamamatsu R7081 PMTs.

PMT Holder

The PMTs are located on the internal wall of the stainless steel buffer vessel. We aim to minimize the material while ensuring that the holding structure is as stable as possible. In addition, the distance between the surface of the PMT photocathode and the buffer vessel needs to be minimized. The PMT holder comprises $\sim$1.5–2.0 mm thick stainless steel. The schematic of the PMT holder is

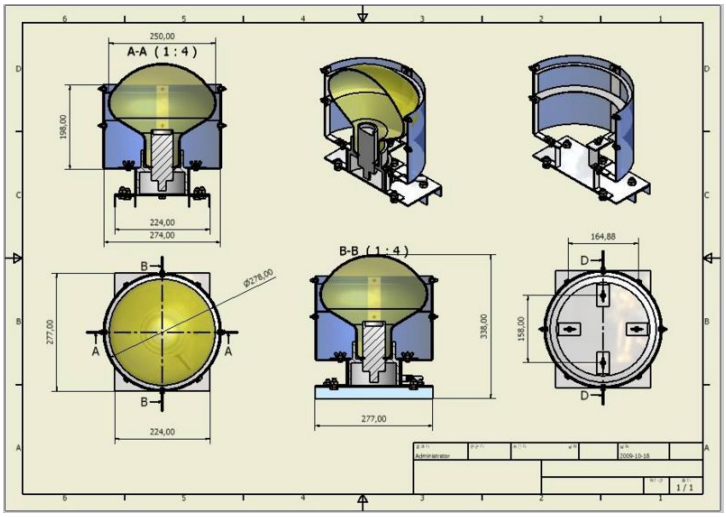

Figure 2.11: Design of the PMT holder. Two stainless steel rims hold the glass of the 10-inch PMT. A cylindrical mu-metal sheet surrounds the individual PMT outside of the rings to reduce the effect of the magnetic field.

shown in Figure 2.11. Two rings hold the PMT's glass bulb section, and the front ring defines the photosensitive area. The inner diameter of the rings is 12.3 cm. A mu-metal sheet surrounds the side of the structure to reduce the effects of the external magnetic fields. The height of the mu-metal shielding is determined based on a magnetic field survey at the experiment halls.

2.4 Liquid Scintillator

In the RENO experiment, linear alkylbenzene (LAB) is used as a base solvent of the liquid scintillator (LS). Previous neutrino experiments typically used pseudocumene (PC or TMB, C9H12, 1,2,4-trimethyl-benzene) as a base solvent of the liquid scintillator because it provides a higher light yield compared to that of others and has optical clarity. However, it is very toxic and has a low ash point; it harms the human body and the experiment's environment. Therefore, LAB is currently used in several neutrino experiments as a replacement. LAB is a safe material with a high ash point, relatively good light yield, high transmittance, and a large attenuation length. Figure 2.12 shows the molecular structure of LAB. Table 2.4 describes the properties of LAB compared with those of PC.

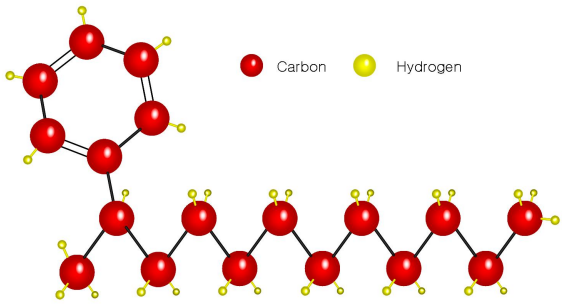

Figure 2.12: Molecular structure of LAB with a linear alkyl chain $C_{12}H_{25}$.

	PC	LAB
Molecular formula	C_9H_{12}	C_nH_{2n+1}-C_6H_5, n ≈ 10–13
Molecular weight (g/mol)	120.19	233∼237
Flashpoint (°C)	48	130
Density (g/ml)	0.89	0.85
Compatibility (acrylic)	Bad, need diluent	Good
Cost	Moderate	Low
Fluor dissolution	Very good	Moderate
Domestic availability	No	Yes
Toxicity	Toxic fume	Non toxic

Table 2.5: Comparison of PC and LAB.

The organic liquids filling the RENO detector are summarized in Table 2.6.

Region	Radius (mm)	Height (mm)	Volume (m^3)	Type
Target	1388	3176	19.21	0.1% Gd-loaded LS
Target vessel	1400	3200	0.48	Acrylic
γ-catcher	1985	4370	34.37	Unloaded scintillator
γ-catcher vessel	2000	4400	1.20	Acrylic
Buffer	2694	5788	76.64	Non-scintillating oil

Table 2.6: Organic liquids used in various parts of the RENO detector.

2.4.1 Optimization for Liquid Scintillator

Pure LAB absorbs light of 260 nm and emits longer wavelength light with a maximum of 340 nm. The acrylic material used for the target and the γ-catcher vessel rapidly becomes opaque below 390 nm, and the quantum efficiency of the installed PMTs (R7081-Low, Hamamatsu) is the most sensitive around the 390 nm region and still appropriate in the range of ∼400–430 nm. Therefore the scintillation light from LAB needs to be shifted above 400 nm. For this purpose, the RENO experiment uses 2,5-diphenyloxazole (PPO, C15H11NO) as a primary solute and 1,4-bis(2-methylstyryl)-benzene (bis-MSB) as a secondary wavelength shifter. As shown in Fig 2.13, PPO and bis-MSB emit photons at ∼340–440 nm and ∼380–460 nm, respectively.

Even though PPO and bis-MSB are necessary, as additional solute into the LAB decreases the attenuation length; thus, so we need to optimize the amount of solute needs to be optimized to reach a balance between the benefit of the wavelength shifter and the decrease in light output due to the decrease of in attenuation length. First, We measured the light yield while the amount of PPO was changed from in the range of ∼1– 20 g/L. Figure 2.14 shows the measured light yield by changing a function of PPO concentration. The light yield is maximum at a PPO concentration of about ∼3 g/L. Then, We measured the light yield while the amount of bis-MSB was changed from in the range ∼0– 200 mg/L, as shown in Figure 2.14. The light yield becomes saturated at 30 mg/L. Therefore, the amount of solute is determined as PPO 3 g/L for PPO and 30 mg/L for bis-MSB.

After determining the amount of the solute, we measured the absorbance of the liquid and converted it to the widely used attenuation length using the Beer–Lambert–Bouguer law. The absorbance is given by

$$A = -\log_{10}\left(\frac{I}{I_0}\right), \tag{2.1}$$

Where I_0 and I are the flux of the incident and the transmitted lights, respectively. According to the Beer–Lambert–Bouguer law, the attenuation length can be written as

$$\lambda = 0.4343\left(\frac{L}{A_{abs}}\right), \tag{2.2}$$

Where L is the length of travel of the light and A_{abs}, is the absorbance of a certain wavelength of the light.

Figure 2.15 shows the measured attenuation length of the LS, LAB, PPO, and bis-MSB. The RENO liquid scintillator has an attenuation length of ∼10 m in the range of ∼400–430 nm.

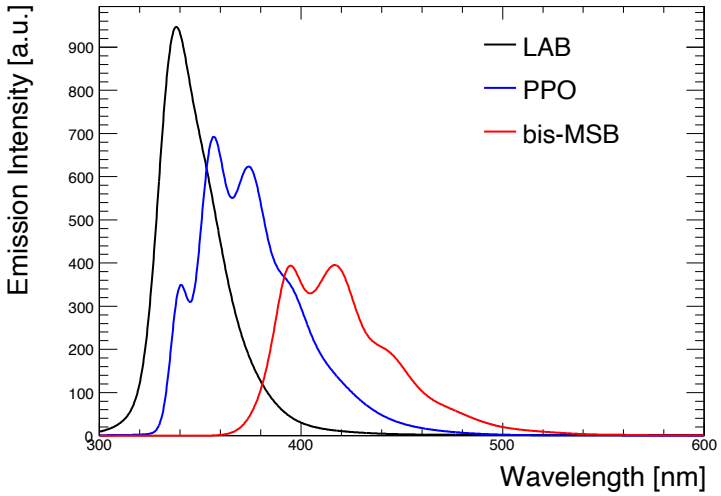

Figure 2.13: Emission spectrum of the solvent LAB (black), the primary fluor PPO (blue), and the wavelength shifter bis-MSB(red).

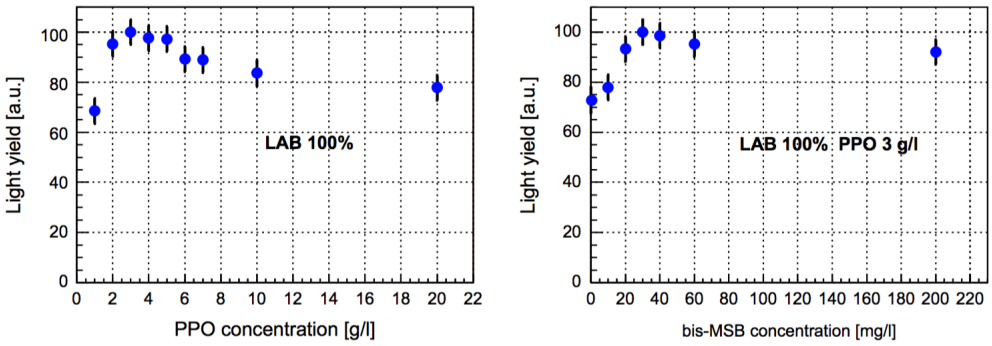

Figure 2.14: Left plot shows relative scintillation light yield of 100% LAB in arbitrary units as a function of PPO concentration. The Right plot shows the light yield of 100% LAB and 3 g/L of PPO with as a function of bis-MSB concentration.

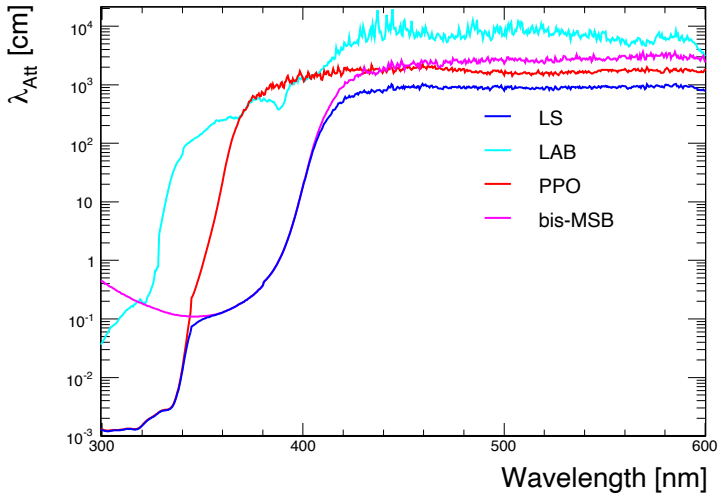

Figure 2.15: Attenuation length of the liquid scintillator. Pure LAB, PPO, and bis-MSB are shown as well.

2.4.2 Gd-loaded Liquid Scintillator

The hydrogen atoms ("free protons") in the liquid scintillator are antineutrino targets in the inverse beta decay reaction. When a neutron is captured by a free proton, γ rays are emitted with a total energy of $\sim$2.2 MeV. Nevertheless, a neutron capture on a Gd atom results in an emission of γ rays with a total energy of $\sim$8 MeV, which is significantly higher than the energies of the γ rays from natural radioactivity, which are typically below 3.5 MeV. The mean thermal neutron capture cross-section of Gd isotopes is four orders of magnitude larger than that of the proton. Therefore, the liquid scintillator doped with a small amount of Gd is ideal for detecting inverse beta decay events. Gadolinium is a silvery white soft, ductile metal belonging to the lanthanide group. It reacts slowly with water, dissolves in acids, and it can form stable organometallic complexes with ligands such as carboxylic acids (R–COOH) and β-diketones. Figure 2.16 shows the molecular structures of Gd compounds with ligands.

Synthesis of the Gd-Complex

It is difficult to add inorganic Gd salt to an organic liquid scintillator to achieve a stable Gd-loaded liquid scintillator. However, two formulations for Gd-

Figure 2.16: Gd compound structures of carboxylic acid and β-diketonate ligands. There are a series of liquid carboxylic acid radicals with different alkyl chains: C2 (acetic acid), C3 (propionic acid), C4 (isobutyl acid), C5 (isovaleric acid), C6 (2-methyl valeric acid, C5H11COOH, HMVA), C8 (ethyl-hexanoic), and C9 (trimethyl-hexanoic).

loaded liquid scintillator have shown promising results; liquid scintillators where Gd binding with carboxylate (CBX) ligands and with β-diketonate (BDK) ligands. The double Chooz and Daya Bay experiments reported the excellent performance of both BDK and CBX Gd-loaded liquid scintillators. After thorough consideration, we used CBX as our basis for ligands. The Gd-carboxylate compound can be synthesized in three steps:

1. $Gd_2O_3 + 6HCl \rightarrow 2GdCl_3 + 3H_2O$
2. $RCOOH + NH_3 * H_2O \rightarrow RCOONH_4 + H_2O$
3. $3RCOONH_4(aqueous) + GdCl_3(aqueous) \rightarrow Gd(RCOO)_3 + 3NH_4Cl$

First, based on step 1, a GdCl3 solution was prepared from Gd2O3. In step 2, 3,5,5-trimethylhexanoic acid (TMHA) was neutralized with ammonium hydroxide. In step 3, two aqueous solutions from steps 1 and 2 were mixed to produce Gd salt. When the two solutions are mixed, white Gd-carboxylate compound (Gd-TMHA) precipitates immediately. These are very pH-sensitive reactions. The precipitated Gd-TMHA was thoroughly rinsed with 18 M ultrapure water several times and then dried in a vacuum desiccator. The final Gd-TMHA product is shown in Figure 2.17. Then, a liquid–liquid extraction technique was used for the second method, as shown in Figure 2.18. Following the reactions, the organic solvent and water can be distinguished owing to the density difference.

2.5 DAQ and Monitoring System

2.5.1 Front-End Electronics

The antineutrino interaction in the RENO detector produces scintillation lights, and a part of them is converted into photoelectrons by the PMT. To detect the antineutrino event, the RENO detector is equipped with 354 inner PMTs and 67 outer PMTs. The readout system of RENO is designed to record the charge and arrival time of PMT hits. Based on the energy and timing information, we

Figure 2.17: White Gd-TMHA salt the following filtration with 0.2 μm pore size Te on the membrane filter.

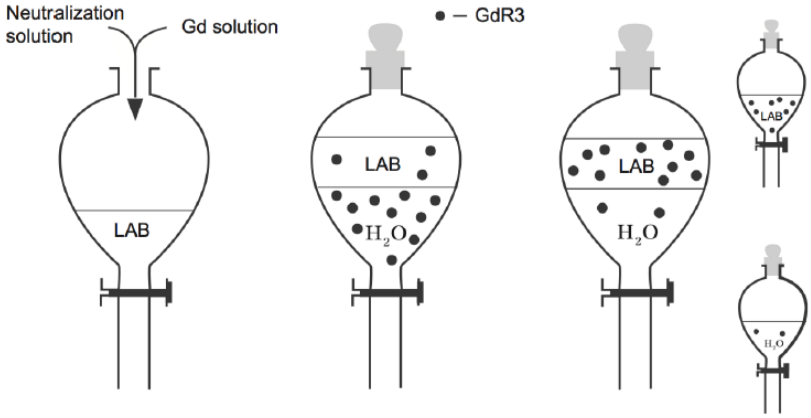

Figure 2.18: Liquid–liquid extraction method. Neutralization solution and Gd solution are mixed into the LAB. The Gd complex is directly dissolved in LAB. Two layers between the LAB and water are separated due to the density difference between the oil and water.

can select the neutrino events, reject background events, and reconstruct the vertex of the antineutrino interaction. The FD and ND are designed to have the same PMT configuration and readout system. The RENO DAQ employs electronics developed for the Super-Kamiokande experiment, which uses charge-to-time conversion chips (QTCs) to record hits at 60 kHz with no dead time.

The characteristics of RENO electronics are summarized as follows.

- PMT gain: $\sim 10^7$
- Time window: ∼300 ns
- Dynamic range of PMT signals: ∼1– 1000 photoelectrons
- Time resolution of each PMT signals: ∼1– 1:5 ns
- Data size: ∼ 200 kbyte/s for each detector
- No electronic dead time
- Time resolution between e^+ signal and neutron-like signal: $\sim 10\ ns$

The following section describes the RENO DAQ electronics.

2.5.2 Qbee Board

The QTC-based electronics with Ethernet (QBEE) board is an electronics based on QTC, with an onboard Ethernet card, developed for the Super-Kamiokande experiment and has been used since Sept. 2008. The new electronics system is sufficiently fast to record every PMT hit, and its stable data acquisition is guaranteed for over ten years. Each QBEE board is equipped with a 100-Mbps Ethernet card, which is sufficiently fast to transfer all hit information to an online computer without any loss. The hit information is stored in the online storage, and the software triggers are applied.

The PMT pulse generated by a photon hit is fed to a QTC chip. The QTC chip measures the hit time and the charge of the PMT pulse and converts them into a form that can be easily read and stored by the time to digital converters (TDCs). The output of the QTC chip is a logic pulse, with its leading edge marking the hit arrival time and its width representing the integrated charge of the PMT pulse. The characteristics of the QTC chip are summarized in Table 2.7.

The operation logic diagram of the QTC chip is shown in Figure 2.19. The QTC chip integrates the charge of a PMT pulse fed to the chip and outputs a pulse with a width proportional to the integrated charge. The QTC chip produces two gates for its charge integration operation: one for charging the capacitor (charge gate) in the QTC chip and the other for discharging the capacitor to measure

Dynamic range	$0 \sim 2500$ pC
Self trigger	Built-in discriminator
Number of input channels	3
Processing speed	~ 500 ns/cycle
Gain	1/7/49 (3 settings)
Charge resolution	0.05 p.e. (< 25 p.e.)
(Non-) Linearity (Q)	$< 1\%$
Timing resolution	0.3 ns (1 p.e.$= -3$ mV), 0.2 ns(> 5 p.e.)
Power dissipation	< 200 mW/channel

Table 2.7: Characteristics of QTC chips, where. p.e. is denotes photoelectron.

the charge in the capacitor (measure gate). If an incoming PMT pulse exceeds a current threshold, a 400-ns-wide charge gate and a 966- ns- wide measurement gate are generated. Therefore, the width of the output pulse from a QTC chip is 400 and 966 ns, which is proportional to the size of the integrated charge. A reset signal of 34 ns is generated after the measurement gate; thus, the processing time of a QTC chip is 1 μs per cycle. The output pulse from the QTC is fed into a multi-hit TDC, where the timing information of all leading and trailing edges is recorded.

A QTC chip receives three analog inputs and processes each input with one of three gains of 1, 7, and 49. The charge resolution is about $\sim$0.1 pC, and the dynamic range is 0.2$\sim$2500 pC. The timing resolution is 0.3 ns for one photoelectron and 0.2 ns for more than five photoelectrons.

A QBEE board accommodates eight QTC and four TDC chips to process 24 analog inputs. The QBEE board receives an external clock signal of 60 MHz and a periodical trigger signal of 60 kHz from a master clock. The 60- kHz periodical trigger signal initializes the TDC and comes arrives with a timing tag and an event number, which is used to identify the PMT hits in the same trigger. After collecting all the hits, an event is built and selected by software triggers. The adjustable QTC parameters for RENO are the threshold level for a single photoelectron signal and the length of the charge gate and measurement gate.

2.5.3 DAQ System

The RENO DAQ consists of a data readout using front-end electronics, an event builder, software triggers, a data logger, and run-control. Schematic diagrams of the RENO DAQ system are shown in Figs. 2.20 and 2.21.

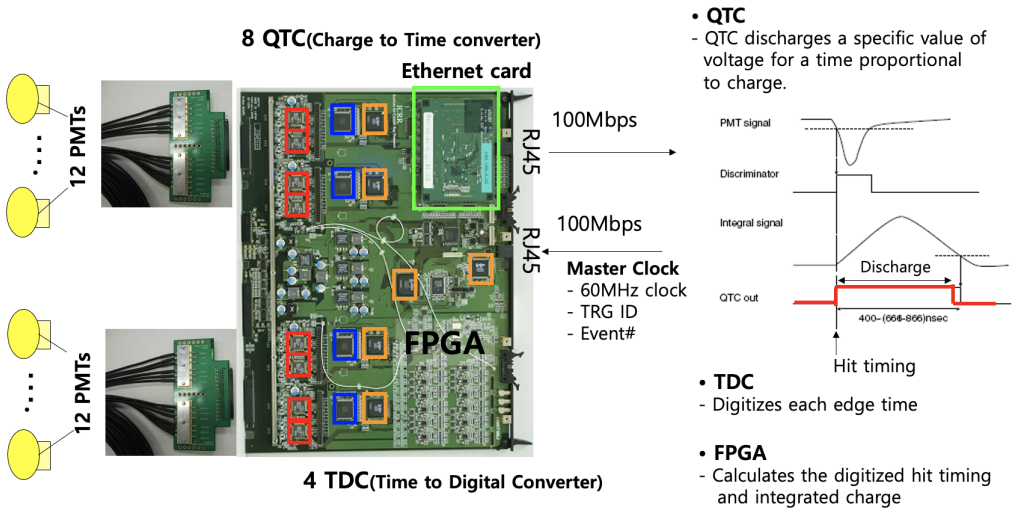

Figure 2.19: Operation logic diagram of the QTC chip and the QBEE board.

Data Readout and Run Control

The front-end electronics for the data readout are based on QBEE boards in the TKO crate and ethernet cards on QBEE. A QBEE board receives 24 analog PMT inputs, digitizes them, and sends the signal outputs to the online computer via a 100 Mbps ethernet card. The RENO experiment uses 18 QBEE boards for 421 channels per detector, and the data throughput rate is about ∼1.8 Gbps per detector. The FD and ND have the same DAQ architecture.

The run control sends commands to DAQ components and makes generates run conditions. Shift crew uses an integrated graphical user interface (GUI), which can be used to select the run mode, trigger type, and detector parameters. The trigger type can be chosen from one of the predefined trigger sets. The detector parameters are high-voltage settings for the PMTs. The "Run Controller" panel is shown in Figure 2.22.

Event Builder

All the QBEE boards are driven by a common 60- MHz master clock (MCLK). A 60 kHz periodical trigger and a serialized 32-bit event number are generated by a trigger module and fanned out via a distributor to all the QBEE boards via network cables. All the hit data are sorted and merged according to the trigger event number and the timing information.

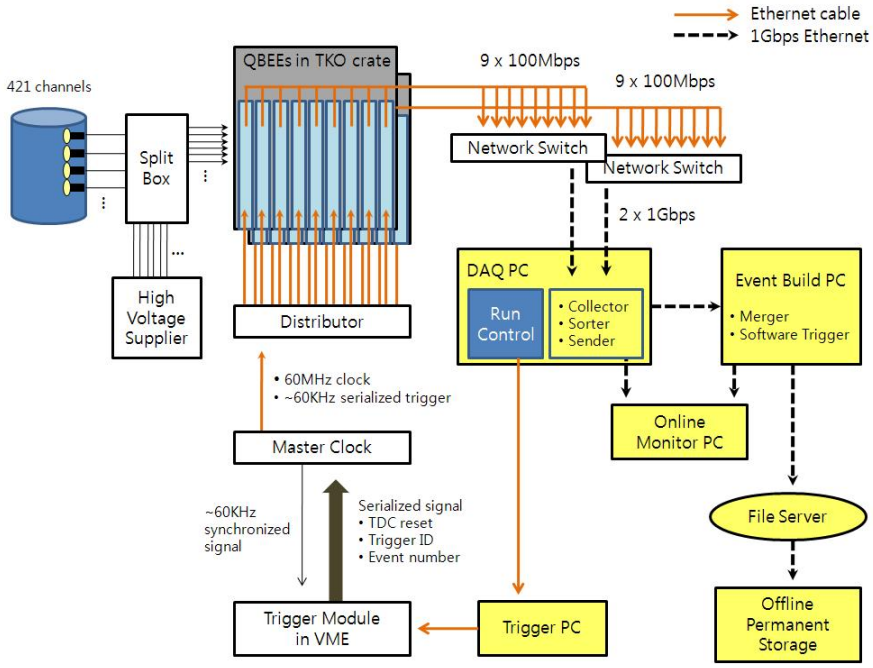

Figure 2.20: Diagram of DAQ system for RENO. There are 18 QBEE boards in two TKO crates collecting the hit signals from 421 PMTs (354 PMTs in the inner detector and 67 PMTs in the veto). The FD and ND have the same DAQ architecture.

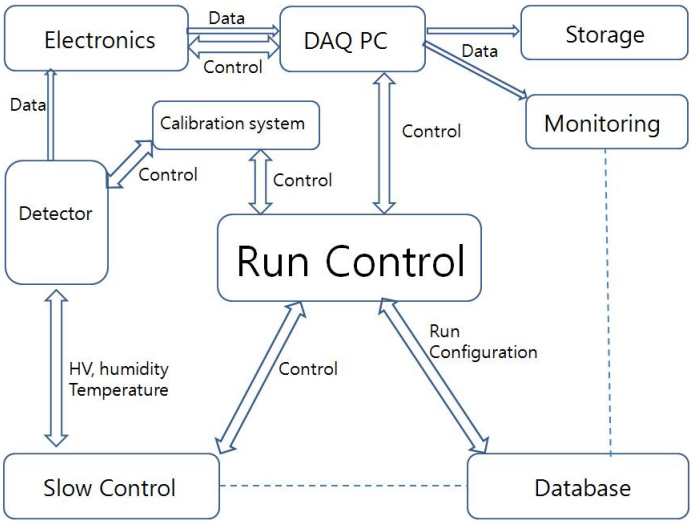

Figure 2.21: Flow diagram of run control for RENO. The run control sends commands to the DAQ component and generates run conditions. Operators use integrated GUI.

A periodic trigger of 60 kHz makes creates a data block of hits. The order of the data blocks is determined according to the event number. The hits in a data block are sorted by their hit time and merged. The hit data in the same block are merged, sorted by hit time, and stored with an event number. An event builder constructs events by applying a software trigger to the merged hit data. Before the software application triggers the merged data, the merged data are stored for several days and used for monitoring purposes.

Software Trigger

The software triggers are applied to the events constructed by the merger to identify neutrino candidate events, cosmic muon events, or calibration events. The software trigger calculates the total number of hits (multiplicity) within a 50 ns time window and constructs an event if the sum of the hits exceeds a certain threshold number. The threshold number of the event is 90 hits (corresponding to ∼0.5∼–0.6 MeV) for the inner detector (ID) trigger and 10 hits for the outer detector (OD) trigger from the first data taking acquisition in Aug. 2011 to May. 2017. Since June. 2017, the ID trigger threshold number has been changed to 80 hits. The decrease of the Gd-LS attenuation length and the PMT coverage due

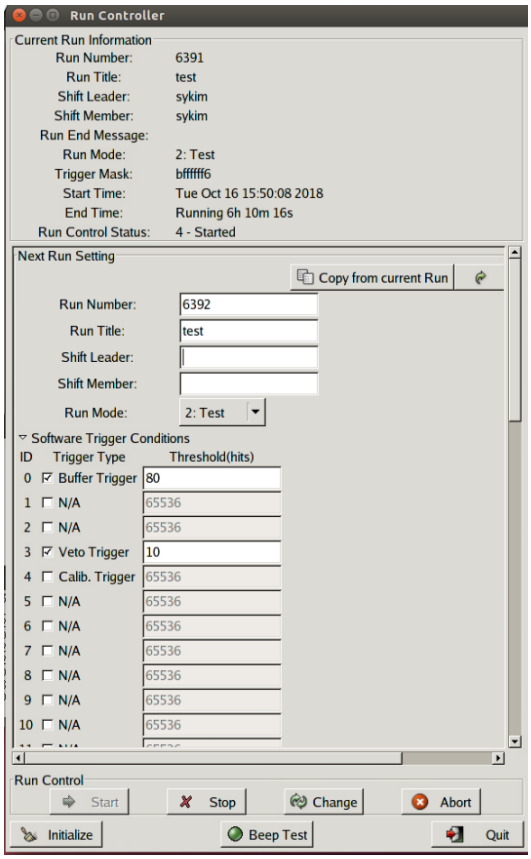

Figure 2.22: Display of the run control panel, where run mode and data acquisition conditions can be selected.

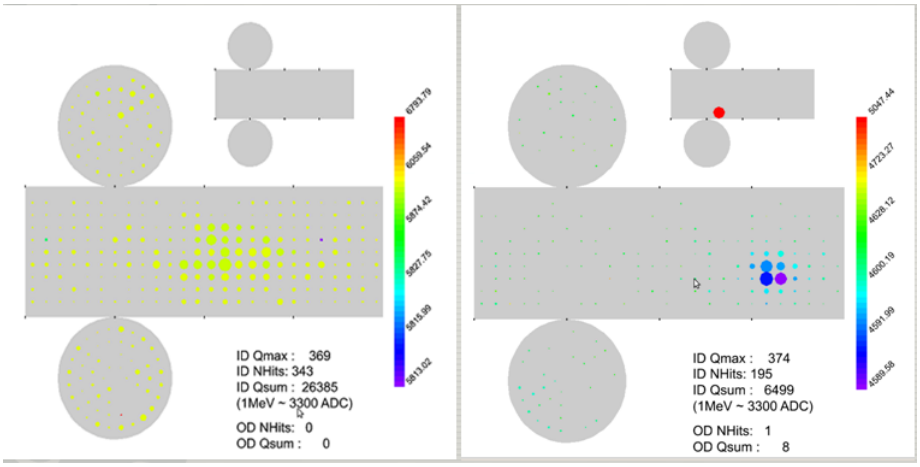

Figure 2.23: RENO event display. The center of the circle indicates the PMT that was hit, the size of the circle is proportional to the charge of the hit, and the color corresponds to the time of the hit.

to the withdrawal of broken PMTs resulted in a decrease in the number of the detected photoelectrons and trigger inefficiency at low-energy for the threshold of 90 hits. The time of the first hit time in an event is set to T_0, and the time windows before and after T_0 determine an event gate by software triggers. All PMT hits within this event gate create an event and calculate the sum of charges in the time gate (approximately -100–50 ns).

2.5.4 Slow Control and Monitoring system

An online monitoring computer, located in the control room, reads the data from the DAQ host computer via the network. It provides event display and online histograms to monitor the detector performance and a variety of additional tasks needed for the efficient monitoring of the detector performance parameters and for diagnoses of malfunctions of the detector or the DAQ system.

The event display shows the charge and hit time information of the trigger for an individual PMT in real-time, as shown in Figure 2.23. The center of the circle indicates the PMT that was hit, the size of the circle is proportional to the charge of the hit, and the color corresponds to the time of the hit.

The online histograms show the accumulated condition of the DAQ system: the channel of the ID and OD PMT that was hit, the number of hits of the trigger, and trigger histograms. The operators can recognize any problem in the DAQ system from the online histograms. Figure 2.24 shows the online histogram

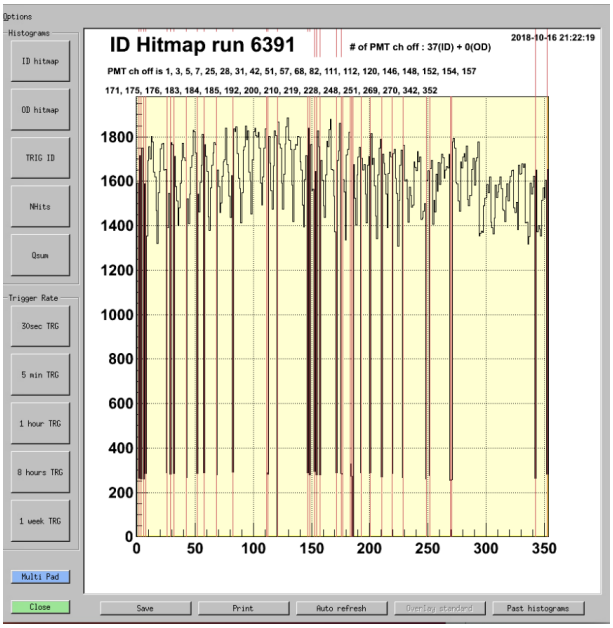

Figure 2.24: Online histogram panel.

panel.

The slow control monitors the status of the high-voltage (HV) systems, the temperature of the electronics crates and detectors, fluids levels, and humidity. In addition, the slow control is able to feed HV for each channel and turn on and off HV remotely. The slow control scheme is shown in Figure 2.25.

High voltage (∼1700 V) is required to be supplied to the PMTs. A nine 48-channel power supply module (A932AP) in two crates (SY1527), manufactured by CAEN S.p.A., is used at both detectors. The supplied high voltage (HV) value must be stable and monitored by shift crew operators. For this purpose, the high voltage monitoring system based on Labview was developed, as shown in Figure 2.26. Colors display the status of each high voltage (HV) channel. The PMTs that provide abnormal signals or highly flashing are disconnected and indicated as black circles, as shown in Figure 2.26.

The experimental environmental conditions, such as temperature and humidity, also should are required to be stable during the data acquisition as well. To prevent damage to the electronics from the humidity and temperature, an air conditioner and a dehumidifier are installed in the experimental hall, the electronics hut, and the control room. To monitor the temperature, three thermocouples inside the detector and two thermocouples in the electronics hut and in the control

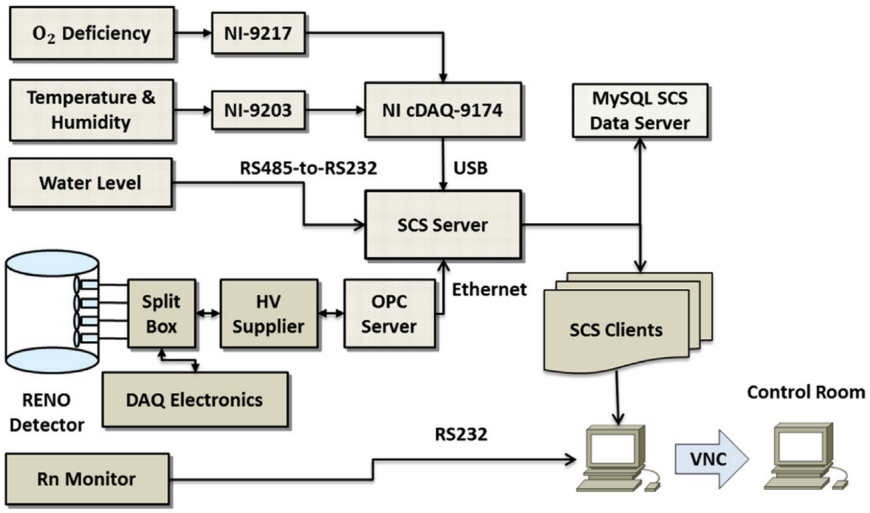

Figure 2.25: Diagram of slow control. The slow control system monitors detector conditions and controls the PMT HV power supplies of the PMT.

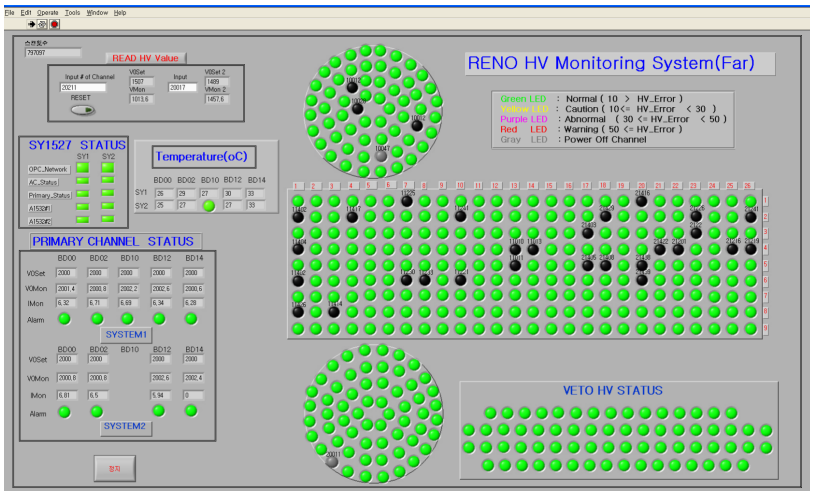

Figure 2.26: RENO HV monitoring system. The broken or highly flashing PMTs are disconnected and indicated by black circles.

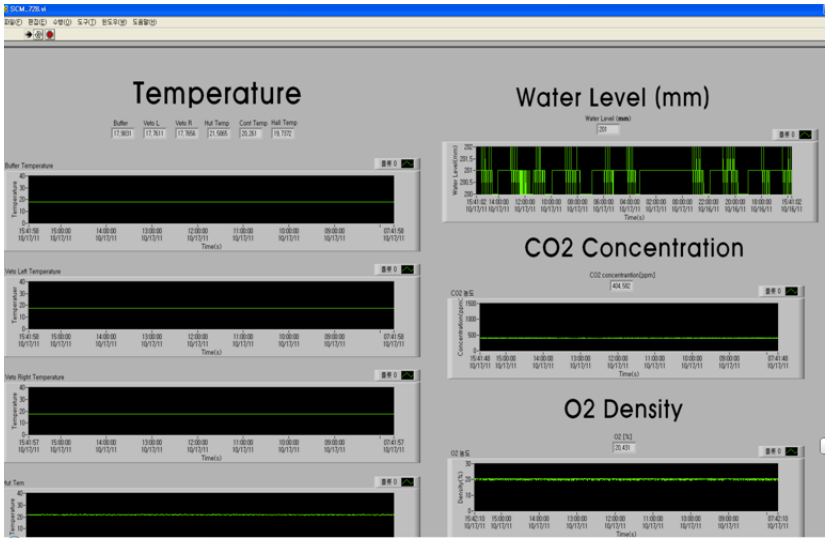

Figure 2.27: RENO slow monitoring system. The temperature, humidity, O2, CO2 and Water levels in the OD are monitored.

room are installed. The humidity is also monitored by a sensor. For safety reasons, O_2, CO_2, and Ra sensors are installed. The veto is filled with pure water for the Cherenkov radiation. The water is required to be purified to prevent the deterioration of its quality. Thus, the level of filled water is also monitored by a sensor. If the water level reaches the high setting threshold, the water circulation and purifying system pumps out water in the veto region automatically and refills it with purified water. The operators can check all these environmental conditions by the slow monitoring system, as shown in Figure 2.27.

Chapter 3

Expected Reactor Antineutrino Events

3.1 Reactor Antineutrino Flux and Spectrum

Reactor neutrinos are emitted due to the decay of fission products of fissile isotopes in the reactor core (Figure 3.1).

The fissile material in a reactor is mainly composed of ^{235}U and ^{239}Pu, which undergo thermal neutron fission. The dominant ^{238}U is fissile only for fast neutrons. However, it also undergoes fission by thermal neutron capture and produces ^{239}Pu as a result.

$$n + {}^{238}\text{U} \rightarrow {}^{239}\text{U} \rightarrow {}^{239}\text{Np} \rightarrow {}^{239}\text{Pu}. \tag{3.1}$$

Similarly, ^{241}Pu is generated from ^{239}Pu,

$$n + {}^{239}\text{Pu} \rightarrow {}^{240}\text{Pu} \rightarrow {}^{241}\text{Pu}. \tag{3.2}$$

The contribution of four fissile isotopes, namely ^{235}U, ^{239}Pu, ^{238}U, and ^{241}Pu, is significant, while that of other isotopes is only marginal (0.1%). Fission fragments from these four isotopes sequentially decay and emit electron antineutrinos. The antineutrinos emitted are exceedingly pure, and the electron-neutrino contamination is only at a level of 10^{-5} above the inverse decay threshold of 1.8 MeV.

The fission rates of the four fissile isotopes are shown in Figure 3.2. As shown in Table 3.1, these four isotopes release similar amounts of energy. Therefore, even though the composition of the fissile material in the power plant changes over the refueling cycle, the average mean energy per fission does not change significantly. Assuming approximately 200 MeV per fission, there are 3.1×10^{19} fissions per

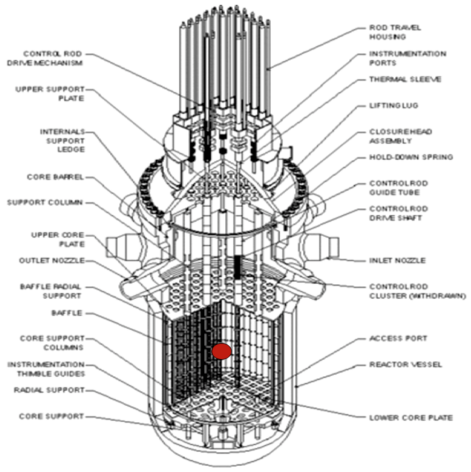

Figure 3.1: A pressurized water plant core. The red dot is the center of the plant fuel.

Isotope	Mean Energy Per Fission (MeV)
^{235}U	201.7 ± 0.6
^{238}U	205.0 ± 0.9
^{239}Pu	210.0 ± 0.9
^{241}Pu	212.4 ± 1.0

Table 3.1: Mean energy emitted per fission of four main isotopes

GW_{th}. Because one fission results in an average of six neutrino emissions above 2 MeV, the neutrino intensity can be estimated to be 2×10^{20} /(GW_{th} s). Because the neutrinos are radiated isotropically from the plant core, the inverse square law applies to neutrino intensity at a distance. The neutrino energy spectrum from a plant is shown in

These four isotopes of the reactor fuel β-decay at various energy levels, and their neutrino spectra are different, as shown in Figure 3.3.

The neutrino energy spectra from fission processes are parameterized in Refs. [65, 66] using

$$\phi_\nu^{(j)} = exp\left(\sum_{i=0}^{5} a_i^{(j)} E_\nu^i\right) \tag{3.3}$$

where $a_i^{(j)}$ are the fitting parameters for the jth isotope and E_ν is neutrino energy

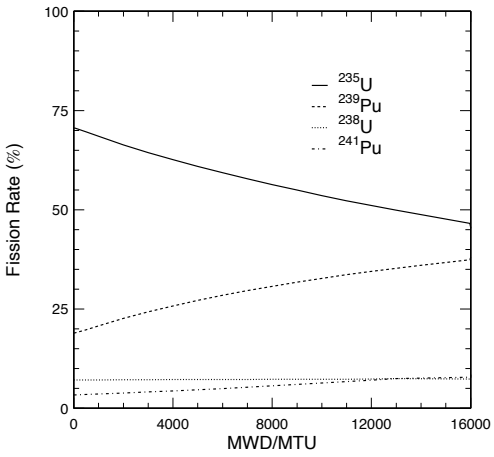

Figure 3.2: The evolution of the fission rate of the four dominant fissile isotopes of a typical refuelling cycle.

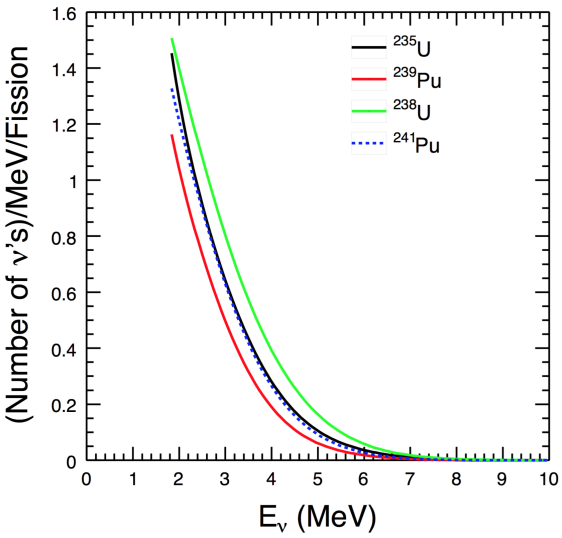

Figure 3.3: The neutrino spectra from fission of four isotopes

in MeV. The results are shown in Table 3.2 and Figure 3.3.

Parameter	^{235}U	^{238}U	^{239}Pu	^{241}Pu
a_0	4.367	4.757	4.833×10^{-1}	2.990
a_1	-4.577	-5.392	1.927×10^{-1}	-2.882
a_2	2.100	2.563	-1.283×10^{-1}	1.278
a_3	-5.294×10^{-1}	-6.596×10^{-1}	-6.762×10^{-3}	-3.343×10^{-1}
a_4	6.186×10^{-2}	7.820×10^{-2}	2.233×10^{-3}	3.905×10^{-2}
a_5	-2.777×10^{-3}	-3.536×10^{-3}	-1.536×10^{-4}	-1.754×10^{-3}

Table 3.2: Parameters of the 5th order polynomial for the neutrino flux from the dominant isotopes in the nuclear fuel. Parameters for isotopes ^{235}U, ^{239}Pu, and ^{241}Pu are taken from Ref. [66]and ^{238}U from Ref. [65]. The resulting distributions are shown in Figure 3.3

The fission rate in a plant with a power P_{th} is

$$n_{fis} = \frac{P_{th}}{\sum_i f_i \bar{E}_{fi}}, \tag{3.4}$$

where f_i and $\bar{E}_{fi}$ are the fission fraction of the nuclear fuel and the mean energy released per fission of isotope i, respectively, given in Table 3.1, and P_{th} is the plant power. Then, the number of fissions per second, n_{fis}, is related to the plant power by $(6.24 \times 10^{18}) \cdot n_{fis}$, where P_{th} is in Watts and E_{fi} in eV, as seen in Eq. 3.4.

The number of neutrinos with energies between $E_{\min}$ and $E_{\max}$ from the fission process of the ith isotope is

$$N_\nu = n_{fis} \cdot \sum_i f_i \int_{E_{\min}}^{E_{\max}} \frac{dN_\nu^{(i)}}{dE_\nu} dE_\nu \tag{3.5}$$

The neutrino flux, which is isotropic about the source, at a distance r is

$$n_\nu(r) = \frac{1}{4\pi r^2} N_\nu. \tag{3.6}$$

3.2 Yield of Reactor Antineutrino Events

The expected rates and spectra of the plant antineutrinos are calculated for the duration of the data extraction by taking into account the varying thermal powers, fission fractions of four fuel isotopes, energy release per fission, and fission and

capture cross-sections. The equation to calculate the expected antineutrinos in the detector d is as follows.

$$N_\nu^d = \frac{N_p}{4\pi R^2} \frac{\sum_i \alpha_i \bar{\sigma}_i}{\sum_i \alpha_i E_i} P_{th} = \frac{N_p}{4\pi R^2} \frac{\bar{\sigma}_5 \left[1 + \sum_i \alpha_i \left(\bar{\sigma}_i/\bar{\sigma}_5 - 1\right)\right]}{E_5 \left[1 + \sum_i \alpha_i \left(E_i/E_5 - 1\right)\right]} P_{th} \tag{3.7}$$

where,

- N_p : the number of total protons.
- R : the distance between the detector and the plant.
- α_i : the fission fraction of the ith isotope. (^{235}U, ^{238}U, ^{239}Pu, ^{241}Pu))
- $\bar{\sigma}_i = \int \sigma\left(E_\nu\right) \phi_\nu^{(i)} dE$: A total number of IBD events per fission is produced in a detector for the ith isotope.
- $\bar{\sigma}_5$: $\bar{\sigma}$ for the ^{235}U.
- E_i : energy released per fission for the ith isotope.
- E_5 : energy released per fission for the ^{235}U.
- P_{th} : plant thermal power generated.

The above expression can also be expressed as

$$N_\nu^d = \gamma \left(1 + k\right) P_{th} \tag{3.8}$$

where, $\gamma = \frac{N_p \bar{\sigma}_5}{4\pi R^2 E_5}$ is a constant for a given detector and geometry, and $1 + k = \left[1 + \sum \alpha_i \left(\bar{\sigma}_i/\sigma_5 - 1\right)\right] / \left[1 + \sum \alpha_i \left(E_i/E_5 - 1\right)\right]$. $1 + k$ is time-dependent because the fission fraction of the four isotopes evolves with time.

The number of target proton N_p

The target free protons are decided by the amount of linear alkylbenzene (LAB) present in the target detector. The free protons and molecular weight of RENO's LAB molecule are 30 and 240.7, respectively, taken from the composition analysis sheet provided by the manufacturer. The density of LAB measured by a densitometer with a resolution of 0.001 is 0.85 g/L. The measured target volume is 18,641 ± 5 L at ND and 18637 ± 5 L at FD. The following equation calculates the total free protons,

$$N_p = \rho N_A V \frac{30}{M_A} \tag{3.9}$$

Where ρ is the density of LAB, N_A is Avogadro's number, M_A is its molecular weight (240.7), 30 is its free protons, and V is the measured volume of the target detector, the calculated target protons are 1.189×10^{30} for both FD and ND, the corresponding uncertainty is 0.5%, and the uncorrelated uncertainty is 0.1%, in the same way, The calculated γ-catcher protons are 2.11×10^{30} for both FD and ND, thus, the number of total protons is 3.299×10^{30}.

Baseline between Detector

The neutrino flux is isotropic about the source, causing the flux to reduce at a rate inversely proportional to the square of the distance. The detector's and the plant's distances are calculated considering each detector's target center and each plant's center. The coordinates of the plant core center and the detector target center were determined from a survey of the national cadastral control points near the power plant and the reactor and detector blueprints. The uncertainties of the baselines are of the order of cm. The distances between each detector and reactor are shown in Table 3.3.

	FD (m)	ND (m)
1^{st} Plant	1563.77	660.06
2^{nd} Plant	1460.83	444.73
3^{rd} Plant	1397.81	301.56
4^{th} Plant	1380.06	339.26
5^{th} Plant	1409.39	519.97
6^{th} Plant	1483.00	746.16

Table 3.3: The distance (m) between each plant and each detector.

Fission Fraction

The fission fractions of the four isotopes evolve with time, and it causes an increment of 1+k over time. The isotope fraction changes the expected reactor neutrino energy spectrum also. The average fission fraction of each plant for ∼2,900 days are summarized in tables 3.4 and 3.5 below.

Plant	U235	U238	Pu239	Pu241
1	0.565	0.076	0.303	0.056
2	0.571	0.076	0.298	0.055
3	0.569	0.072	0.303	0.056
4	0.582	0.072	0.292	0.053
5	0.571	0.072	0.300	0.056
6	0.589	0.072	0.287	0.052

Table 3.4: The average fission fraction of the 4 isotopes for the ND (2,900 days).

Plant	U235	U238	Pu239	Pu241
1	0.567	0.076	0.302	0.056
2	0.574	0.076	0.296	0.054
3	0.570	0.072	0.302	0.056
4	0.580	0.072	0.294	0.054
5	0.569	0.073	0.302	0.057
6	0.585	0.072	0.290	0.053

Table 3.5: The average fission fraction of the 4 isotopes for FD (2,900 days).

Total IBD events produced in a detector per fission for the ith isotopes $\bar{\sigma}_i$

For each isotope, the total IBD events per fission produced in a detector are calculated by convolving the IBD cross-section with the antineutrino energy spectrum, which is the expected energy spectrum of antineutrinos per fission from each isotope, as shown in Fig 3.4.

Energy Released Per Fission E

The mean energy emitted per fission has been calculated [49], the correlated uncertainty is 0.2%, and is summarized in Table 3.1.

Power plant Thermal Power

The maximum thermal power is 2.90 GW_{th} for reactor 1 2 and 2.815 GW_{th} for reactor 3 6. However, the thermal output of the reactors varies as time passing. The thermal power can be calculated by considering the maximum $P_{th}\times$thermal

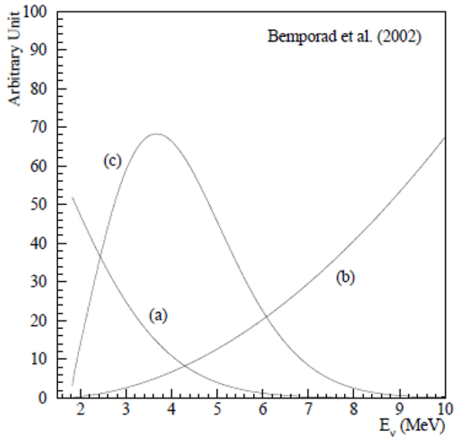

Figure 3.4: Reactor $\bar{\nu}_e$ flux (a), IBD cross-section (b), and interaction spectrum at a detector based on such reaction (c). The cut-off at 1.8 MeV is because of the minimum neutrino energy required for the IBD process.

output (%), which KNHP provides as the daily mean thermal output. The average thermal powers for ∼2,900 days as shown in Table 3.6.

Plant	FD	ND
1	81.32	81.28
2	72.53	72.47
3	76.72	76.65
4	74.79	74.72
5	84.58	84.53
6	82.32	82.26

Table 3.6: The average thermal powers for ∼2,900 days.

Flux Variation Coming from Fuel Burning 1 + k

The increment 1+k is time-dependent as the fission fractions of the four isotopes evolve with fuel burning. Since we were provided with the values of fission fraction and cycle burn-up, determined by the reactor-core simulations of ANC for approximately one month from the Korea Hydro & Nuclear Power Co (KHNP), the everyday 1+k can be predicted by fitting. Figure 3.5 shows the fitting of 1+k for reactor one and cycle 25. The elapsed time (x-axis in Figure 3.5) is calculated

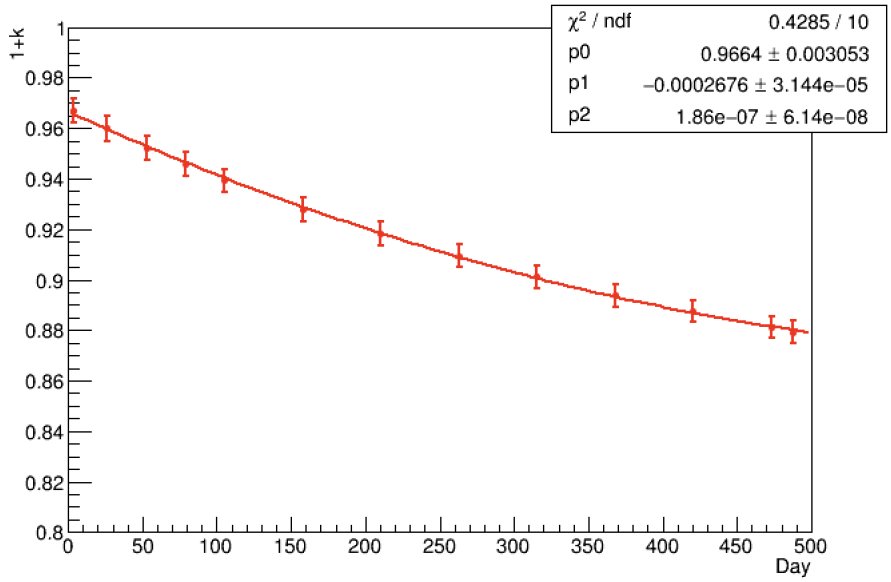

Figure 3.5: Fitting of 1+k factor for reactor 1, cycle 25

by dividing cycle burn-up by the mean daily burn-up.

Calculated Antineutrino Flux N_ν^d for ∼2900days of data

By substituting the quantities obtained above into Eq. 3.9, the expected antineutrino events detected at the detector are determined and summarized in Table 3.7.

Plant	FD	ND
1	100728.5	477930.1
2	107332.6	977032.8
3	109342.2	2015502.9
4	105216.5	1400017.3
5	138878.7	850413.6
6	125530.5	412510.1

Table 3.7: Expected flux for ∼2,900 days of data for FD and ND. The visible energy range is 1.2∼8 MeV

3.3 Expected Reactor Antineutrino Spectrum with Interaction

The expected interaction on the antineutrino spectrum in each detector d can be calculated using the following equation,

$$S_\nu^d = N_\nu^d \left(\sum_i I_i s_\nu^i \right) \tag{3.10}$$

where, $N_\nu^d \left(= \sum_i N_{\nu,i}^d \right)$ is the expected antineutrinos obtained above (where $N_{\nu,i}^d$ is the expected antineutrino of the ith isotope at the detector d) and $I_i \left(= \frac{N_{\nu,i}^d}{\sum_i N_{\nu,i}^d} \right)$ is the fraction of neutrino interaction at the target by neutrino produced by the isotope species i. The average interaction fractions at each plant are summarized in the Table 3.8 and 3.9. And $s_\nu^i \left(= \sigma\left(E_\nu\right) \phi_\nu^{(i)} / \int \sigma\left(E_\nu\right) \phi_\nu^{(i)} dE_\nu \right)$ is the normalized interaction spectrum of the ith isotope, as shown on the plot on the left side in Figure 3.6. From Eq. 3.10, the expected interaction antineutrino spectra are shown in the plots on the middle and right side in Figure 3.6.

Plant	U235	U238	Pu239	Pu241
1	0.607	0.124	0.214	0.055
2	0.612	0.124	0.210	0.053
3	0.612	0.119	0.214	0.055
4	0.624	0.118	0.206	0.052
5	0.614	0.119	0.212	0.055
6	0.629	0.118	0.202	0.051

Table 3.8: The average interaction fraction of 4 isotopes for ND, ∼2,900 days.

Plant	U235	U238	Pu239	Pu241
1	0.608	0.124	0.213	0.055
2	0.615	0.124	0.209	0.053
3	0.613	0.119	0.213	0.055
4	0.622	0.118	0.207	0.053
5	0.612	0.119	0.213	0.056
6	0.626	0.118	0.204	0.051

Table 3.9: The average interaction fraction of 4 isotopes for FD, ∼2,900 days.

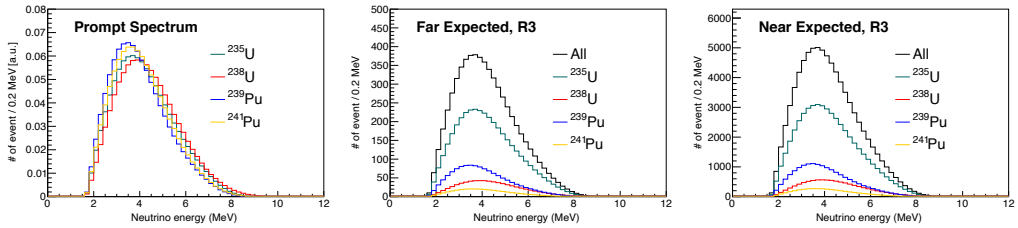

Figure 3.6: Expected interaction spectrum of a neutrino. The left side shows the normalized interaction spectrum for each isotope. The middle shows the expected interaction spectrum of 3^{rd} plant for FD, and the right side shows the same for ND.

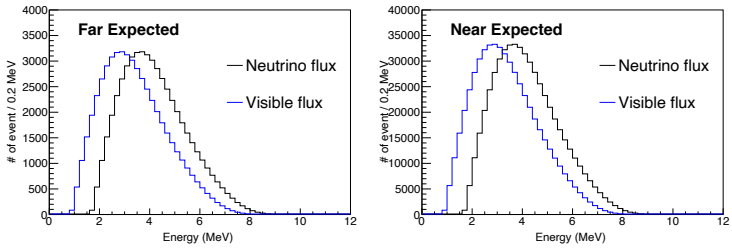

Figure 3.7: Expected neutrino and visible energy spectra. The left plot shows FD, and the right plot shows ND. The black line represents the expected interaction spectrum of a neutrino at the detector. The blue line shows the expected visible spectrum of a neutrino at the detector.

3.4 Prediction of Observed Reactor Antineutrino Spectrum

Systematic uncertainties are of two types: correlated and uncorrelated. The correlated systematic uncertainties and the direction in which they occur are the same for both detectors. Due to identical detector properties, the correlated uncertainties can be canceled out. Uncorrelated systematic uncertainties are independent of each other. Thus, this uncorrelated uncertainty cannot be canceled. The systematic uncertainties of expected reactor neutrino flux and spectrum result from the thermal power output, fission fractions of the four isotopes, the energy released per fission, and capture cross-section. These uncertainties are summarized in Table 3.10.

Parameter	Uncorrelated	Correlated
Baseline	0.03%	-
Thermal Power	0.5%	-
Fission fraction	0.7%	-
Fission reaction cross section	-	1.9%
Reference energy spectra	-	0.5%
Energy per fission	-	0.2%
Combined	0.9%	2.0%

Table 3.10: Systematic uncertainties of Expected Reactor Neutrino Flux

Baseline

The distance from the detector center to the plant fuel center has been precisely measured with an uncertainty below 10 cm. The shortest baseline, between 3^{rd} plant and the near detector, is 301.56 m. Therefore, the maximum systematic uncertainty is $0.1/301.56 = 0.03\%$.

Thermal Power

The plant's thermal power is measured indirectly by calculating the total power supplied at the secondary side of steam generators. The uncertainties of thermal power output are usually less than 0.5% per core and are fully correlated among the plants.

Fission Fraction

The fission fraction uncertainties are summarized in Table 3.11 and shown Figure 3.8.

Isotope	Fractional uncertainty of fission fraction
^{235}U	3.3%
^{238}U	6.5%
^{239}Pu	4.0%
^{241}Pu	11.0%

Table 3.11: Fractional uncertainties of fission fraction

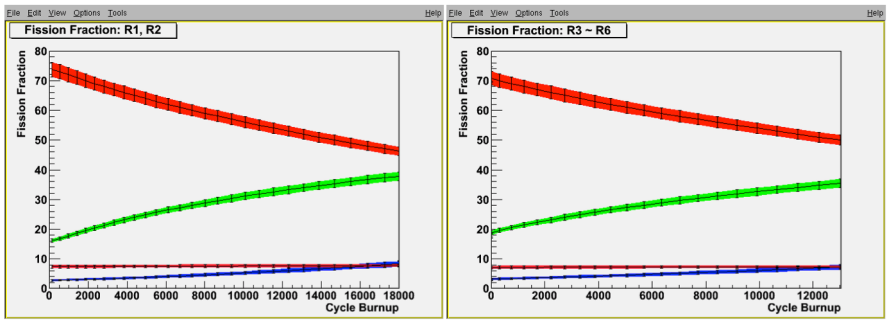

Figure 3.8: Fission fraction variation due to fuel burn-up and its uncertainties. $1^{st} \sim 2^{nd}$ plant and $3^{rd} \sim 6^{th}$ plant have differences, albeit small. The higher red is ^{235}U. Green is ^{239}Pu. Blue is ^{241}Pu. Lower red is ^{238}U.

Fission Reaction Cross Section and Reference Energy Spectra

Associated antielectron neutrino flux gives 1.9% correlated uncertainty, calculated from the neutrino yield per fission and fission spectra.

Energy realsed per fission

As shown in Table 3.1, the thermal energy released per fission gives 0.2% correlated uncertainty.

3.5 Monte Carlo Simulation

RENO has performed extensive studies using Monte Carlo (MC) simulation as with other experiments. The results of MC studies present worthy directions in optimizing and determining the detector design parameters. It helps to obtain the most cost-effective design without compromising the experiment's sensitivity. The MC simulation also helps develop analysis tools. In addition, some systematic uncertainties can also be estimated from the simulation studies. The RENO simulation is modified from GLG4SIM, a geant4-based program for LS neutrino detectors. The "generic" program has been developed with a new event generation that presents better physics models. We can estimate the expected flux of the detector with oscillation from the MC. This flux in turn is used for obtaining θ_{13} and $|\delta m^2_{ee}|$. During the data extraction reported in this manuscript, the dead photomultiplier tube (PMT) fraction is less than 1% for both ND and FD. However, the dead PMTs were not accounted for in the RENO MC because the

time-dependent charge correction in data compensates for the side effects of dead PMTs.

3.5.1 Detector Simulation

The detector simulation's main role is as a data analysis tool. The RENO detector is designed with four concentric cylindrical modules – two active inner modules called target and γ-catcher, and two inert outer modules called buffer and veto, as shown in Figure 3.9. Compared to the past reactor neutrino experiments, an additional active layer, γ-catcher, surrounding the target was added to the detector design to contain γ rays escaping the target. 354 and 67 10-inch PMTs are mounted on the buffer vessel wall and veto wall, respectively, pointing inward, normal to the wall surfaces.

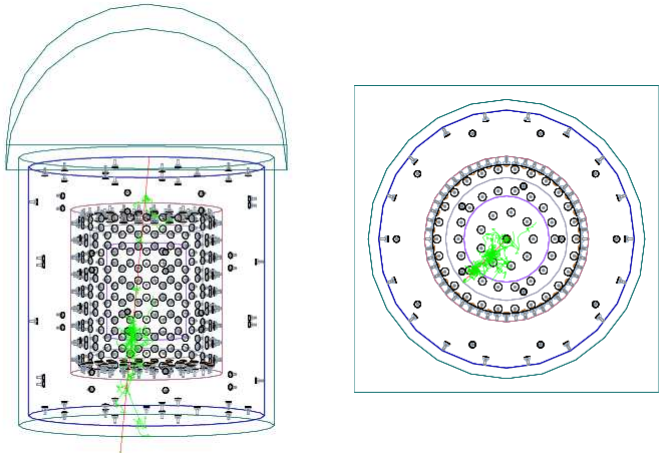

Figure 3.9: Side and top view of the RENO detector simulation with a muon (red line) passes through the target and leaves showers (green lines).

Software Tools

The primary software tool for modeling the RENO detector response, GLG4SIM, is a geant4-based simulation package for LS detectors derived from GLG4sim of the KamLAND collaboration. This software simulated a detailed detector response to particles moving through and interacting with a large volume of LS detectors.

The RENO detector has four concentric cylindrical sub-detectors, each filled with Gd-loaded LS, LS without Gd, mineral oil, and water, respectively. The geant4 toolkits are used for simulating the physics processes involving particles

with energies above a few keV and propagating through the materials in the sub-detectors. However, the optical photon production and propagation through the liquid scintillator, including processes like absorption, re-emission, and elastic collisions, are handled by custom codes on GLG4SIM. In the detector simulation, the LS consists of LAB for the organic solvent, 1.5 g/l of PPO as a fluor, and 0.3 mg/l of Bis-MSB as a secondary-wavelength shifter. In the target region, 0.1% Gd is loaded. geant4 Neutron Data Library (NDL) version 3.8 provides a reasonable approximation for the continuum γ spectrum after neutron capture on Gd. However, the discrete lines of high-energy γs are not included in the NDL version 3.8. However, a GLG4SIM update is available for additional Gd support for accurately modeling discrete lines of the high-energy γ rays. The neutron capture distance and capture time distributions are shown in Figure 3.10. GLG4SIM uses a custom simulation code for PMT with detailed PMT geometries. This PMT simulation handles optical photons' transmission, absorption, and reflection at the photocathode. The PMT modeling includes a finite photocathode thickness and wavelength-dependent photocathode efficiency supplied by the PMT manufacturer.

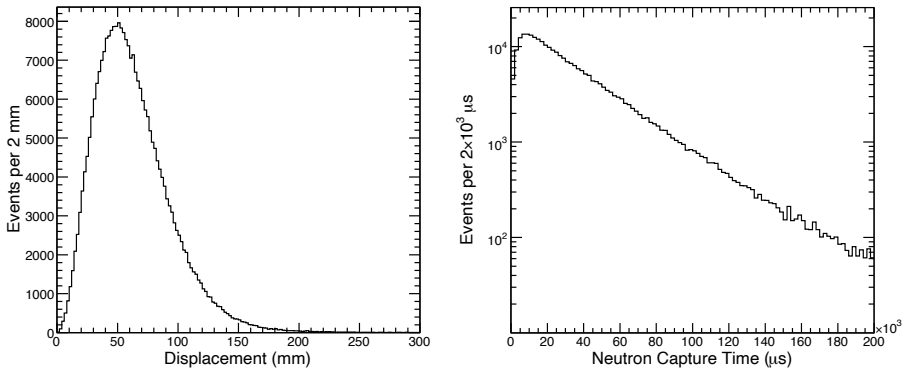

Figure 3.10: Neutron capture distance from IBD events (left) and neutron capture time by 0.1% Gd is $\sim$30 μs(right).

Optical Photon Processes

Each photon in the simulation is tracked in the detector until it reaches a PMT or is lost. The simulation accounts for several light propagation phenomena while tracking the photons. Photons in the scintillator may undergo absorption or elastic scattering (Rayleigh scattering) by solvent and fluor molecules. Attenuation

length, λ_{att}, of the liquid scintillator is defined as

$$\frac{1}{\lambda_{att}} = \frac{1}{\lambda_{scat}} + \frac{1}{\lambda_{abs}}, \tag{3.11}$$

Where λ_{scatt} and λ_{abs} are the scattering and absorption lengths, respectively. The reciprocal value of the liquid scintillator attenuation length ($1/\lambda_{att}^{LS}$) is equal to the sum of those scattering lengths and absorption lengths,

$$\frac{1}{\lambda_{att}^{LS}} = \frac{1}{\lambda_{scat}^{LS}} + \frac{1}{\lambda_{abs}^{LS}} = \frac{1}{\lambda_{scat}^{LS}} + \frac{1}{\lambda_{abs}^{solvent}} + \frac{1}{\lambda_{abs}^{fluors}}. \tag{3.12}$$

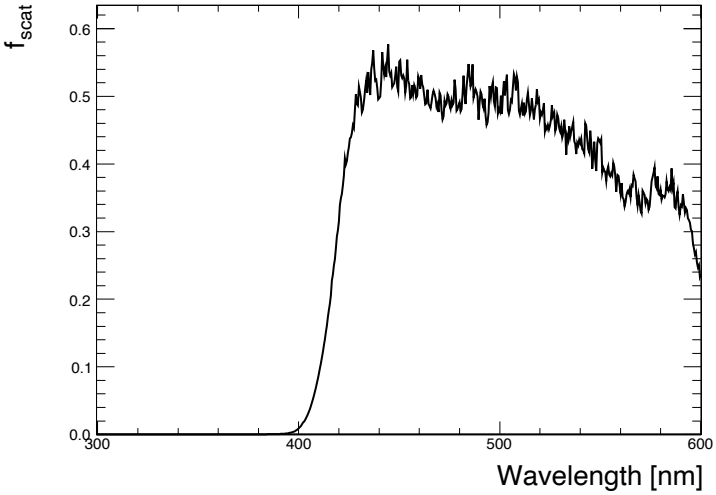

Figure 3.11: Measured scattering fraction of LAB-based liquid scintillator.

In the simulation, photons can be either scattered or absorbed by the solvent and fluors according to the corresponding fractions. Because a large fraction of the liquid scintillator is solvent, photons are scattered mostly by LAB. It should be noted that the bandgap for the lowest-energy electronic transitions in LAB molecules is at 320 nm, and thus absorption by LAB below 320 nm is strong. At wavelengths longer than 320 nm, absorption by LAB drops rapidly, and the measured extinction coefficient roughly demonstrates a λ^{-4} dependence, as expected in Rayleigh scattering. The scattering fraction, f_{scatt}, can be obtained from

$$f_{scatt} = \frac{\lambda_{att}^{LS}}{\lambda_{scatt}^{LAB}}. \tag{3.13}$$

Figure 3.11 shows the measured scattering fraction of an optical photon in the LS. When a photon undergoes elastic scattering, its wavelength remains unchanged, but its direction is altered. The path of a photon after elastic scattering demonstrates a $(1 + \cos^2\theta)$ dependence, where θ is the photon-scattering angle. Absorption of a photon by fluors can be followed by their re-emission, but there is a chance of an absorbing molecule, depending on its quantum yield efficiency, undergoing non-radiative relaxation. The non-radiative relaxation results in the loss of the photon and tracking in the simulation are terminated in such a case. The absorption probability of LAB, PPO, and bis-MSB can be calculated by

$$P^i_{abs} = \frac{\lambda^{LS}_{abs}}{\lambda^i_{abs}}, \tag{3.14}$$

Where i represents LAB, PPO, or bis-MSB. Figure 3.12 shows the measured absorption probability for each component in the liquid scintillator. Re-emission occurs isotropically, and a re-emitted photon is assigned a longer wavelength than the absorbed photon, based on the emission spectrum.

The absorption of photons within the acrylic medium (vessel walls) is simulated according to the absorption probability calculated with the medium's attenuation length. Also, the reflection and refraction of photons at the surface of the acrylic vessel are simulated using Fresnel's law. The detector's refractive indices of all-dielectric materials are measured at different wavelengths and implemented in the simulation. Figure 3.13 shows the measured refractive indices of some of the detector materials. After a photon enters a PMT and is absorbed by the photocathode, tracking is terminated. A hit is then made depending on the quantum efficiency of the photocathode.

3.5.2 Monte-Carlo Event Reconstruction

Vertex Reconstruction

Two independent algorithms, the "charge weighting method" and the "likelihood method," have been used for vertex reconstruction. The charge weighting method is simple and fast and is suitable for event display online or as a filter to extract interesting events to apply more sophisticated event-selection criteria. The likelihood method has a better vertex position resolution than the charge weighting method, but it requires more CPU time and is an offline reconstruction method. The event vertex in the charge weighting method is calculated as

$$\vec{r}_{vtx} = \frac{\sum_{i=PMT} n_i \vec{r}_i}{\sum_{i=PMT} n_i}, \tag{3.15}$$

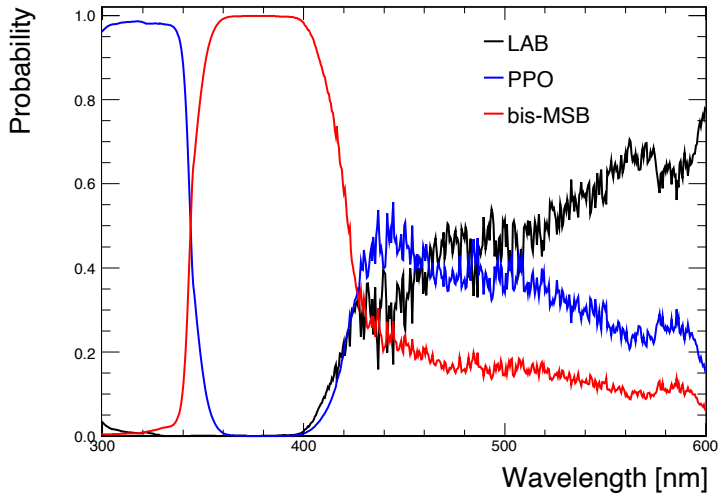

Figure 3.12: Measured absorption probabilities of LAB, PPO, and bis-MSB. These are used in the detector simulation.

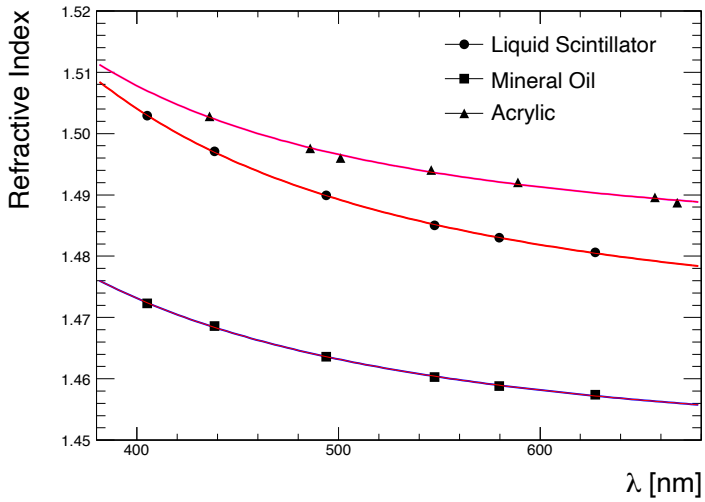

Figure 3.13: Measured refractive indices of liquid scintillator, mineral oil, and acrylic.

Where n_i is the number of photoelectrons on the ith PMT and $\vec{r}_i$ is the vector point from the center of the detector to the ith PMT. The number of photoelectrons is calculated by $n_i = c_i q_i$, where q_i and c_i are the amount of charge measured on the ith PMT and the charge to the number of photoelectron conversion factor on that PMT. Because the reconstructed vertex position calculated with the charge weighting method is inherently closer to the center of the detector than the actual vertex position, linear corrections are applied based on the detector simulation results. The position resolution is found to be ~ 38 cm for a 1 MeV γ-ray as shown in Figure 3.14, and it improves further for a higher energy γ.

The likelihood method uses the number of scintillation photons detected by the PMTs and the arrival time of those photons. The expected number of photoelectrons on the ith PMT can be written as

$$\nu_i = N_{tot} \frac{A_i \cdot f(\cos\theta_i)}{4\pi R_i^2} \epsilon_i \cdot \prod_j e^{-R_{ij}/\lambda_j}, \tag{3.16}$$

where N_{tot} is the generated total optical photons, A_i and ϵ_i are the frontal areas of the cathode, and quantum efficiency of the PMT, respectively, R_{ij} is the distance from the vertex to the PMT in medium j, and λ_j is the attenuation length of the j^{th} medium in between the vertex and the PMT. The effective area of the PMT's photocathode, seen from the incident angle, θ_i is accounted for in function $f(\cos\theta_i)$.

The likelihood is then written as

$$\mathcal{L} = \prod_{i=PMT} \mathcal{G}(n_i, \vec{r}; \nu_i, \sigma_i) \cdot \mathcal{T}(t_i; n_i, R_i), \tag{3.17}$$

where $\mathcal{G}(n_i; \nu_i, \sigma_i)$ is the Gaussian probability with mean, ν_i and width, σ_i. $\mathcal{T}(t_i; n_i, R_i)$ is the probability of having the first hit of n_i hitting the ith PMT to have a hit time of t_i. The observed photoelectrons, n_i, are calculated from the charge output of PMT using the charge-to-photoelectron conversion factor from calibrations. The negative log-likelihood is then minimized using MINUIT to find the vertex position and the created total optical photons.

Energy Reconstruction

To convert p.e. to prompt energy (MeV) for IBD events, we derive the conversion function using the same procedure as the data described in section 5.3. That is, we obtain raw p.e. from ^{137}Cs, ^{68}Ge, H-capture, ^{60}Co, C-capture, and Gd-capture, which are located at the target's center. The following table 3.12. shows the source raw p.e. used for MC energy conversion. One million events are used for n-Gd, and 400,000 events are used for other sources.

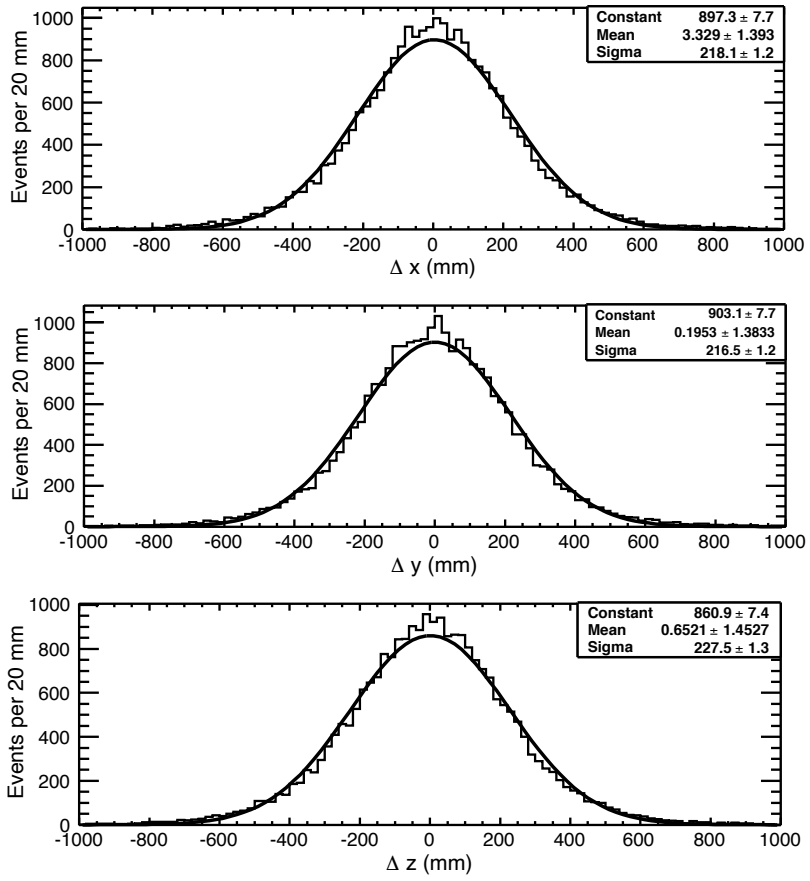

Figure 3.14: Difference between reconstructed and generated vertex positions for 1 MeV γ rays in a random direction in the target using a simple weighting method.

Source	Emission energy	FD raw p.e.	ND raw p.e.
^{137}Cs	0.662 MeV	147.63 ± 0.14	143.45 ± 0.14
^{68}Ge	1.022 MeV	223.37 ± 0.94	216.45 ± 0.94
nH	2.223 MeV	538.26 ± 0.28	522.86 ± 0.28
^{60}Co	2.505 MeV	583.10 ± 1.00	565.94 ± 1.00
nC	4.95 MeV	1226.31 ± 0.61	1191.89 ± 0.61
nGd	7.9 MeV	1931.63 ± 0.95	1880.64 ± 0.95

Table 3.12: MC raw photo electron of calibration sources, which is used for conversion function in the target region.

Based on the corrected raw p.e., we obtain the p.e.-to-MeV conversion function by fitting it with the following function.

$$\text{Function of P.E. / MeV (MeV)} = P_0 - \frac{P_1}{1 - \exp(-P_2 \cdot \text{MeV} - P_3)} \tag{3.18}$$

where, p.e. is the photoelectron, MeV is the prompt energy (MeV), and P_0, P_1, P_2, P_3 are the fitting parameters. The fitting results are shown in Figure 3.15 and Table 3.13.

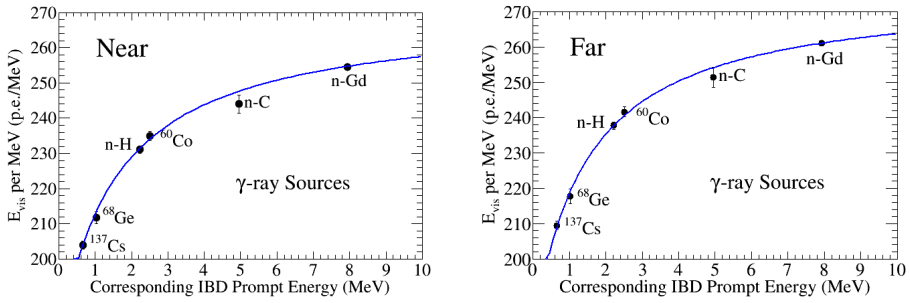

Figure 3.15: Target energy conversion function for MC. The left is ND. The right is FD.

Parameter	FD	ND
P_0	256.19 ± 0.26	249.46 ± 0.26
P_1	0.0118 ± 0.0014	0.0100 ± 0.0090
P_2	0.000208 ± 0.000023	0.000184 ± 0.000166
P_3	0.000156 ± 0.000019	0.000136 ± 0.000121

Table 3.13: The fitting results of energy conversion function for target

Source	Emission energy	FD raw p.e.	ND raw p.e.
^{68}Ge	1.02 MeV	244.365 ± 0.564	
nH	2.223 MeV	571.110 ± 1.580	576.057 ± 0.794
^{60}Co	2.506 MeV	653.744 ± 1.650	655.237 ± 1.033
nC	4.95 MeV	1341.259 ± 6.591	1345.35 ± 1.832

Table 3.14: MC raw photo electron of calibration sources, which is used for conversion function in catcher region.

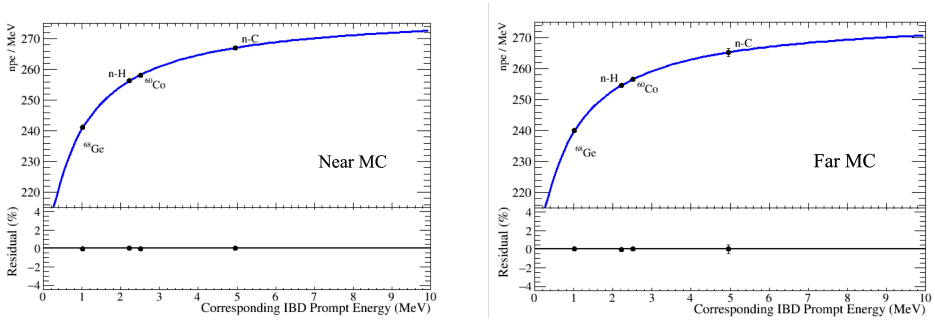

Figure 3.16: Catcher energy conversion function for MC. The left is ND. The right is FD.

Parameter	FD	ND
P_0	277.072 ± 2.71521	278.951 ± 1.43729
P_1	0.01849 ± 0.00306	0.01877 ± 0.05732
P_2	0.00027 ± 0.00006	0.00027 ± 0.00084
P_3	0.00022 ± 0.00005	0.00021 ± 0.00065

Table 3.15: The fitting results of energy conversion function for catcher

3.6 MC expected prompt and delayed spectra

MC Prompt Energy Spectrum

We have also tuned the MC parameters and obtained MC conversion for each detector. The energy resolution correction factor was also obtained. We can produce an MC energy spectrum to compare. Figure 3.17 shows the final reconstructed MC spectrum with oscillation and no oscillation effect.

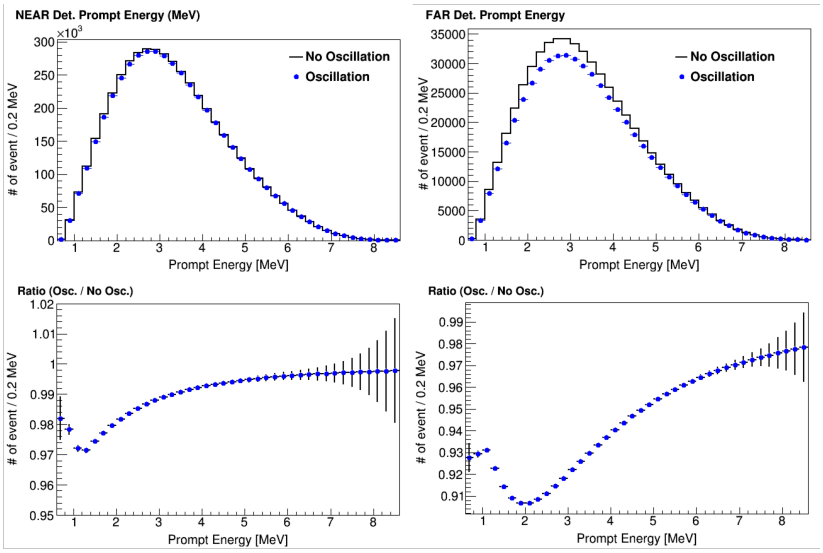

Figure 3.17: MC prompt energy spectrum with oscillation and no oscillation effect, reconstructed after applying an energy-resolution correction. Far MC spectrum is shown on the right. The near MC spectrum is shown on the left.

Chapter 4

Event Reconstruction

IBD signal is a pair of prompt and delayed signals. The prompt signal energy is below 12 MeV, and the delayed signal can be produced by a neutron captured on Hydrogen (H) or Gadolinium (Gd). The corresponding energy is 2.2 MeV or ∼8 MeV. Thus, reconstructed energy and vertex are crucial for identifying the IBD candidate events against various backgrounds.

4.1 Energy Reconstruction

Before data taking, to remove noise, we set the discriminator threshold for collecting real events. We compared single photon electrons with different threshold values. Figure 4.1 shows the charge distribution depending on different thresholds. No significant variation with the threshold values was checked. Thus we chose the highest value, -1.0 mV, to remove lower the background efficiently. The PMT gain value is set for 1.0×10^7. When a single photo-electron enters a PMT, the DAQ estimates 1.6 pC from the hit signal. For efficient gain settings, we placed the ^{137}Cs radioactive source in the center of each detector. With 354 PMTs in buffer and ^{137}Cs source producing around 120∼130 hits, the ^{137}Cs gave an almost single photoelectron response at each PMT. To find the exact values for the gain setting, we checked data with four different high voltages – 1,400, 1,500, 1,600, and 1,700 V – and fitted the results together with the gain function.

$$\text{PMT Gain} = A \cdot V^N \tag{4.1}$$

where V is the power-supplying voltage for PMT. A and N are the fitting parameters. From the results, we determine the exact power-supplying voltage for PMT that gives 1.0×10^7 gain. Figure 4.2 shows an example of a fitted channel. After analyzing all PMTs, we set a power-supplying voltage for each PMT channel and

re-gather data to cross-check the setting. Figure 4.3 shows the result. The X-axis corresponds to gain matching. The variation among PMTs is below 3%.

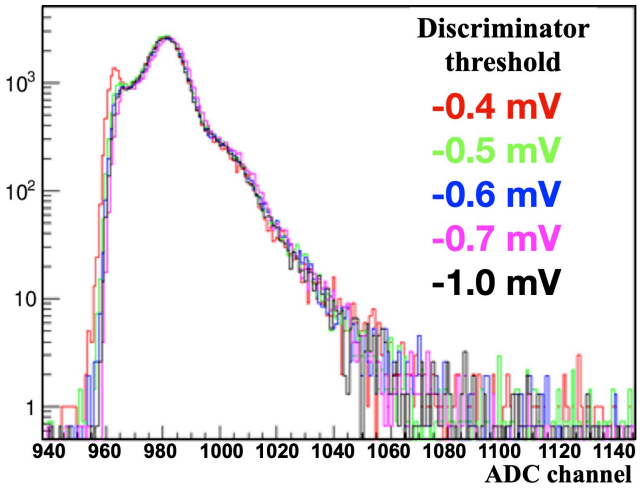

Figure 4.1: Charge distribution (ADC channel) of single photoelectron. Different threshold shows almost similar shape.

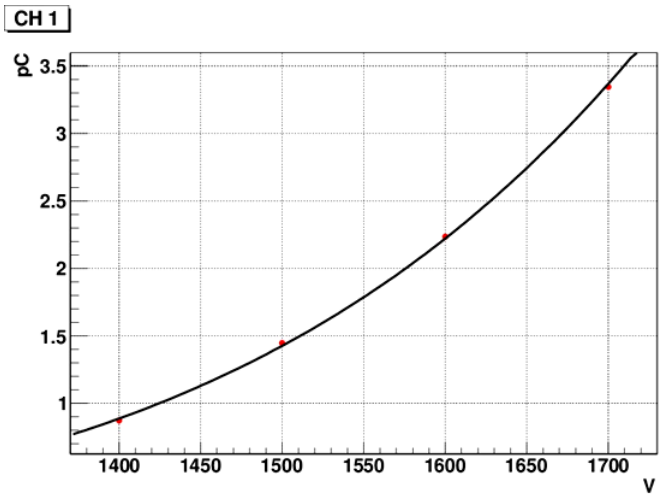

Figure 4.2: Fitted plot with four high voltages. The X-axis corresponds to the power-supplying voltage for each PMT, and Y-axis corresponds to the response value of charge (pC). 1.6 pC is a demanding gain matching.

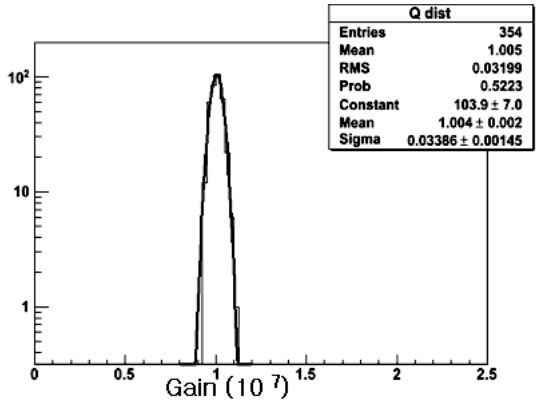

Figure 4.3: Cross check after PMT gain matching is shown. The deviation among PMTs is below 3% at FD and ND.

4.1.1 Charge correction

In the RENO detector, delayed signals of n-H and n-Gd emit specific energy, which is suitable for monitoring and calibration. The γ-catcher can adapt to n-H data for calibration because of no n-Gd events in the region. The energy can be measured by the total hit charges of PMTs. An n-H charge decreased with time, as shown in Figure 4.4. Because the attenuation length of the liquid scintillator shows a tendency to decrease slightly with time, and some dead PMTs are removed. The real n-H energy can not be decreased. Thus, the observed charge is required to be corrected for analysis. The correction method is a simple multiplication of a correction factor, the decreasing ratio as below.

$$\text{Correction factor} = \frac{\text{Mean}_{\text{ref.}}}{\text{Mean}_{\text{periods}}} \tag{4.2}$$

, where is Mean_ref. is reference value in table 4.1. and Mean each period is measured charge of n-H delayed signal in each term. Because the same energy conversion function is adapted for all periods, the corrected Mean_period should be the same as Mean_ref.. When the correction factor is applied to each term using Eq. 4.2, it should be stable with time, as shown in Figure 4.5. However, the corrected points' deviation is large, meaning simple multiplication is not enough for correction.

	FD	ND
Reference (npe)	578.462 ± 4.247	564.243 ± 4.099

Table 4.1: Charge correction reference value. The reference value is the measured charge of the delayed signal of November 2011 data

Using the uniformity property with IBD events, the target region is additionally corrected with spatial factors using n-Gd delayed signal events in certain periods. Accordingly, the γ-catcher region is also checked with the charge deviation for each cell with time. The γ-catcher region is divided into 13 areas, as shown in Figure 4.6. After correction, most of the cells are comparable to the reference value, which is the period of the first 500 days. Some cells fluctuate $\sim$5% after the 500 days. Thus, in the period after the 500 days, γ-catcher should be applied spatial charge correction.

The spatial charge correction factors have affected the vertex with time. The spatial charge corrections are transformed into a continuous correction map developed by interpolating each cell. After spatial correction, the measured charge values become more uniform in all areas, as shown in Figure 4.7.

The simple multiplication of the first charge correction is not regarded as spatial dependence. When spatial charge correction is applied, the measured charge changes uniformly in all regions. Due to a large deviation of charge stability after spatial correction, we apply additional correction, which is second charge correction. The second correction is similar way as the first charge correction. The stability of delayed charges with time is changed more stable after second charge correction, as shown in Figure 4.8

Because of the decreasing charge and non-uniformity of the vertex, the energy resolution was worse. After adopting the 3 processes of correction, the energy resolution is almost reinstated after the 500 days period, as shown in Figure 4.8

4.2 Muon Energy Reconstruction

Cosmogenic muons introduce the main background in the IBD candidates. The intrinsic muon energy cannot be reconstructed, but its deposited energy inside the detector can be reasonably measured as visible energy proportional to its path length [67]. The muon deposit energy (E_μ) is reconstructed by the measured $Q_{\rm tot}$ with a conversion factor of 250 photoelectrons per MeV. A muon is identified in an event with deposited energy greater than 70 MeV. Due to the saturation of the DAQ electronics, however, the muon deposit energy cannot exceed the maximum value of $\sim$1,700MeV. The charge correction method basically multiplies the observed charge by a correction factor, as below.

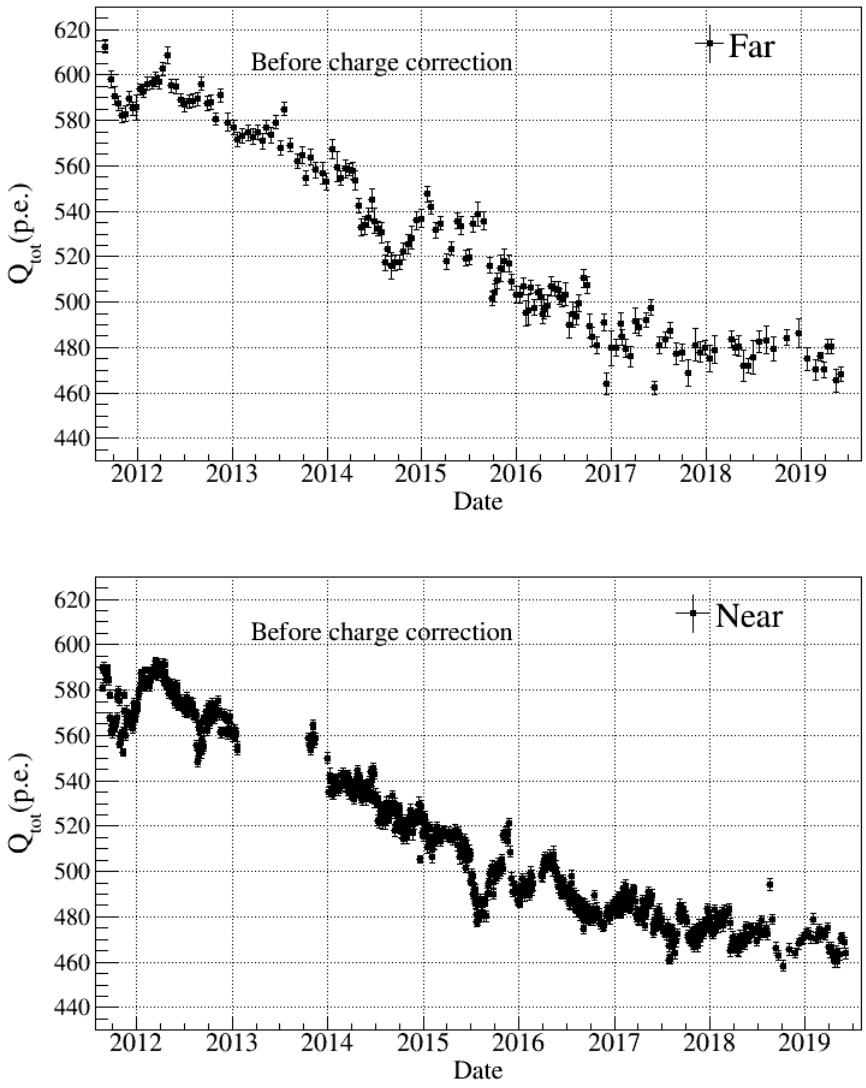

Figure 4.4: Raw charge stability at FD and ND. Some ND data points around the 2013 year elapsed time are excluded due to UPS noise, which is explained in the next chapter.

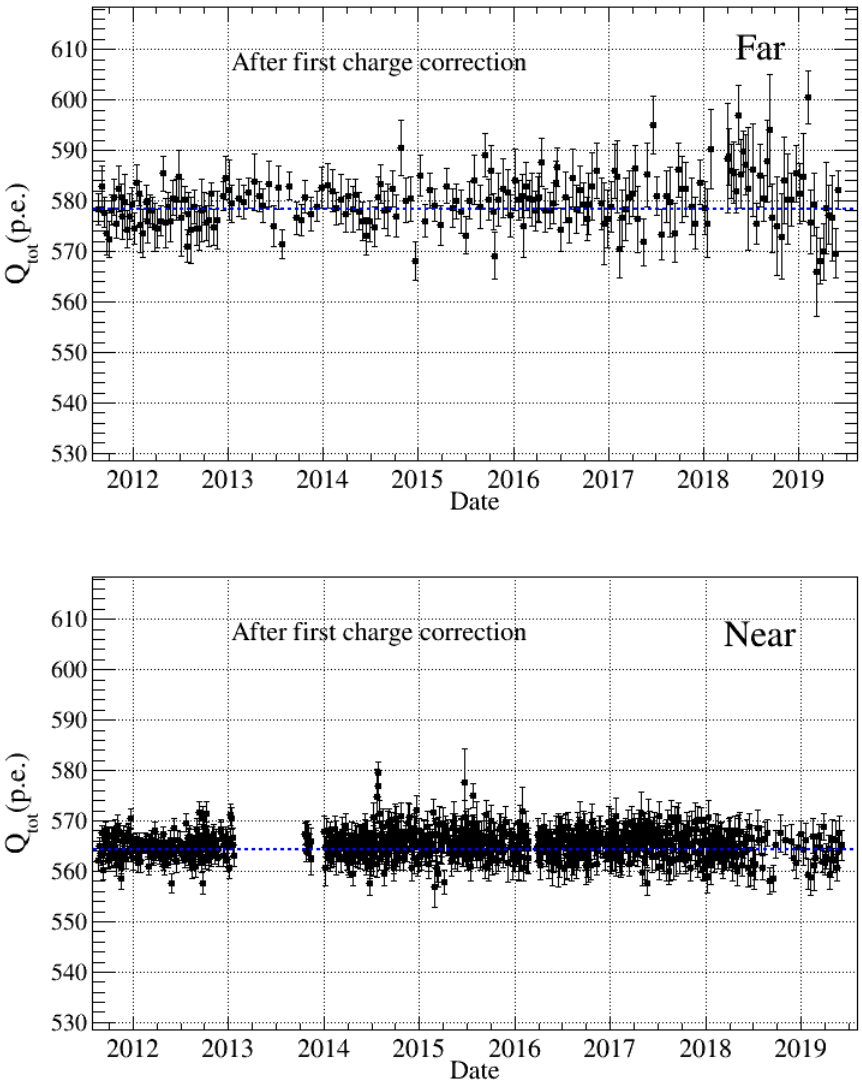

Figure 4.5: First charge correction result. The charge distribution of stability in γ-catcher at FD and ND. The reference charge correction values are blue dashed lines, listed in table 4.1

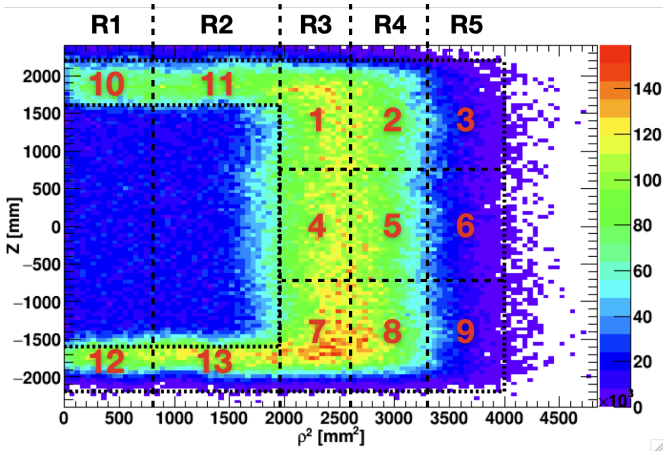

Figure 4.6: Cell Definition for spatial charge correction. The colors represent a density of IBD candidates of n-H. R1, R2, R3, R4, and R5 are categorized in a certain range of radius (ρ). The blue area in the center is the target, and the white color of the outer region is the buffer filled with non-scintillating oil.

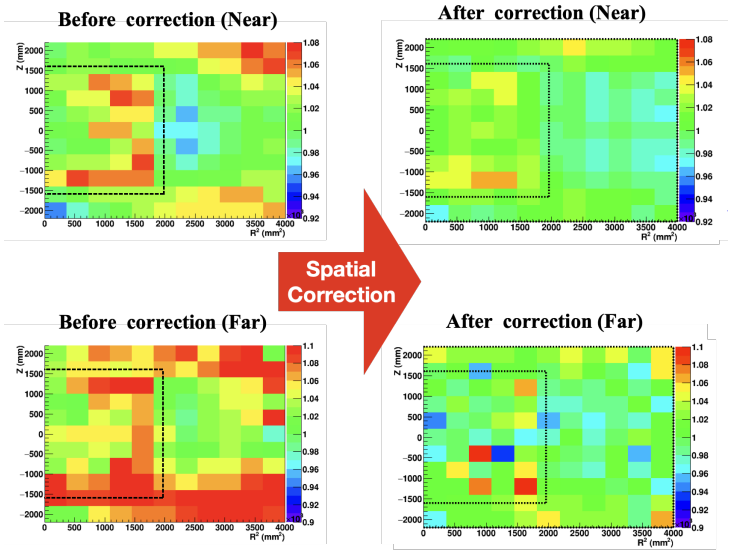

Figure 4.7: The spatial charge distribution of delayed signals. The colors represent Q_ref./Q_mean. When the color changes closely to more green, the charge distribution is changed to more uniform in space.

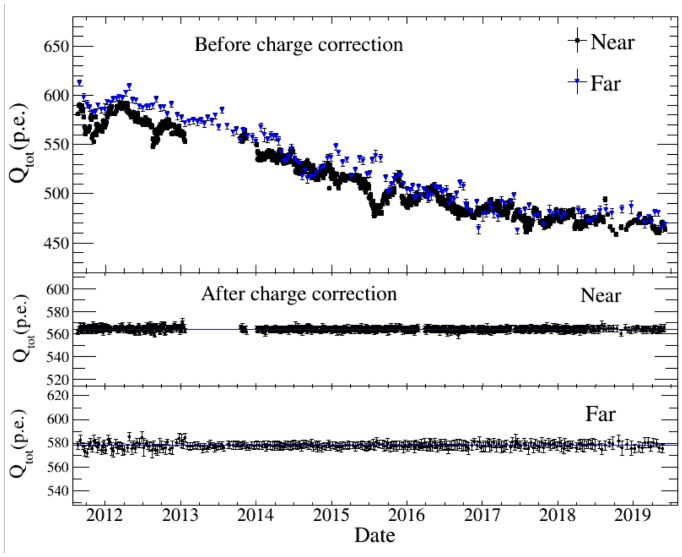

Figure 4.8: Charge stability of γ-catcher after all charge correction for FD and ND. The measured charges are well consistent with the reference value (blue) after all corrections.

Due to a decrease in the attenuation length of Gd-LS and the removed malfunctioning PMTs, the muon deposit energy spectra vary, and the muon rates are reduced. The muon charge correction is designed to fit both muon energy spectrum and muon rate with a reference for high muon energy region ($E_\mu >$ ~1.0GeV). Figure 4.9 and 4.10 show the corrected muon deposit energy spectrum and the stability of the muon rate.

4.3 Vertex Reconstruction

Due to the uncorrelated distances between prompt and delayed candidates, the vertex of IBD candidate events is valuable to remove accidental backgrounds. A low MeV photon in the liquid scintillator loses most energy within a small space. Thus, the optical photons emerging from scintillation processes would be greatly constrained within the vertex point. The optical photons can travel freely without the affection of detector materials, and the uniformly arranged PMTs information can reconstruct an event point using each hit charge of PMT as a weighting factor to estimate. A value of reconstructed vertex, $\vec{r}_{\rm vtx}$, is procured as

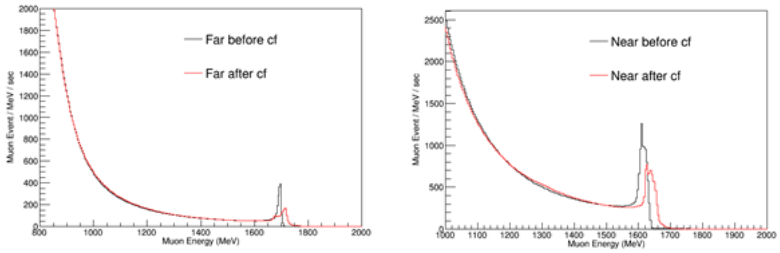

Figure 4.9: Corrected muon deposit energy distribution. The left side is FD, and the right side is ND. The black distribution is data before ^{252}Cf contamination as the reference. Muon energy spectra after ^{252}Cf contamination (red) are good agreement with the reference (black) within the high-energy region($E_\mu >$ ~1.0GeV).

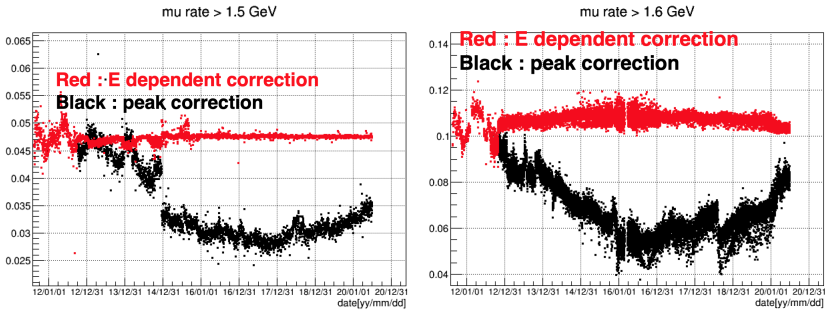

Figure 4.10: muon event rates stability. The left side is for FD data, and the right side is for ND. Non-corrected muon event rates grow lower (black dots). The corrected muon event shows a constant event rate (red dots).

a charge weighted average of all PMTs hit points [68],

$$\vec{r}_{\rm vtx} = \frac{\sum_i (Q_i \cdot \vec{r}_i)}{\sum_i Q_i} \tag{4.3}$$

where Q_i is the collected charge by the i^{th} PMT, and $\vec{r}_i$, is a position vector of the PMT from the center of the RENO detector. This method produces an $\vec{r}_{\rm vtx}$ with a position-dependent offset from the actual vertex position, mainly due to geometric effects. If the detector is spherical, then $\vec{r}_{\rm vtx}$ will be the actual vertex with a correction factor of 1.5 at every point in the detector. However, the RENO detector has a cylindrical shape, and the correction factor varies depending on the location of the event vertex. The correction factor according to $\vec{r}_{\rm vtx}$ is obtained using simple numerical calculations that take into account the simple geometry of the detector and the effective attenuation length of the ID material. RENO detectors' correction factors are calculated using simple Monte Carlo calculations. Assuming that the surface of the cylinder is a photosensitive area with uniform efficiency, in the Eq. 4.4, the Q_i as a unit area can be written,

$$Q_i = \frac{(\vec{r}_i - \vec{r}_{\rm o}) \cdot \hat{\nu}}{|\vec{r}_i - \vec{r}_{\rm o}|^3} \exp(-|\tilde{\rm r}_{\rm i} - \tilde{\rm r}_{\rm o}|/\lambda) \tag{4.4}$$

Where $\vec{r}_{\rm o}$ is the vector pointing to the actual event vertex position from the center of the detector, and $\hat{\nu}$ is the unit vector pointing outward from the surface of the photosensitive area pointed by $\vec{r}_i$. The attenuation length of the liquids, λ, which is assumed to be 1.2×10^4 mm, is accounted for in this calculation. For a given actual input vertex position, $\vec{r}_{\rm o}$, we obtain the average output vertex position $\vec{r}_{\rm vtx}$ using Monte Carlo programs. The positions are then compared to obtain correction factors for the radius components ρ and z components as a function of $\vec{r}_{\rm vtx}$. The calculated correction factors are shown on the left side of Figure 4.11. The results of the reconstructed vertex are shown on the right side of Figure 4.11. Naïve method refers to the weighting method using Eq. 4.3 with a fixed correction factor of 1.5, which is a correction factor for the spherical detector, and the improved method refers to the weighting method corrected with Eq. 4.4.

The performance of the vertex reconstruction was validated with 3 calibration source datasets: ^{137}Cs, ^{68}Ge, and ^{60}Co. Each radioactive source is deployed in the target along the cylinder axis from z = 1,200 $\sim$ 1,200 mm at 300 mm intervals. Figure 4.12 shows that the vertex resolution is about 20 cm at 1 MeV and improves at higher energies. X-axis in Figure 4.12 is the difference of reconstructed z-position and source z-position ($z_{\rm rec}$ $z_{\rm src}$).

Figure 4.13 shows a reasonable agreement between the reconstructed and actual source locations. The difference is as large as $\sim$7% for ^{137}Cs and less than

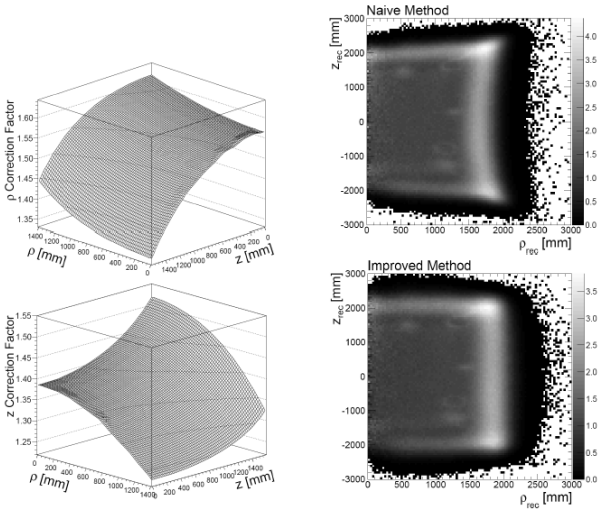

Figure 4.11: The left side is the correction factors to ρ and z calculated with a Monte Carlo program. The right side shows the reconstructed event vertex density distributions of background events in ρ and z values using the naïve and improved methods. The external γ background events highlight the reconstructed outer boundary of the γ-catcher. The naïve method has position-dependent biases [68].

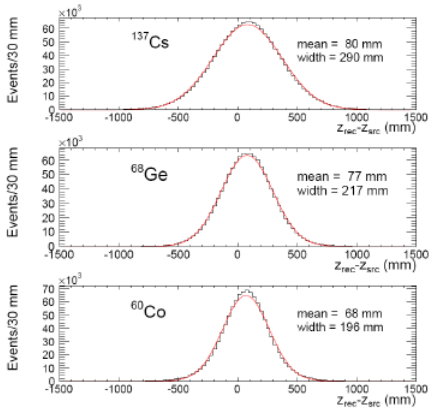

Figure 4.12: The residual of the reconstructed and source z-positions, $z_{rec}z_{src}$, for ^{137}Cs, ^{60}Co, and ^{68}Gesource samples for ND for all source z-positions. The distribution's mean and width of the Gaussian fit (red line) are also shown.

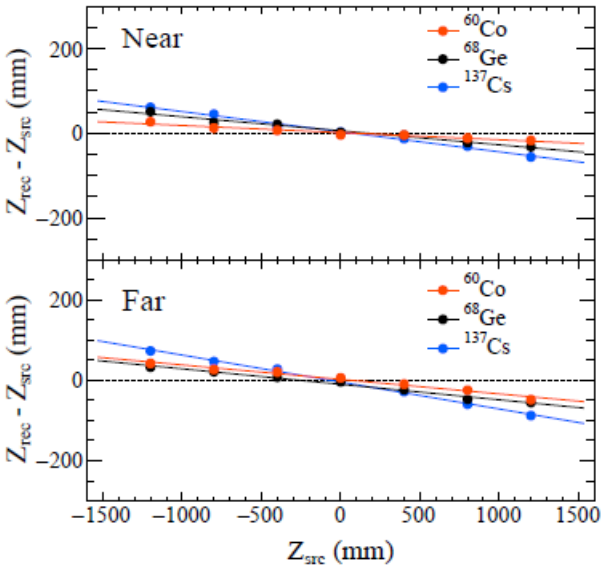

Figure 4.13: Difference between reconstructed vertices (Z_{rec}) and actual positions (Z_{src}) of ^{137}Cs, ^{68}Ge, and ^{60}Co sources. The reconstructed vertices show systematic deviations from the true positions at the source locations away from the center. The systematic shifts reduce as the source of energy increases.

$\sim$5% for the other two sources with γ-ray energies larger than 1 MeV. However, this bias is not a problem because the requirement of a delayed signal naturally picks the target event without any information about the event vertices.

Chapter 5

Energy Calibration

Because the measurement of θ_{13} mainly depends on the systematic uncertainties in the relative parameters between FD and ND, it is important to investigate the detector performance in more detail. There are two main motivations for having an energy calibration system. First, in the energy range of 1∼10 MeV, the features of the event depend on the location of the event vertex as the scintillation lights pass through the liquid scintillator, acrylic vessel, and buffer oil. The vertex position-dependence of energy measurements can be understood by placing radioactive sources at various points inside a liquid scintillator and measuring the energy deposits. Detailed optical parameters of the liquid scintillator, acrylic vessel, and stainless steel tank of both detectors can be obtained and compared. Second, the scintillation and optical properties of liquid scintillators are changed during the long data-taking period. Therefore, it is important to monitor the detector response during the experiment. Additionally, the day and night oscillation from the energy measurements due to temperature and other environmental factors inside and outside the detector also require continuous monitoring to ensure the regular calibration source data. The delayed signal is also used in daily monitoring data and obtains the daily charge correction factor.

5.1 Radioactive Sources

To calibrate the detector response for the IBD of reactor antineutrinos, several radioactive sources are used, and these have a μCi level or lower activities: ^{54}Mn, ^{137}Cs, ^{68}Ge, ^{65}Zn, ^{60}Co, and ^{252}Cf . The characteristics of the radioactive sources are summarized in Table 5.1. ^{252}Cf is important because it is the neutron source for this study. The ^{252}Cf source can help verify the neutron capture on gadolinium in the target region. The size of the radioactive source is limited by the attenuation length (0.511 MeV γ ray) for the positron source. The attenuation length

of the 0.511 MeV γs in the LS is approximately 10 cm. Thus, to minimize the amount of scintillation light getting scattered by the source itself, the overall size of the radioactive source should be several times smaller than the attenuation length. The overall size of the source is 2 cm $\times$ 3 cm. When deploying points, the source is enclosed in an acrylic container. The material of the acrylic container should be congruous with the scintillator materials, and polytetrafluoroethylene (PTFE) could be one of the best candidate materials. Figure 5.1 shows the spectra of source data.

type	sources	energy (keV)	calibration
e^+	^{68}Ge	511(2)	position E threshold
γ	^{137}Cs	662	gamma
	^{54}Mn	821	gamma
	^{65}Zn	1116	gamma
	^{60}Co	1173+1333	multiple gamma
neutron	^{252}Cf	neutron + $\sim$10 MeV	neutron efficiency

Table 5.1: A list of radioactive sources for calibration.

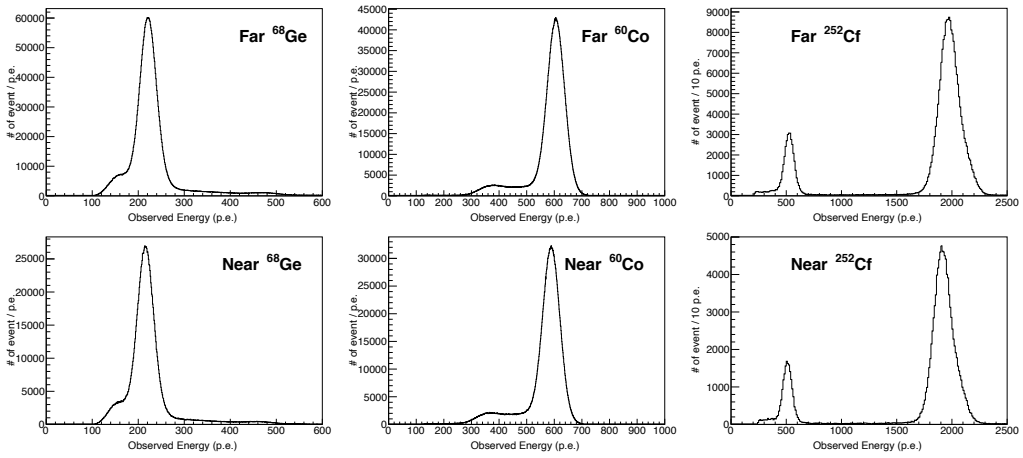

Figure 5.1: Spectra of source data. The top side is FD, and the bottom side is ND.

5.2 Source Deployment System

The main goal of using radioactive sources for calibration is to measure the energy scale, resolution, and vertex position dependence of energy measurement. Therefore, we need to deploy the source at the desired point accurately. To achieve this, we developed a 1D and 3D source deploying system operated with personal computer software as micro control unit (MCU). The 1D system is composed of a stepping motor-driven pulley with a polyethylene wire. The acrylic container connected the wire with a weighting teflon rod to resist the buoyant force of LS. The system has a z-position accuracy of a few mm, which is much smaller than the resolution (a few cm) of the vertex position of the detector. We made two 1D source deploying systems for each detector. One is for the target, and the other is for the γ-catcher region. At the target region, the z-axis is exactly at the center of the target vessel and the side of the detector for the γ-catcher. Figure 5.2 shows the design of the 1D driving system. Using the 3D deploying system, the radioactive source can be located in the target region only. This system is consists of four rods that can connect with each other, and there is a robot arm at the end of these rods. The robot arm can be folded and has three points for locating the source container. Moreover, the robot arm can be rotated, allowing it to locate the source at the center, the three-side position, and all the ϕ angles. Figure 5.3 shows the design of the 3D calibration system, and Figure 5.4 shows the 1D/3D calibration system installed at the detector.

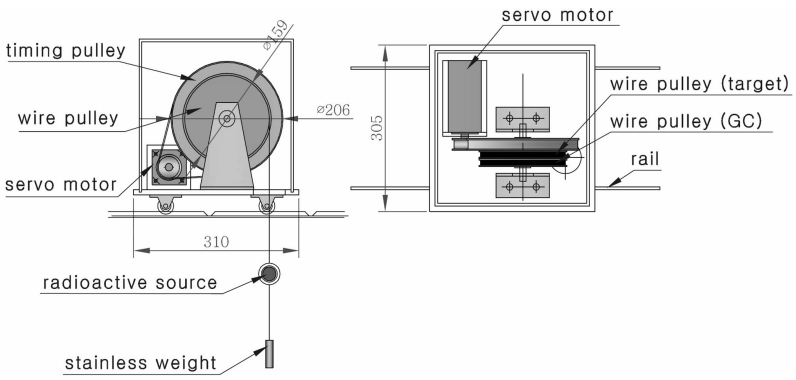

Figure 5.2: Simple drawing of 1D source deploying system.

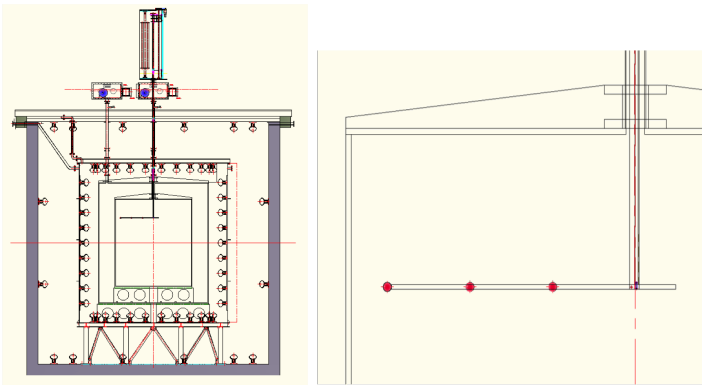

Figure 5.3: Simple drawing of 3D calibration system. The plot on the left shows a sectional view of a 3D calibration system mounted on the detector. The red dot in the right plot corresponds to the position of the calibration source in the robot arm.

Figure 5.4: Picture of the installed 3D system.

5.3 Energy Determination

To build the energy conversion function, 6 radioactive sources (^{54}Mn, ^{68}Ge, ^{65}Zn, ^{60}Co, AmBe, NiCf) and n-H IBD events are adapted for reference points corresponding to true energies. Through the conversion function, we can identify

the number of photoelectrons (npe) as energy (MeV). Each reference point is converted npe/MeV through the following equation.

$$\text{npe/MeV} = \frac{\text{observed charge (npe)} \cdot \text{C}_{\text{Uniform/Center}} \cdot \text{C}_{\text{e}^+/\gamma}}{\text{energy of radioactive source (MeV)}} \tag{5.1}$$

, where the measured charge is the peak value of radioactive source data at the center of each detector (Target, γ-catcher of FD and ND). There is a slight difference between the source data and the positron signal from IBD; therefore, correction is needed. The correction factor, $C_{\text{Uniform/Center}}$, is the difference between the calibration source position and the whole region in each detector. Source data is taken at a specific location (the center coordinates of Target is $x = 0$ mm, $y = 0$ mm, $z = 0$ mm, and γ-catcher is $x = 0$ mm, $y = 1650$ mm, $z = 0$ mm) and IBD events are distributed in all region of the detector. The measured charge depends on the position, and this difference should be corrected. This factor is obtained using the delayed signal of IBD data and summarized in Table 5.2.

γ-catcher	FD	ND
Center-to-Uniform correction factor	1.0106 ± 0.0002	1.0082 ± 0.0013

Table 5.2: γ-catcher center-to-Uniform correction factor, $C_{\text{Uniform/Center}}$, at the FD and ND.

The $C_{e^+/\gamma}$ is a correction factor for the conversion γ-ray to positron. It is derived by comparing positron MC and source MC and summarized in Table 5.3. Source MC simulates the number and energy of γ from a radioactive source, and positron MC simulates the total energy of radioactive as a single positron like IBD signal. The light emission of the positron in LS is different from γ from a radioactive source. It is also influenced by the number of γ, therefore, this difference should be corrected. The raw npe at the FD and ND are summarized in Table 5.4. The corrected npe at the FD and ND of Equation 5.1 are summarized in Table 5.5.

Source	FD	ND
^{54}Mn	0.967 ± 0.005	0.975 ± 0.005
^{68}Ge	1.033 ± 0.007	1.033 ± 0.008
^{65}Zn	0.968 ± 0.005	0.975 ± 0.005
(n-H)	0.977 ± 0.003	0.989 ± 0.001
^{60}Co	1.041 ± 0.003	1.041 ± 0.002
Ambe (n-C)	0.997 ± 0.006	0.996 ± 0.003
NiCf	1.002 ± 0.001	1.001± 0.001

Table 5.3: Correction factor for γ-to-e$^+$, $C_{e^+/\gamma}$, in the γ-catcher of FD and ND.

Source	raw npe (FD)	raw npe (ND)
^{54}Mn	200.008 ± 2.902	192.117 ± 2.439
^{68}Ge	232.02 ± 4.537	223.473 ± 3.761
^{65}Zn	273.055 ± 3.364	261.383 ± 4.395
(n-H)	578.891 ± 0.314	565.064 ± 558.722
^{60}Co	619.931 ± 10.739	597.701 ± 10.046
AmBe (n-C)	1320.77 ± 13.003	1313.83 ± 13.476
NiCf	2277.95 ± 15.999	2248.36 ± 19.945

Table 5.4: Raw charge of calibration sources data in the γ-catcher of FD and ND.

The LS has a quenching effect, especially at low energy. Therefore, the npe/MeV is not linear with energy, as shown in Figure 5.5. The error bar is large because the amount of data acquired from radioactive sources is small. Equation 5.2 is chosen as the model of energy conversion function, which is considered non-linearity.

$$\text{npe / MeV} = P_0 - \frac{P_1}{1 - \exp(-P_2 \cdot \text{MeV} - P_3)} \tag{5.2}$$

, where P_0, P_1, P_2, and P_3 are fitting parameters. The fitting results are shown in Figure 5.5 and Table 5.6. Using the obtained parameters and Equation 5.2, the observed charge in the detector can be converted to MeV.

Source	FD	ND
^{54}Mn	237.502 ± 3.47486	227.491 ± 2.9797
^{68}Ge	240.168 ± 5.04467	228.784 ± 4.2938
^{65}Zn	242.528 ± 3.02219	231.509 ± 3.96328
(n-H)	251.071 ± 0.888403	246.569 ± 0.283518
^{60}Co	258.246 ± 4.54655	246.341 ± 4.16627
AmBe (n-C)	265.59 ± 3.03576	261.019 ± 2.76824
NiCf	268.603 ± 1.94596	261.718 ± 2.33272

Table 5.5: Corrected values (npe/MeV) of each calibration source data in the γ-catcher FD and ND. The uncertainty of each source comes from statistics and fittings of the peak value.

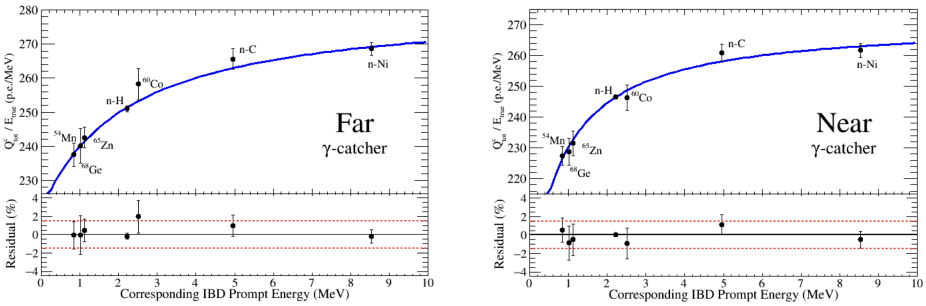

Figure 5.5: Energy conversion function for data in the γ-catcher FD and ND. The curve is the fitting function, and each point is the measurement result of npe/MeV from source data. There is a quenching effect, and the fitting function is considered for saturation at high energy.

^{12}B and ^{12}N isotope are produced by muon and undergo β-decay, and the energy spectrum is distributed in 0∼18 MeV. These backgrounds made only prompt signals; therefore, they do not contribute to the IBD signal. In Figure 5.6, the energy spectrum of ^{12}B and ^{12}N was compared with MC to check the energy conversion function. This result indicates that the energy conversion function works well in the energy window of the electron antineutrinos. In addition, it shows how RENO MC is well-tuned and works fine.

Parameter	FD	ND
P_0	281.651 ± 4.554	271.057 ± 2.414
P_1	0.022435 ± 0.007218	0.019681 ± 0.002941
P_2	0.000167 ± 0.000073	0.000262 ± 0.000048
P_3	0.000370 ± 0.000125	0.000220 ± 0.000053

Table 5.6: The fitting results of energy conversion function in the γ-catcher ND and FD.

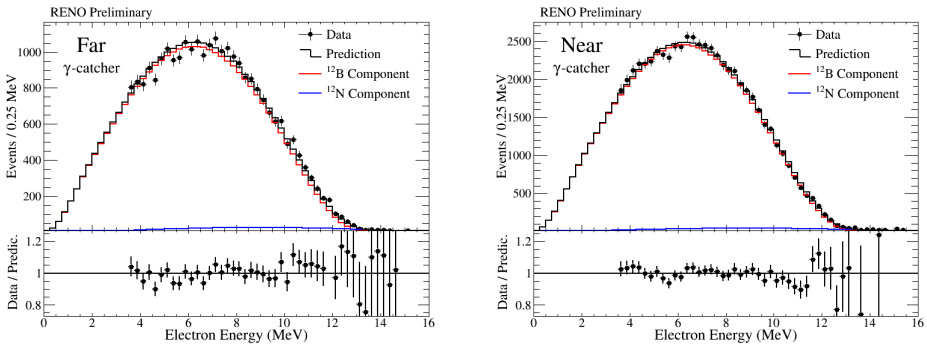

Figure 5.6: Energy spectrum of ^{12}B and ^{12}N at the FD and ND. The spectrum of the data agrees well with MC for the γ-catcher of FD and ND. The fraction of ^{12}N is 2.89% (2.80%) in FD (ND).

The conversion function for the target region was also developed in the same way for the γ-catcher. The fitting results of target region are shown in Fig. 5.7 and Table 5.7.

Parameter	far	near
P_0	275.9 ± 1.0	270.1 ± 1.3
P_1	0.0170 ± 0.0015	0.0170 ± 0.0025
P_2	0.000123 ± 0.000012	0.000116 ± 0.000012
P_3	0.000174 ± 0.000018	0.000179 ± 0.000030

Table 5.7: The fitting results of energy conversion function in the target region of FD and ND.

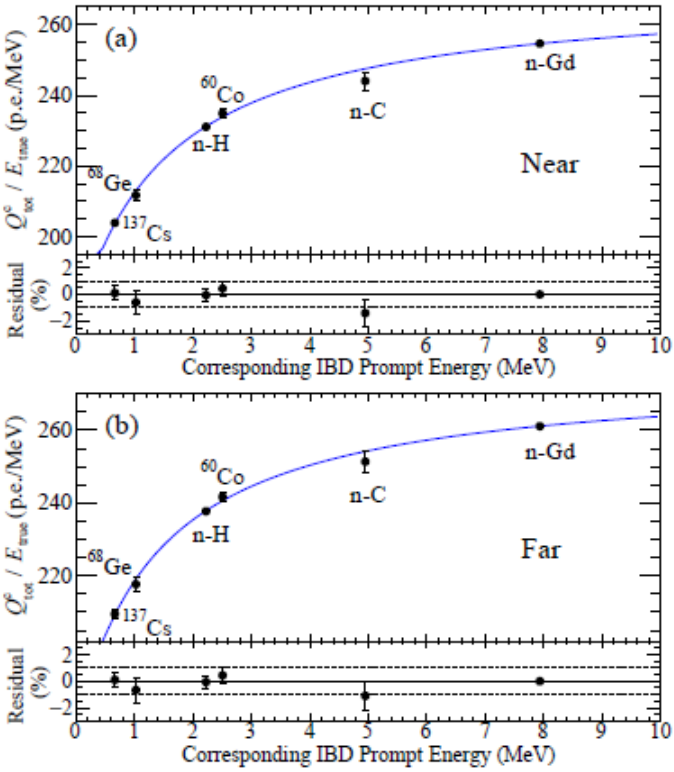

Figure 5.7: Energy conversion function for data in the target of FD and ND. The curve is the fit results to the data points The nC sample is obtained from the ^{210}Po^{9}Be source and the n-H sample from the ^{252}Cf source. The lower panels show fractional residuals of all calibration data points from the best fit. There is also a quenching effect same as the γ-catcher.

Chapter 6

Event Selection

The reactor electron antineutrinos are detected via the IBD reaction which produces a pair of prompt and delayed signals. The n-H IBD candidate sample is made by coincidence requirements between a prompt-like event with an energy of 1.2 to 12 MeV and a delayed-like event with an energy near 2.2 MeV. Because of high ambient γ-rays against the delayed signal and a large accidental background from a rather large coincident time, the n-H IBD selection criteria need to be carefully optimized to extract the IBD signal. This Chapter describes the applied selection criteria to remove backgrounds correlated or uncorrelated between the prompt and delayed events.

6.1 Data Sample

The RENO experiment has been continuing data-taking since August 11, 2011. This analysis is obtained by using ∼2900 days of data through June 05, 2019. The data with a satisfactory run conditions were used after checking operational parameters. The data sample consists of two parts, Set A and Set B, according to ^{252}Cf contamination. The contamination was made in the Gd-LS by a tiny amount of ^{252}Cf that was accidentally smeared into both detectors during calibrations. The reason is that the calibration source container did not perfectly seal due to a loose "O" ring. When the ^{252}Cf source container was submerged in the target during calibrations, Gd-LS permeated into the acrylic container, and a tiny amount of dissolved ^{252}Cf leaked into Gd-LS. Set A is without the contamination, and set B is with the contamination. Roughly a year of ND data is not used because of electronic noise introduced by an uninterruptible power supply (UPS) which was installed on January 22, 2013. Table 6.1 describes data sets A and B as well as the unused near data sample. Figure 6.1 shows the daily data-collection efficiency for both detectors, during the period of the used data sample.

Detector	Data Set	Date	Time (days)
Far	Set A	11^{th} Aug, 2011 $\sim$ 28^{th} Sep, 2012	384.473
	Set B	28^{th} Sep, 2012 $\sim$ 4^{th} Jun, 2019	2268.824
Near	Set A	19^{th} Aug, 2011 $\sim$ 27^{th} Oct, 2012	379.663
	Set B	27^{th} Oct, 2012 $\sim$ 5^{th} Sep, 2019	1879.625
Near	UPS on (excluded)	21^{th} Jan, 2013 $\sim$ 18^{th} Oct, 2013 14^{th} Nov, 2013 $\sim$ 31^{th} Dec, 2013	267.80

Table 6.1: Two sets of data samples at FD and ND for $\sim$2900 days of data.

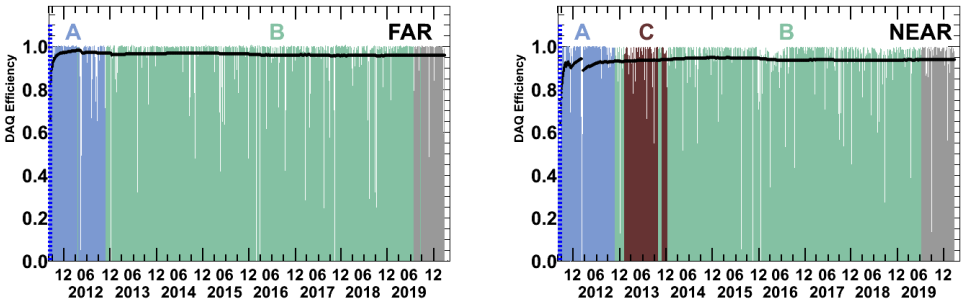

Figure 6.1: Daily data-collection efficiencies for FD (left) and ND (right). The black curves represent the efficiencies. A (B) represents the data Set A (B) without (with) the ^{252}Cf contamination, and C indicates the unused data set due to the electronic noise from the UPS at ND.

6.2 Removal of γ-ray from Environmental Radioactivity

The main background of the prompt and delayed candidate is contributed by ambient γ-rays from natural radioactivity, flashing lights from PMTs, and electronic noise. The ambient γ-rays below $\sim$3.5 MeV emanate from PMT glasses, LS, mineral oil, detector vessels and surrounding rocks. The concentration of radioisotopes in the ID materials is measured using ICP-MS and HPGe detectors. The most single event rates contributed by the radioactivity of each detector subsystem are estimated with the radioactive concentration and detector acceptance from a MC simulation. Table 6.2 lists the radioactive concentration and the estimated single event rates. Figure 6.2 shows the expected energy spectra of γ-rays

emanating from radioactive materials in the detector.

	^{40}K (ppt)	^{232}Th (ppt)	^{238}U (ppt)	Single Event Rate (Hz)
Rock	4.33(ppm)	7.58(ppm)	2.32(ppm)	9.2
Target LS	< 0.32	17.7	13.9	5.6
Target Acrylic	8	206.8	167.5	0.95
γ-catcher LS	< 0.32	17.7	13.9	< 8.4
γ-catcher acrylic	8	206.8	167.5	0.87
Buffer Oil	10	19.7	5.0	1.07
Buffer Vessel	60	900	900	0.33
PMT	10.8	125.9	50.3	8.19
Total				< 34.6

Table 6.2: Ambient γ-rays come from in surrounding rock and the main components of the identical RENO detectors

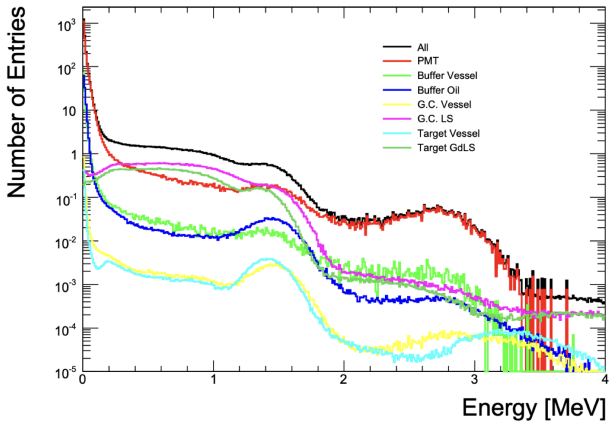

Figure 6.2: Expected energy spectra of γ-rays emanating from radioactive materials in the detector.

The backgrounds of ambient γ-rays, PMT flashing and electronic noise can be effectively identified by a localized charge measurement. Such a localized charge pattern is sensitive to the total PMT charge (Q_{tot}) and the maximum charge (Q_{max}) of any single ID PMT. These backgrounds are significantly removed by requiring a small value of Q_{max}/Q_{tot} for uniformly distributed charges over PMTs. An efficient requirement is applied to reduce single event rates by rejecting prompt candidates with $Q_{max}/Q_{tot} > 0.07$ and delayed candidates with $Q_{max}/Q_{tot} >$

0.06. The efficiency of the $Q_{max}/Q_{tot} > 0.07$ (0.06) requirement is (97.45 ± 0.07) [(86.58 ± 0.09)]% at both detectors.

6.3 Removal of Cosmic-Ray Background

Cosmic muons entering the detector are easily identified and removed because they leave a trace by Cherenkov radiation in the veto layer. A cosmic muon-induced neutron in the detector or the surrounding rock can mimic the IBD delayed signal. A veto time of 1 ms is imposed to remove the cosmic-induced neutron background. A high-energy muon can make various radioactive isotopes. Among them, ^{9}Li and ^{8}He, in particular, release an electron and a neutron via subsequent decays and mimic an IBD pair signal. The prompt and delayed events coming from the cosmogenic isotopes of ^{9}Li and ^{8}He are correlated to the preceding muon event. In order to remove those ^{9}Li and ^{8}He background pairs, an IBD candidate is rejected within a few hundred milliseconds after its preceding high energetic muon. The veto time is differently required depending on the preceding muon energy to minimize the signal loss. The muon rate rapidly decreases as the muon energy increases, as shown in Figure 6.3. The muon visible energy is limited in the detector size and thus a sharp fall-off is seen in the energy of ∼1.7 GeV. The cosmic muon veto criteria are imposed differently according to the five energy groups of 1, 2, A, B, and C because the ^{9}Li and ^{8}He production rate is proportional to the muon energy, as shown in Figure 6.4. The muon rates for those energy ranges are given in Table 6.3, and different veto time windows are determined according to the muon rates.

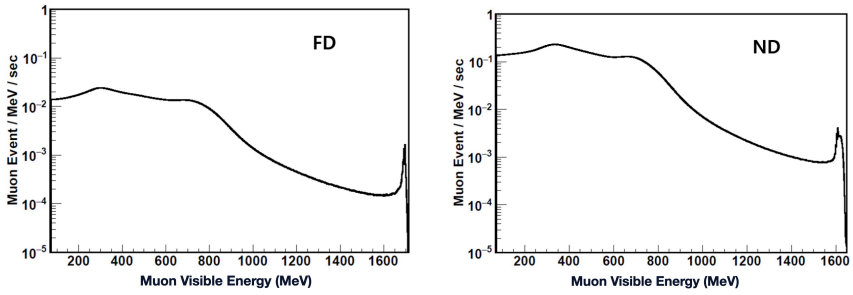

Figure 6.3: Muon visible energy spectra observed at FD (left) and ND (right). The maximum visible energy near 1.7 GeV is attributed to the dynamic range of the RENO electronics and the detector size.

Muon	FD		ND	
Type	Energy	Rate (Hz)	Energy	Rate (Hz)
1	$0.07 \sim 1.0$ GeV	12.854	$0.07 \sim 1.4$ GeV	117.193
2	$20 \sim 70$ MeV	0.258	$20 \sim 70$ MeV	0.759
A	> 1.5 GeV	0.047	> 1.6 GeV	0.107
B	$1.2 \sim 1.5$ GeV	0.081	$1.5 \sim 1.6$ GeV	0.081
C	$1.4 \sim 1.5$ GeV	0.091	$1.0 \sim 1.2$ GeV	0.157

Table 6.3: Muon rate observed at different visible energies. The muon at ND is higher than at FD due to a shallow overburden. Note that ND is located under a 70 m high mountain and FD is under a 200 m high mountain.

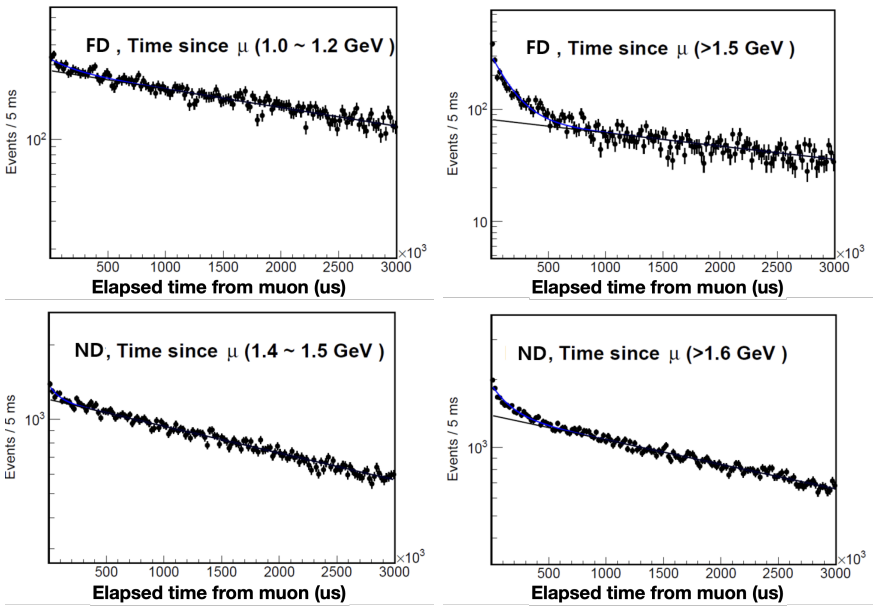

Figure 6.4: Elapsed time from the preceding muon. A fit was made with two exponential functions. The shorter decay time component corresponds to the ^{9}Li/^{8}He background and the longer decay time to the IBD signals. Because of the high muon rate, it is difficult to see the ^{9}Li/^{8}He production below 1.0 GeV (1.4 GeV) at FD [ND].

The muon veto time windows below are determined by taking into account the signal loss and the fraction of removed ^{9}Li/^{8}He background. The total loss of IBD signal by the muon veto criteria is (11.49) [(21.55)]% for FD [ND].

The optimized requirements are as follows:

- Muon 1 (FD : 0.07 $\sim$ 1.0 GeV, ND : 0.07 $\sim$ 1.4 GeV) : Veto all events within a 1 ms window following Muon 1.
- Muon 2 (FD, ND: 20 $\sim$ 70 MeV, number of hits in the outer detector $>$ 50): Veto all events within a 1 ms window following Muon 2.
- FD Muon A ($>$ 1.5 GeV): Veto all events within a 700 ms window following muon A at FD.
- FD Muon B (1.2 $\sim$ 1.5 GeV): Veto all events within a 500 ms window following muon B at FD.
- FD Muon C (1.0 $\sim$ 1.2 GeV): Veto all events within a 200 ms window following muon C at FD.
- ND Muon A ($>$ 1.6 GeV): Veto all events within a 700 ms window following muon A at ND.
- ND Muon B (1.5 $\sim$ 1.6 GeV): Veto all events within a 400 ms window following muon B at ND.
- ND Muon C (1.4 $\sim$ 1.5 GeV): Veto all events within a 200 ms window following muon C at ND.

The fraction of IBD signal loss due to the muon timing veto requirements at FD [ND] is (11.27) [(21.56)]% for Set A and (11.52) [(21.54)]% for Set B.

6.4 IBD Pair Requirements

After removing cosmic muon-induced background events, prompt or delayed candidates from the IBD reaction are selected by appropriate energy requirements. A prompt signal comes from a positron and its annihilation and releases visible energy of more than 1.02 MeV. A delayed signal comes from a γ-ray produced by a neutron capture on H. IBD candidate pairs are selected by time and spatial coincidence between the prompt and delayed events.

Prompt Energy Requirement

After the muon time veto requirement, a prompt candidate event is selected by requirement of the prompt energy (E_{prompt}) between 1.2 and 12 MeV.

$$1.2 \text{ MeV} < E_{prompt} < 12.0 \text{ MeV}$$

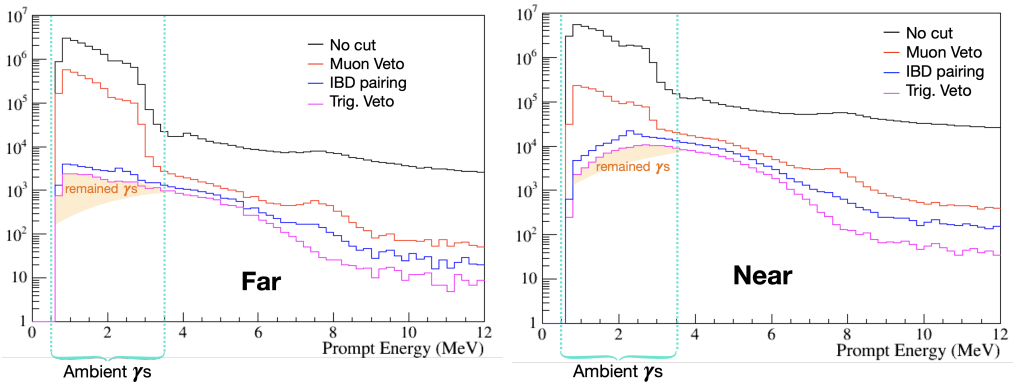

Figure 6.5: Energy spectra of prompt event candidates after applying the muon time veto requirement.

The energy distributions of the prompt candidate events before the energy requirement are shown in Figure 6.5 and show a large background coming from radioactivity below ∼3.5 MeV. The events with $E_{prompt} < 1.2$ MeV dose not include IBD events occurring in, also near the acrylic vessel of ID that deposit positron kinetic energy in the acrylic of ID wall without emitting scintillation lights. These reconstructed events have visible energy near the 1.02 MeV positron energy. The IBD signal loss by the $E_{prompt} > 1.2$ MeV requirement is about 2% in both detectors. The prompt events emerging around the acrylic of the target could lose some of their energy in the non-scintillating acrylic region and conduct with a slight change of its prompt energies. The energy misestimation affects both FD and ND as identical and has a negligible effect on the results.

Delayed Energy Requirement

A delayed energy ($E_{delayed}$) of 2.2 MeV is emitted by a γ-ray from neutron capture on H. The delayed signal suffers from a large γ-ray background coming from natural radioactivity below ∼3.5 MeV. Therefore, the high purity of n-H delayed events can be selected by requiring their prompt energy above 3.5 MeV, as shown in Figure 6.6. Based on the energy distribution clearly peaking at 2.2 MeV, a delayed energy requirement with a 2σ energy range is imposed to select the n-H signal against the large radioactivity background where σ represents the Gaussian energy resolution of roughly 0.25 MeV.

$$2.2 - 2\sigma < E_{delayed} < 2.2 + 2\sigma \text{ MeV}$$

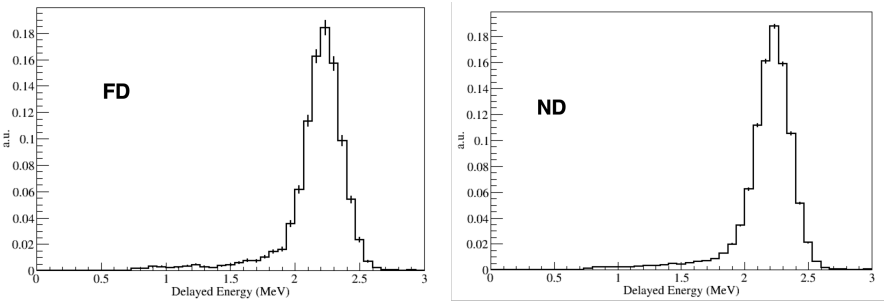

Figure 6.6: Energy distributions of pure delayed signal events which are selected by requiring a paired prompt event with an energy > 3.5 MeV. The spectra peak at 2.2 MeV agreement with a γ-ray energy coming from neutron capture on H.

Time Coincidence Requirement

A neutron released from the IBD reaction carries relatively low energies below 30 keV. The neutron keeps losing the energy by multiple scatterings with protons and becomes thermalized within $\sim$2 μs to be captured on H. The expected capture time is roughly 200 μs. The measured capture time shown in Figure 6.7 is consistent with the expectation. A large time difference (ΔT) between prompt and delayed candidates may come from accidental pairs. Therefore, a time coincidence requirement below is applied to reduce the accidental background. The signal loss due to this requirement is 86.86 $\pm$ 0.125% for Set A and 87.84 $\pm$ 0.104% for Set B.

$$2\ \mu\text{sec} < \Delta\text{T} < 400\ \mu\text{sec}.$$

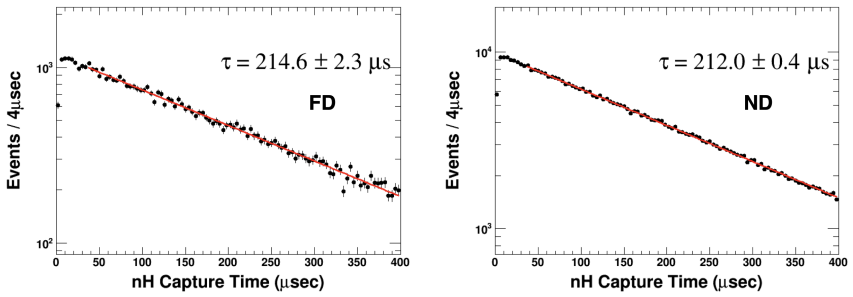

Figure 6.7: Capture time distributions of pure delayed signal events which are selected by requiring a paired prompt event with an energy > 3.5 MeV. The fitted capture time is approximately 200 μs, consistent with expectation.

Spatial Coincidence Requirement

A neutron from the IBD reaction is not displaced from its production point due to its minimal kinetic energy below 30 keV. Figure 6.8 shows distributions of distance (ΔR) between prompt and delayed candidates. A good spatial correlation is shown in the distribution of ND while a large accidental background is evident for FD. A spatial correlation requirement of $\Delta R < 450$ mm is applied to reduce the accidental background pairs. Thus, the following criteria were determined considering the fraction of the IBD signal and the accidental background.

$$\Delta R < 450 \text{ mm}$$

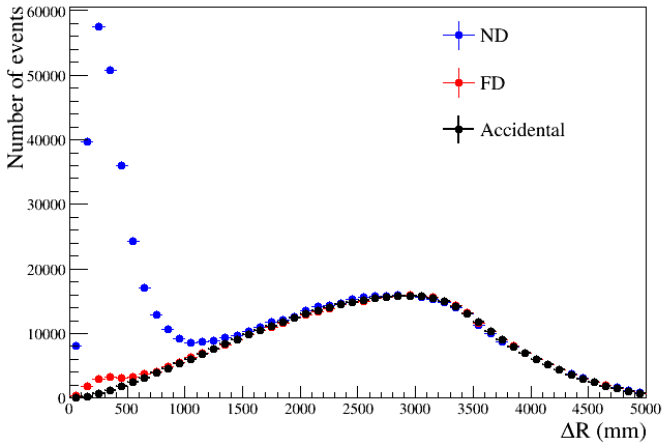

Figure 6.8: Distributions of ΔR between prompt and delayed candidates at FD and ND. The black distribution represents a spatial correlation of accidental pairs with a large ΔR. A clear spatial correlation is seen from ND ΔR distribution (blue) while the accidental contribution to FD distribution (red) is rather large in the $\Delta R < 450$ mm due to γ-rays from radioactivity.

6.5 Multiplicity Timing Veto Requirement on Trigger and Event

The RENO trigger is formed if there is a signal above a threshold in the inner (ID) and outer (OD) detectors. An IBD pair candidate accompanied with a trigger in a short time interval is most likely a background because the chances are so low for a true IBD signal. The veto timing criteria are determined based on the trigger and background rates. Table 6.4 shows average trigger rates observed for data

sets A and B at FD and ND. Several multiplicity criteria based on trigger and event information are adapted to remove events of a single fast neutron, multiple neutrons, and the ^{252}Cf contamination background.

Detector	Period	Rate [Hz]		
		ID	OD	ID & OD
Far	Set A	77.01	38.21	23.14
	Set B	71.69	35.87	22.99
Near	Set A	60.60	320.54	208.62
	Set B	58.91	320.48	206.67

Table 6.4: trigger rates at FD and ND.

Any Trigger Requirement

The probability of a trigger or an event occurring close to a true IBD signal is quite low because of the rare reactor antineutrino signals. Therefore, IBD candidate pairs are rejected if they are accompanied by any preceding ID or OD trigger within a few hundred μs window before them. The timing correlation between background pairs and any triggers is evident for $\sim$600 μs, clearly seen in Figure 6.9 and 6.10. Figure 6.11 shows the background pairs are more closely associated with an OD trigger in time. This is likely due to cosmic muon-induced spallation products including neutrons. The backgrounds pairs are rejected if any trigger is accompanied within certain time windows (see the listed timing veto criteria below). Figure 6.7 shows the prompt energy distribution of those rejected events by the trigger veto criteria. The neutron backgrounds captured on Gd or H are clearly seen and a lot of multiple neutron captures are removed. The IBD signal loss at FD [ND] by the any trigger requirement is (3.7) [(13.2)]% for Set A and (5.7) [(20.8)]% for Set B.

- Data Set A: 300 μsec before prompt signal

- Data Set B: 500 μsec before prompt signal

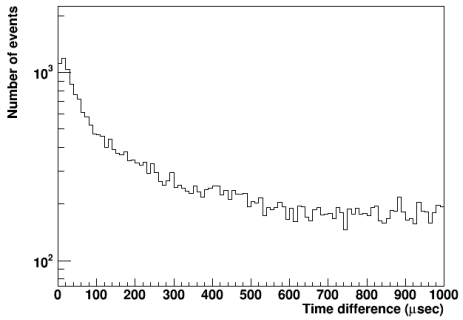

Figure 6.9: Time difference distribution between an ID trigger and a prompt candidate. A clear time correlation within ∼600 μs is seen.

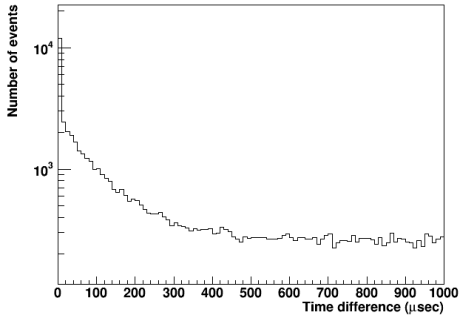

Figure 6.10: Time difference distribution between an ID or OD trigger and a prompt candidate. A clear time correlation within ∼600 μs is seen.

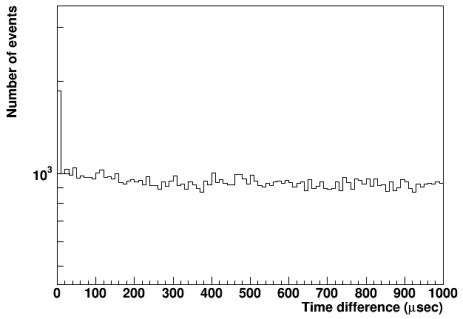

Figure 6.11: Time difference distribution between an OD trigger and a prompt candidate. A shorter time correlation is seen for the OD trigger association.

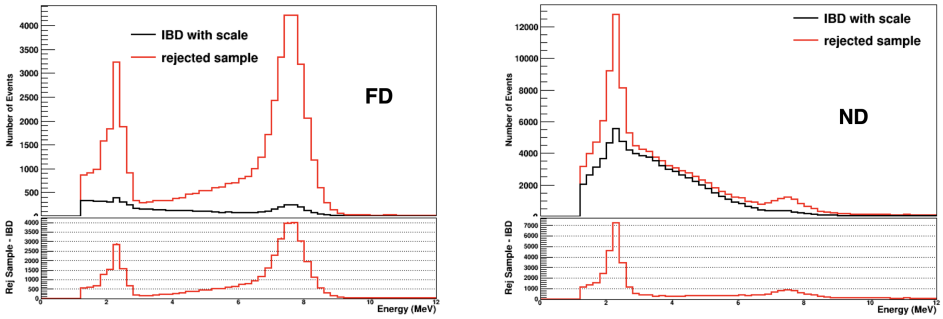

Figure 6.12: Prompt energy spectra of background pairs rejected by the any-trigger requirement at FD and ND. The red histograms represent the prompt events rejected by the requirement. The black histograms represent the estimated IBD signal loss. The bottom panels show the prompt energy spectra of rejected backgrounds, clearly showing neutron captures on Gd and H.

Pair Multiplicity Requirement

If multiple neutrons come in at almost the same time, two 2.2 MeV delayed signals by neutron capture can be paired. They interact with the proton in the detector and lose energy before the neutrons are captured. Then there must be generated a signal in the ID. These backgrounds can be removed using only ID or ID & OD trigger information. The requirement range is determined based on the two triggers' time distribution, as shown in Figure 6.9 and 6.10.

- Data Set A: 300 $\sim$ 600 μsec between any of two pair candidates

- Data Set B: 500 $\sim$ 600 μsec between any of two pair candidates

Figure 6.13 shows the prompt energy distributions of IBD candidate pairs rejected by the pair multiplicity requirement. The IBD signal loss at FD [ND]is (2.5) [(4.2)]% for Set A and (0.8) [(1.3)]% for Set B.

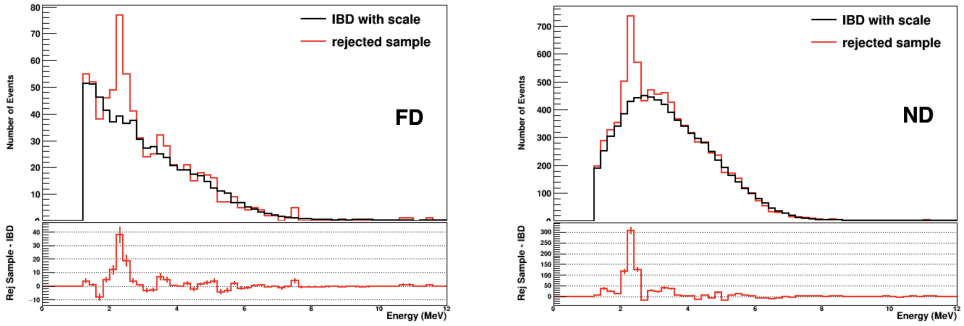

Figure 6.13: Prompt energy distributions of IBD candidate pairs rejected by the pair multiplicity requirement at FD and ND. The red histograms represent the prompt events rejected by the requirement. The black histograms represent the estimated IBD signal loss. The bottom panels show the prompt energy spectra of rejected backgrounds, clearly showing neutron captures on H.

ID Trigger Requirement

Fast neutrons entering the detector interact with protons in LS several times, finally lose most of energy and are captured by Gd or H. They mimic IBD pair signals and can be removed if an ID trigger occurs within 800 μs after an IBD pair. Figure 6.14 shows the elapsed time distribution of ID triggers after a prompt signal of an IBD and a clear time correlation of $\sim$1 ms between them. Figure 6.15 shows the prompt energy distributions of pairs rejected by the ID trigger requirement, consistent with the fast neutron spectrum. The IBD signal loss at FD [ND] is (5.4) [(4.4)]% for Set A and (4.9) [(3.7)]% for Set B.

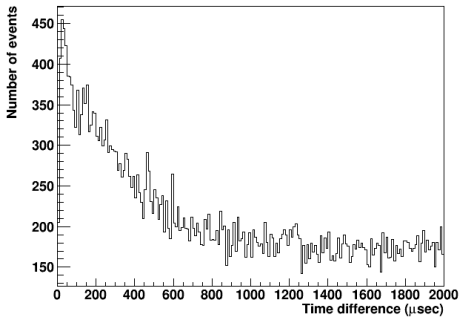

Figure 6.14: Time difference distribution of an ID trigger after a prompt candidate. A time correlation of $\sim$1 ms is seen.

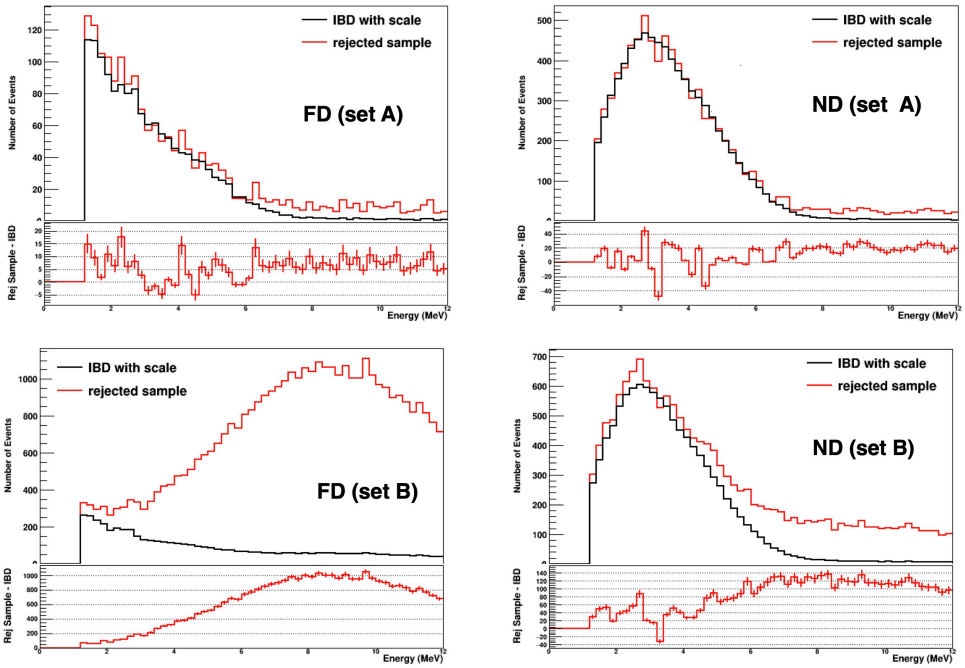

Figure 6.15: Prompt energy distributions of pairs rejected by the ID trigger requirement. The bottom panels show the prompt energy spectra of rejected background pairs, consistent with that of the expected fast neutrons, and the data set B spectrum have consistent with the combination of ^{252}Cf component and fast neutron.

ID and OD Trigger Requirement

Multiple neutrons can be produced by a high energetic cosmic muon in the detector. One of the neutrons interacts with protons in ID and is captured on H to mimic an IBD signal while the other neutron escapes from the ID and leaves signals in both ID and OD. Such IBD background pairs can be removed if an ID and OD trigger occur within 100 or 200 μs after an IBD pair. Figure 6.16 shows the prompt energy distributions of pairs rejected by the ID and OD trigger requirements, consistent with the fast neutron spectrum. The IBD signal loss at FD [ND] is (0.05) [(0.95)]% for Set A and (0.28) [(2.69)]% for Set B.

- Data Set A: ~100 μsec after the prompt signal
- Data Set B: ~200 μsec after the prompt signal

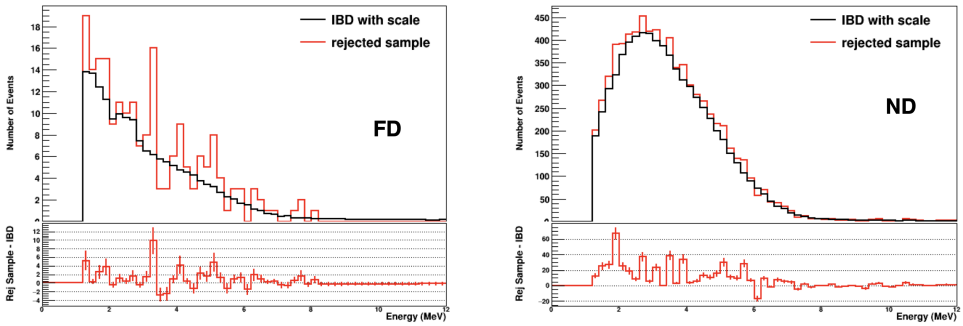

Figure 6.16: Prompt energy distributions of pairs rejected by the ID and OD trigger requirement. The bottom panels show the prompt energy spectra of rejected background pairs.

6.6 Removal of PMT Flashing Events

A PMT sometimes produces a lot of spontaneous photons, known as "instrumental lights" without any physics reasons. The mechanism of the spontaneous light emission by a PMT is not well understood but probably generated by voltage discharge of a capacitor in the PMT base. Such flashing PMTs have been appearing intermittently and can be found in the monitoring stage of data-taking. The PMT flashing activity is apparently correlated with the temperature of the detector and the applied high voltage. The flashing rate increases with higher temperature and higher voltage. The events caused by the flashing PMTs contribute to the accidental background of IBD candidates. A flasher event has a specific PMT hit time and charge pattern. For identifying the flasher events, it is efficient to inspect a PMT hit charge information of Q_{tot} and Q_{max} in an extended timing window of 400 to 800 ns and impose a requirement of Q_{max}/Q_{tot}. Flashing light occurs randomly and thus leaves most of charges in off-time from the event time "t0" as shown in Figure 6.17. A requirement of $Q_{max}/Q_{tot} < 0.08$ can eliminate a large fraction of PMT flashing events.

- Ambient γ and flasher removal Q_{max}/Q_{tot} (-400 $\sim$ 800 ns) < 0.08

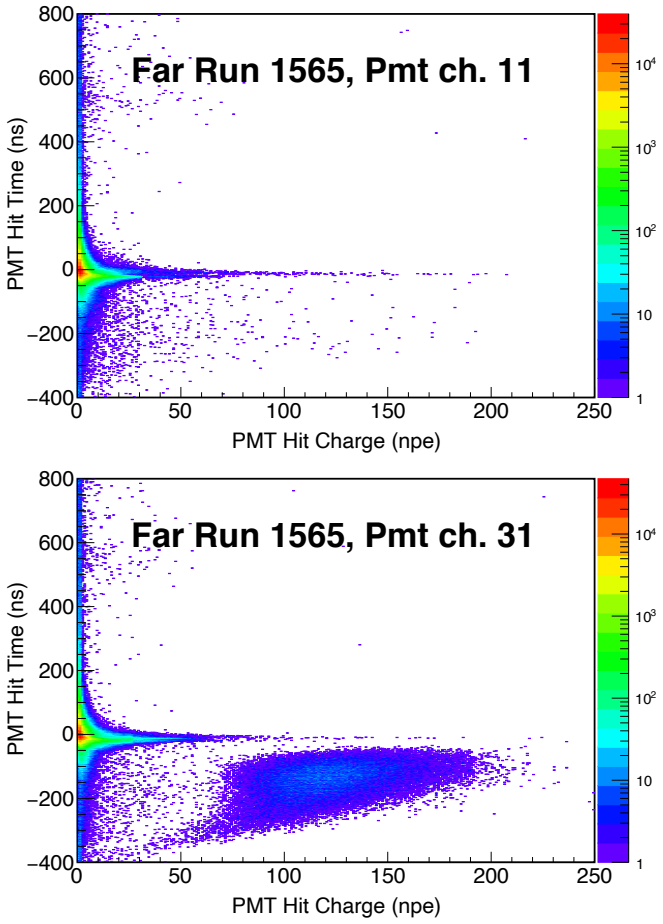

Figure 6.17: Comparison of PMT hit timing and charge distributions between a normal PMT (upper) and a flashing PMT (lower). The flashing PMT observes a large charge in early off-time before the event time "t0".

However, the requirement is not enough to remove all of PMT flashing events. A localized charge (Q_{loc}) is defined by the charge observed by the neighboring PMTs around a PMT with Q_{max} in a timing window of 400 to 800 ns. A smaller value of Q_{loc}/Q_{max} indicates a more isolated charge observed by the maximum charged PMT, a most likely flashing PMT. Therefore, most of the flashing events are eliminated by requiring a large value of Q_{max}/Q_{tot} and a small value of Q_{loc}/Q_{max}. Figure 6.18 shows distributions of Q_{max}/Q_{tot} and Q_{loc}/Q_{max} to identify the PMT flashing events. A more detailed description on the PMT flashing events can be found in Appendix A.

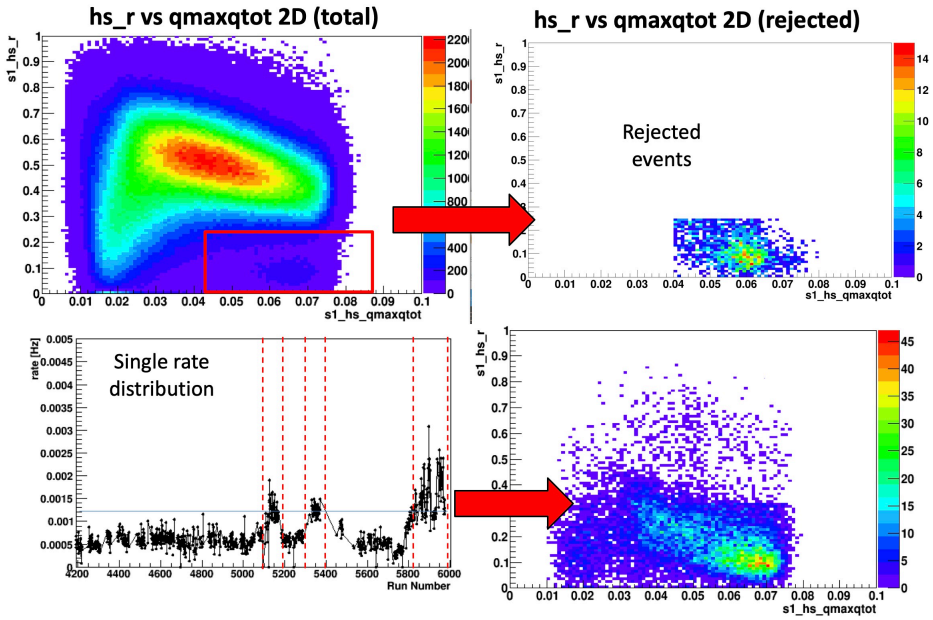

Figure 6.18: Distributions of Q_{max}/Q_{tot} and Q_{loc}/Q_{max} for PMT flashing events. The upper left plot shows the 2D distribution of Q_{loc}/Q_{max} vs. Q_{max}/Q_{tot} and the PMT flashing events in a box which are rejected by requiring small Q_{loc}/Q_{max} and large Q_{max}/Q_{tot} values. The lower left plot shows a single event rate as a function of run number or time. The lower right plot clearly shows flashing events in the 2D distribution of Q_{loc}/Q_{max} vs. Q_{max}/Q_{tot} time for a time period of the high single event rate.

6.7 IBD Candidate Sample

Detector	Data	DAQ live time (days)	Observed IBD candidates
FAR	Set A	384.473	27469
	Set B	2268.824	134643
NEAR	Set A	379.663	174524
	Set B	1879.635	540936

Table 6.5: The observed IBD candidates event rate at $1.2 < E_{prompt} < 8.0$MeV. for the far detector.

Applying the IBD selection criteria yields (162112) [(715460)] candidates events with E_{prompt} between 1.2 $\sim$ 8.0 MeV for a live time of (2653.297) [(2259.298)] days in FD [ND]. These IBD candidates include remaining backgrounds of uncorrelated and correlated pairs of prompt and delayed candidate events. The uncorrelated background is due to accidental coincidences coming from a random association of a prompt candidate event with a delayed event. The accidental background is mostly contributed by the ambient γ-rays below $\sim$3.5 MeV. The correlated backgrounds are due to fast neutrons, β-n emitters from cosmogenic ^{9}Li/^{8}He isotopes, and ^{252}Cf contamination in the target. In addition, the number of IBD signals is about 10 times larger than that of FD. Since the neutrino spreads radially, the observed number of neutrinos is inversely proportional to the square of the distance.

The total IBD signal loss due to all timing requirements for FD [ND] is (21.18 $\pm$ 0.01) [(38.256 $\pm$ 0.035)]% for Set A and (22.69 $\pm$ 0.10) [(43.056 $\pm$ 0.033)]% for Set B. The IBD signal loss due to the rest selection requirements at FD [ND] is (11.17 $\pm$ 0.01) [(21.28 $\pm$ 0.04)]% for Set A and (11.37 $\pm$ 0.01) [(27.18 $\pm$ 0.01)]% for Set B. The signal losses of individual requirements are given in Tables 6.6 and 6.7. Because of tight selection criteria against high backgrounds, the overall detection efficiency of FD [ND] is (23.0 $\pm$ 1.4) [(22.8 $\pm$ 0.9)]% for Set A and (21.8 $\pm$ 1.1) [(21.2 $\pm$ 0.8)]% for Set B, roughly 29.1 (28.8) % of the n-Gd efficiency. However, due to 2.8 times larger target volume than the n-Gd IBD detection, the observed number of n-H IBD candidates is more or less similar to that of the n-Gd sample.

Selection criteria	Set A	Set B	Set A+B
Muon Veto	11.271 $\pm$ 0.003	11.517 $\pm$ 0.001	11.450 $\pm$ 0.001
Any Trigger before 300 (500) μs	3.679 $\pm$ 0.001	5.688 $\pm$ 0.001	5.135 $\pm$ 0.001
Pair multiplicity within 600 μs	2.503 $\pm$ 0.001	0.778 $\pm$ 0.001	1.252 $\pm$ 0.001
ID Trigger after 800 μs	5.367 $\pm$ 0.001	5.050 $\pm$ 0.001	5.137 $\pm$ 0.001
ID & OD Trigger after 100 (200) μs	0.048 $\pm$ 0.001	0.247 $\pm$ 0.020	0.192 $\pm$ 0.014
Hotspot removal	-	0.251 $\pm$ 0.024	0.182 $\pm$ 0.017
Flasher requirement	-	1.172 $\pm$ 0.128	0.850 $\pm$ 0.093
Combined	21.184 $\pm$ 0.003	22.687 $\pm$ 0.103	22.274 $\pm$ 0.075

Table 6.6: Signal loss for FD. The loss is determined by muon or trigger rates.

Selection criteria	Set A	Set B	Set A+B
Muon Veto	21.594 ± 0.003	21.541 ± 0.002	21.547 ± 0.001
Any Trigger before 300 (500) μs	13.190 ± 0.001	20.820 ± 0.001	18.947 ± 0.001
Pair multiplicity within 600 μs	4.231 ± 0.001	1.351 ± 0.001	2.058 ± 0.001
ID Trigger after 800 μs	4.369 ± 0.001	4.259 ± 0.001	4.286 ± 0.001
ID & OD Trigger after 100 (200) μs	0.099 ± 0.056	2.621 ± 0.054	2.220 ± 0.043
Hotspot removal	-	-	-
Flasher requirement	-	0.336 ± 0.020	0.254 ± 0.015
Combined	38.256 ± 0.035	43.056 ± 0.034	41.877 ± 0.027

Table 6.7: Signal loss for ND. The loss is determined by muon or trigger rates.

Chapter 7

Estimation of Remaining Backgrounds

The remaining backgrounds after event selection requirements consist of three main backgrounds due to accidentals, fast neutrons, and beta-n emitters from cosmogenic ^{9}Li/^{8}He as shown in Figure 7.1. The Set B data sample includes an additional background due to the ^{252}Cf contamination. The most dominant background comes from the random coincidence between the prompt and delayed candidates. The spectral shapes and rates of the remaining backgrounds need to be measured in order to be subtracted from the final IBD candidate sample. They are measured from background enriched samples; thus, their uncertainties can be reduced with more data. Because of higher backgrounds due to the lower energy of the n-H delayed signal than the n-Gd sample, the remaining backgrounds must be estimated accurately for a precise measurement of θ_{13}. The following subsections describe how to obtain the remaining backgrounds.

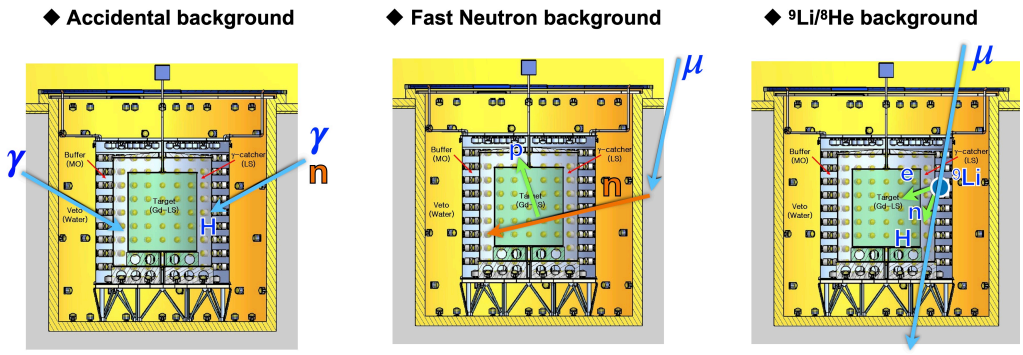

Figure 7.1: Schematic description of remaining backgrounds in the n-H final sample. There are three main background components of accidentals, fast neutrons, and beta-n emitters from cosmogenic ^{9}Li/^{8}He.

7.1 Accidental Background

The accidental background is uncorrelated between the prompt and delayed candidates and comes from the random association of a prompt-like event due to radioactivity and a delayed-like event due to cosmic muon-induced neutron capture. The prompt-like events are mostly ambient γ-rays from the radioactivity in the PMT glasses, LS, and surrounding rock. Most ambient radioactivities generate under ~3.5 MeV γ rays. The delayed-like events originate from neutrons produced by high-energy cosmic rays in the surrounding rocks or the detector.

The delayed event candidate of the n-H analysis requires an event near 2.2 MeV as a γ-ray from neutron capture on H and, therefore, suffers from extremely high ambient γ-rays. The prompt candidate rate of FD is roughly 1.7 times higher than ND due to more radioactivity in the surrounding rocks. This results in higher accidental backgrounds of FD than ND.

An accidental background sample is obtained by requiring temporal dissociation between prompt- and delayed-like events, i.e., $\Delta T > 1$ ms for the IBD sample with no ΔR requirement. The prompt energy spectra of the accidental backgrounds of ND and FD are shown in Figures 7.2 and 7.3. In Figure 7.3, the prompt energy spectra with $\Delta R > 2000$ mm are unchanged for various ΔT

requirements. On the other hand, the prompt spectral shapes withΔT $>$ 1 ms are affected by the spatial coincidence requirements of ΔR as shown in Figure 7.3. Therefore, a requirement of ΔR $<$ 450 mm, the same as the IBD selection criterion, is applied to the accidental background sample.

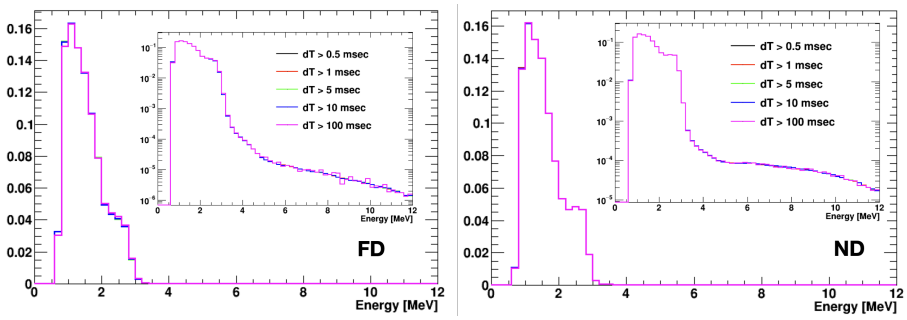

Figure 7.2: Energy spectra obtained from accidental background control samples of ΔT $>$ 1 ms. The spectral shape changes a little bit by the ΔR spatial coincidence conditions.

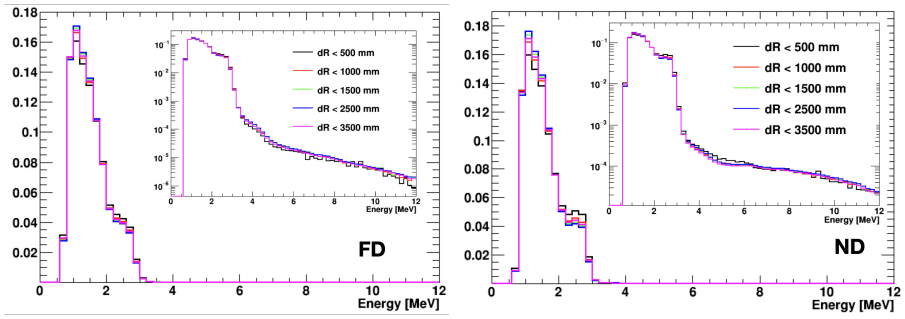

Figure 7.3: Accidental shape for different ΔR at the FD and ND with ΔT $>$ 1 ms. The prompt signal energy spectrum of accidental background is affected by ΔR. The red line is used because the same criteria as those of IBD must be applied.

The remaining rate in the final sample is estimated by measuring the rate of random spatial associations in the IBD signal region of ΔR $<$ 450 mm, extrapolated from the dominant background region of ΔR $>$ 2000 mm using the ΔR distribution of the accidental background spectrum as shown in Figure 7.4. It can be seen that two components show peaks at $\sim$300 mm and peaks at $\sim$2800 mm in both ND and FD. The first component is the IBD signal, which is the neutron capture distance, usually within 1000 mm. The accidental background is no

correlation between prompt signal and delayed signal, so the ΔR is determined by the size of the detector. Since the ΔR distribution of the two components is different, the amount of accidental as a red line can be obtained via adjusting to minimize the spectrum difference at ΔR > 2000 mm from the black line. After adjusting the amount of accidental background, the amount of remaining accidental background within 450 mm of ΔR can be obtained.

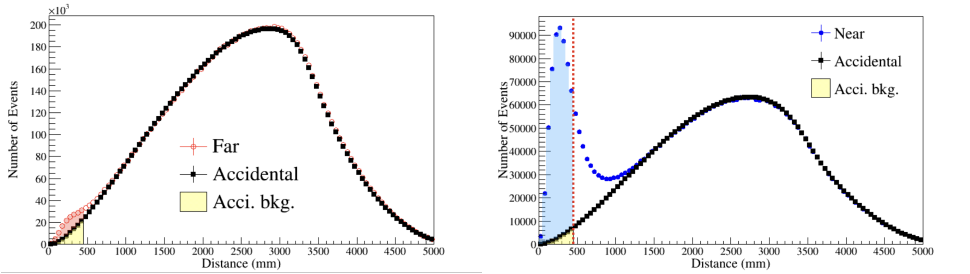

Figure 7.4: Spatial correlation (ΔR) distribution of IBD candidates with no ΔR requirement for FD (red dots) and ND (blue dots). The amount of accidental background is obtained by a fit to data at ΔR > 2000 mm using the random ΔR distribution (black dots) from the accidental background enriched sample.

Based on the measured accidental rate remaining in the IBD candidate sample, the prompt energy spectra after subtracting the accidental background are obtained as shown in Figure 7.4. This process gives the prompt signal energy spectrum of the IBD candidate without accidental background, as shown in Figure 7.5.

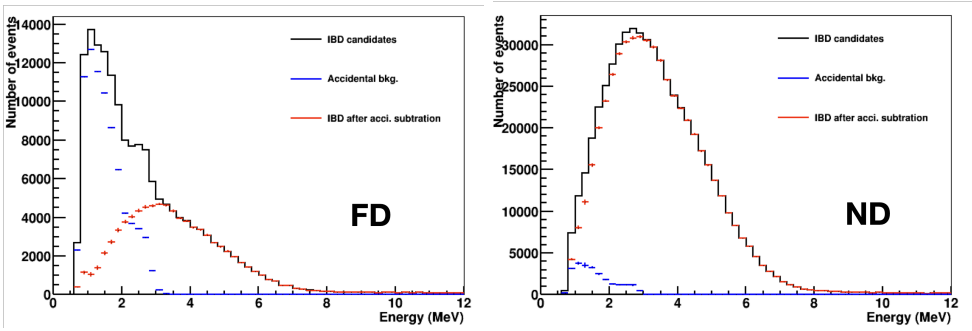

Figure 7.5: Prompt energy spectra after subtracting the accidental background for FD and ND as shown by red histograms are obtained as shown in Figure 7.4. The accidental background of FD is roughly three times larger than ND.

The amount of the remaining accidental background in the final sample is

again measured as a consistent check by a fit to the energy distribution of the IBD candidates using the accidental spectrum and the obtained accidental background subtracted spectrum from the ΔR fit as shown in Figure 7.6.

The remaining accidental rates in the final samples are obtained and given in Table 7.1. The accidental fraction in the IBD final sample is ∼37.1% for FD and ∼2.8% for ND.

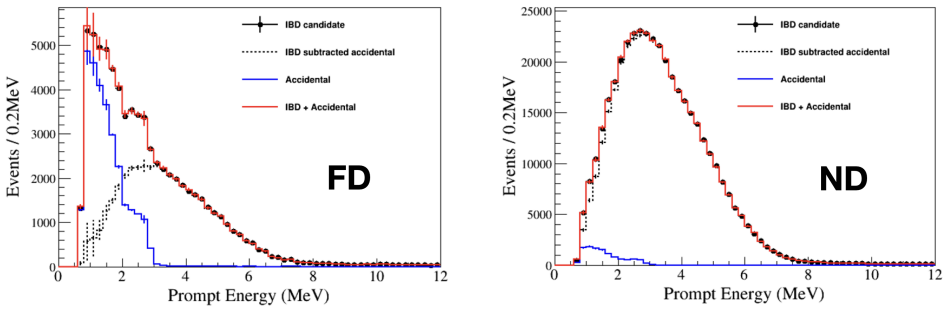

Figure 7.6: Estimation of the remaining accidental background in the final sample by a fit to the energy distribution of the IBD candidates (black) using the accidental spectrum (blue) and the obtained accidental background subtracted spectrum (red) from the ΔR fit.

Detector	Period	Accidental Background (/day)
Far	Set A	21.82 ± 0.02
	Set B	22.77 ± 0.01
Near	Set A	7.95 ± 0.01
	Set B	8.79 ± 0.01

Table 7.1: Results of estimation of accidental background at the FD and ND.

7.2 Fast Neutron Background

The fast neutrons are produced by cosmic muons traversing the surrounding rock and the detector. An energetic neutron entering the ID can interact in the LS to produce a recoil proton before being captured on H or Gd. The recoil proton generates scintillation lights mimicking a prompt-like event that is paired with the delayed signal of the neutron capture on H.

Fast neutrons create visible energies up to more than 100 MeV by the recoil proton. Figure 7.7 shows the prompt energy distribution, which appears to

decrease gradually as energy increases. In this n-H analysis, the fast neutron background shows an exponential shape spectrum while it shows a flat spectrum in the target region of the n-Gd analysis.

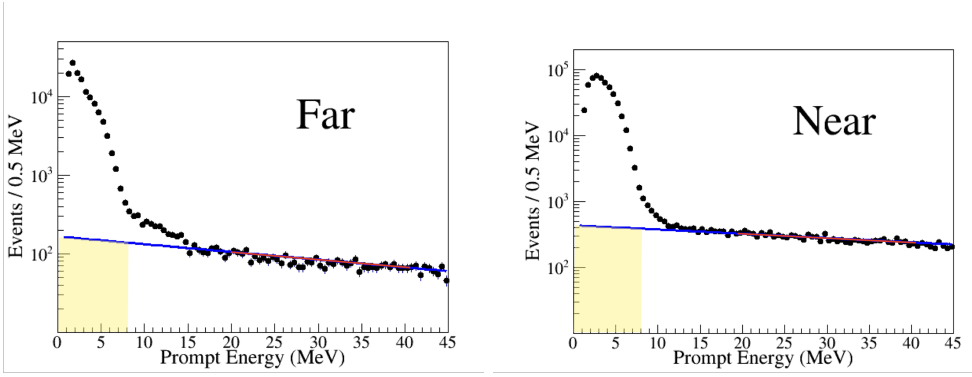

Figure 7.7: Prompt energy spectra of IBD candidates including an exponential spectrum of fast neutrons above 12 MeV. The fast neutron background rate in the IBD candidates is estimated by extrapolating from the dominant background region assuming an exponential spectrum of the background (blue exponential fit).

The fast neutron background rate in the final IBD candidate sample is estimated by being extrapolated from the background dominant energy region of $12 < E_{prompt} < 44$ MeV to the IBD signal region of $1.2 < E_{prompt} < 8.0$ MeV, assuming an exponential spectrum of the background as shown in Figure 7.7. The fitting range for data set B is changed due to the ^{252}Cf contamination. The fitting range for the fast neutron spectrum at both FD and ND is chosen as below:

$$\text{Set A} : 12 \sim 44 \text{ MeV}$$
$$\text{Set B} : 20 \sim 44 \text{ MeV}$$

A fast neutron enriched sample is obtained by selecting IBD candidates that are accompanied by any single events of $E_{prompt} > 0.7$ MeV within 400 μs subsequent window. This sample also contains some IBD candidates due to the time selection requirement, as shown in the prompt spectra of Figure 7.8. The rate of the remaining IBD candidates is estimated by the distribution of the time difference between an IBD pair and its accompanied single event, as shown in Figure 7.9. The distributions clearly show a short-time correlated component of fast neutrons, while a long-time component represents the IBD candidates. The contained IBD candidate rate is estimated by a fit to the long-time component.

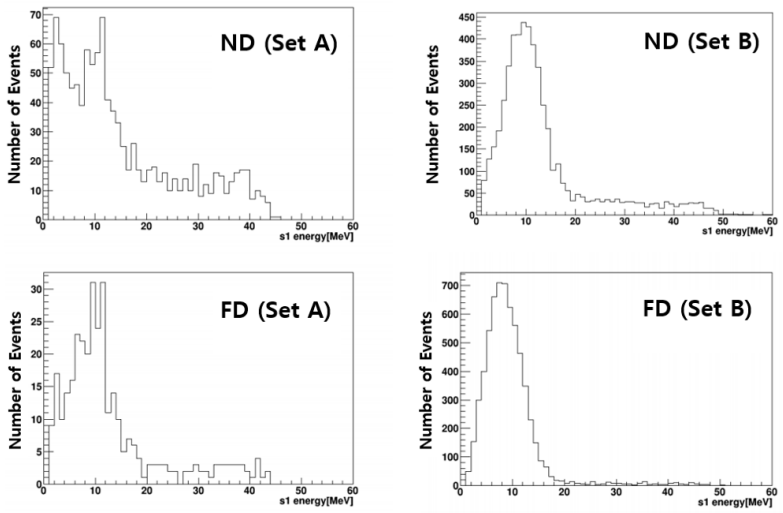

Figure 7.8: Prompt energy spectra of fast neutron enriched sample at FD and ND. This sample contains some IBD candidates due to the time selection requirement.

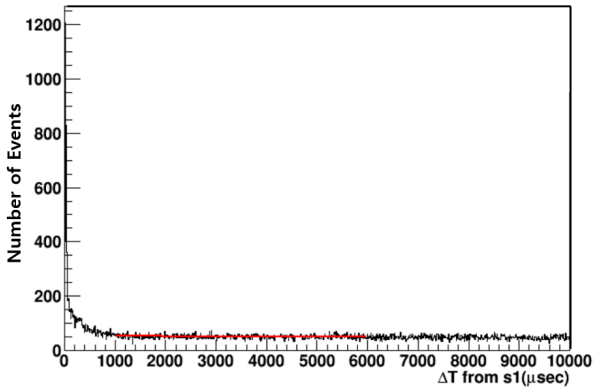

Figure 7.9: Distributions of the time difference between an IBD pair and its accompanied single event. The contained IBD candidate rate is estimated by a fit to the long-time component underneath a short-time correlated component of fast neutrons.

Based on the estimated rate, the IBD prompt spectrum is subtracted from the prompt spectrum of the fast neutron enriched sample to obtain the fast neu-

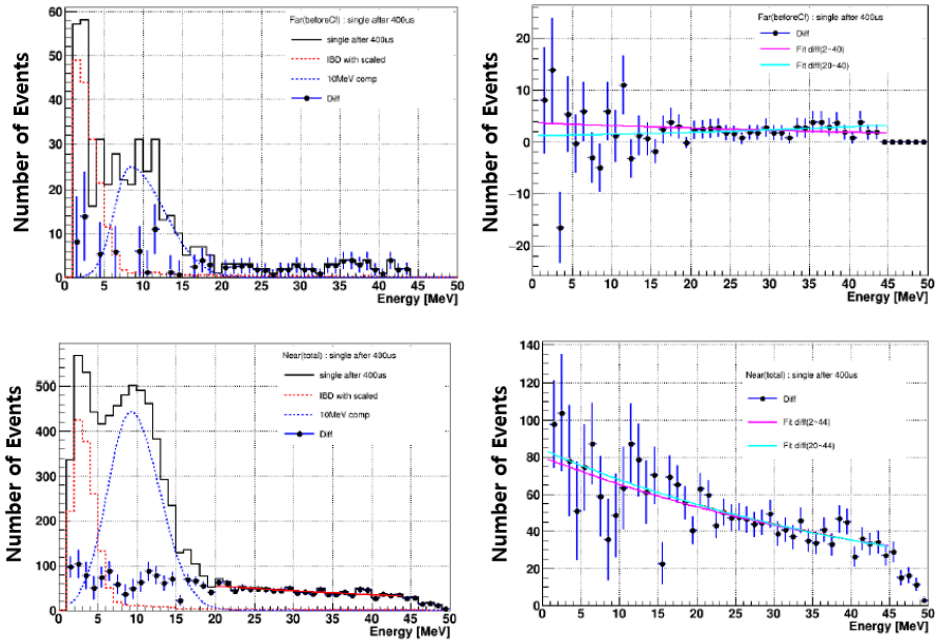

Figure 7.10: Prompt spectra of fast neutrons after removing the IBD candidates and the 10 MeV Gaussian component from the fast neutron enriched sample. Exponential prompt spectra are obtained for fast neutrons.

tron prompt spectrum. However, a Gaussian shape component remains at 10 MeV, Figure 7.10 shows the prompt spectra of fast neutrons after removing the IBD candidates and the 10 MeV Gaussian component, showing an exponential spectrum. The spectral shape uncertainty of the fast neutron background is estimated by a possible deviation from the exponential spectrum if the fitting range is changed. The estimated shape uncertainties are given in Table 7.2.

Detector	Spectrum Uncertainty (%)
FD	19.74
ND	4.74

Table 7.2: Estimated prompt spectral uncertainties of fast neutrons at FD and ND.

The estimated rates of fast neutron backgrounds remaining in the IBD sample are given in Table 7.3, corresponding to roughly 1% of the sample at both FD

and ND.

Detector	Period	Fast Neutron (/day)
FD	Set A	0.77 ± 0.17
	Set B	0.83 ± 0.13
ND	Set A	3.42 ± 0.08
	Set B	3.01 ± 0.13

Table 7.3: Estimated rates of fast neutron backgrounds in the IBD sample

7.3 Cosmogenic ^{9}Li/^{8}He Background

High-energy cosmic muons produce unstable isotopes of ^{9}Li/^{8}He through interaction with carbon atoms in the detector. They emit a β- particle as well as a neutron from a subsequent decay (τ = 257.2 ms, Q = 13.6 MeV for ^{9}Li and τ = 171.7 ms, Q = 10.7 MeV for ^{8}He) to mimic the IBD signal.

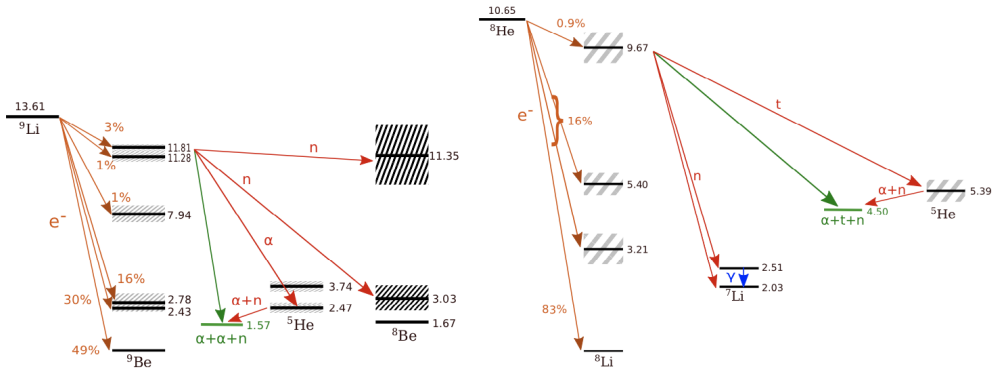

Figure 7.11: Decay scheme of ^{9}Li/^{8}He [69]. The decay schemes of ^{9}Li and ^{8}He are drawn at the highest energy levels. The β decay branching ratio is shown along with some possible decay paths. Particles that are emitted during the transition between levels can be found above the red arrows, and the green arrows indicate a direct tree body break-up.

The β-n decay scheme is shown in Figure 7.12. The spectral shape of the ^{9}Li/^{8}He background is obtained using a sample of IBD-like pairs, which are produced within 500 ms (400 ms) by energetic muons of $E_{\mu} > 1.5$ GeV (> 1.6 GeV)

for FD (ND). The time difference distribution between an energetic muon and a subsequent IBD candidate is shown in Figure 7.12.

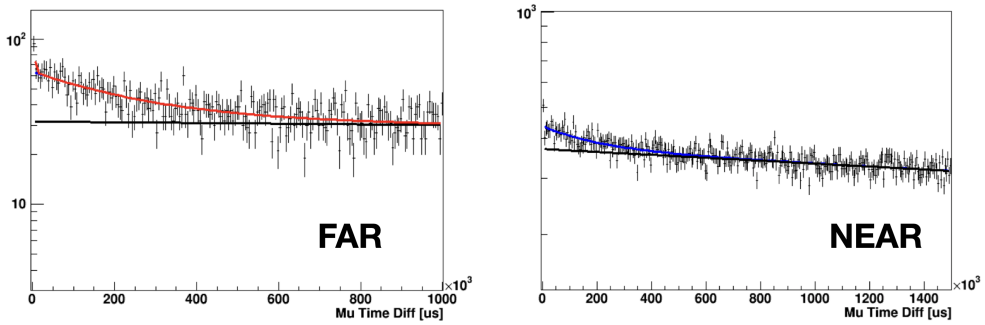

Figure 7.12: Decay time distribution of the IBD-like pairs from their preceding energetic muons in FD (left) and ND (right) detectors. The ^{9}Li/^{8}He background is seen with a measured mean decay time of ∼250 ms, indicating predominant production of ^{9}Li over ^{8}He, while muon-induced accidental background events are observed right after the preceding muons.

Based on their observed spectra, the shortest decay-time component is found to be the muon-induced accidental background followed by the ^{9}Li/^{8}He background. The IBD signals are temporally uncorrelated with muon events, and their time differences are distributed according to the IBD rate. The measured mean decay time of ∼250 ms indicates the predominant production of ^{9}Li over ^{8}He.

The prompt signal energy spectrum of ^{9}Li/^{8}He is required for the remaining background measurements. Figure 7.13 shows the distribution of the elapsed time from a preceding muon consisting of three different backgrounds of timing components as below:

- Muon accidental (short-time component)
- ^{9}Li/^{8}He (medium-time component)
- IBD candidates (long-time component)

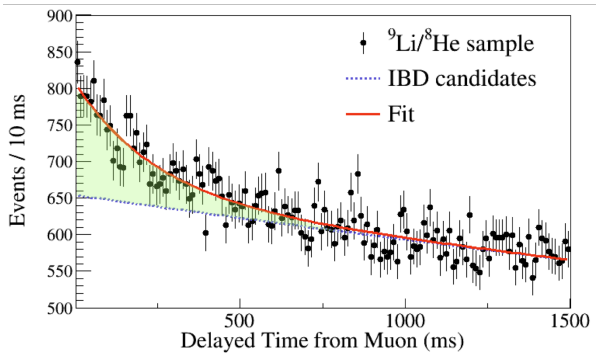

Figure 7.13: Delayed time distribution of the ^{9}Li/^{8}He enriched IBD candidates from their preceding energetic muons. The ^{9}Li/^{8}He background is clearly seen with a measured mean decay-time of ∼250 ms while a long-time component comes from the IBD candidates.

The measured prompt-energy spectrum of the ^{9}Li/^{8}He background is obtained by subtracting the energy spectra of the IBD candidates and the muon-induced accidental background from that of the ^{9}Li/^{8}He enriched sample, as shown in Figure 7.14. The rates of subtracted IBD candidates and accidentals are determined by the fit to the delayed time distribution. Figure 7.15 shows the obtained prompt-energy spectra at FD and ND with errors estimated from the spectral subtraction. The energy shape uncertainty comes from statistical uncertainty of the ^{9}Li/^{8}He enriched sample and, therefore, is expected to be reduced by more data.

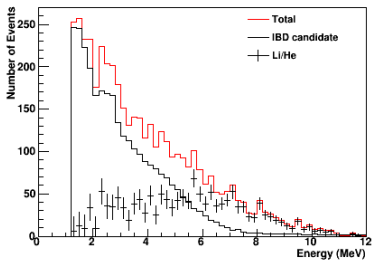

Figure 7.14: Measured prompt-energy spectrum of the ^{9}Li/^{8}He background (cross) obtained by subtracting the energy spectra of the IBD candidates (black histogram) and the muon-induced accidental background from that of the ^{9}Li/^{8}He enriched sample (red histogram). The rates of subtracted IBD candidates and accidentals are determined by the fit to the delayed time distribution.

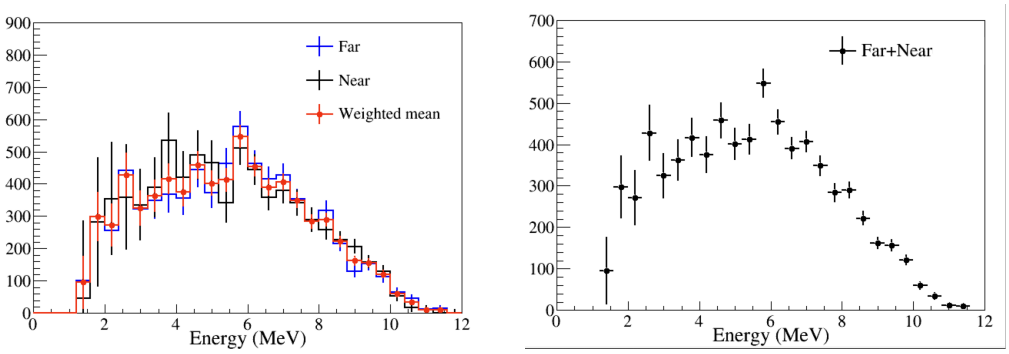

Figure 7.15: Measured prompt-energy spectra at FD and ND with errors estimated from the spectral subtraction (left). The two spectra at FD and ND are combined by an error-weighted mean (right).

The remaining ^{9}Li/^{8}He background rate in the IBD signal region of E_{prompt} < 8 MeV is estimated by extrapolating from the background dominant region of E_{prompt} > 8 MeV using the measured background spectrum, as shown in Figure 7.16. The background rate in the region of E_{prompt} > 8 MeV is estimated by a fit to the IBD candidate data using the measured ^{9}Li/^{8}He background spectrum, the measured fast neutron background, and the MC IBD expectation. The best fit is found to minimize the χ^2 below:

$$\chi^2 = \sum_{i=bin} \left(\frac{N_i^{obs} - N_i^{exp}}{\sqrt{N_i^{obs}}} \right)^2 + \left(\frac{f}{\sigma_f} \right)^2 + \sum_i \left(\frac{f_{s_i}}{\sigma_{f_{s_i}}} \right)^2 \tag{7.1}$$

$$E_i = \alpha \cdot n_{LH}^i + n_{IBD\ MC}^i + (1 + f + f_{s_i}) \cdot n_{FN}^i \tag{7.2}$$

- N_i^{obs} : number of IBD candidate
- n_{LH} : number of ^{9}Li/^{8}He
- n_{FN} : number of fast neutron
- $n_{IBD\ MC}$: number of expected IBD
- α : scale factor for the amount of ^{9}Li/^{8}He
- f : pull parameter for magnitude uncertainty of fast neutron
- f_{s_i} : pull parameter for shape uncertainty of fast neutron

- σ_f : magnitude uncertainty of fast neutron
- $\sigma_{f_{si}}$: shape uncertainty of fast neutron

The remaining fast neutron rate only is first obtained above 12 MeV and next constrained for determining the ^{9}Li/^{8}He rate. The best-fit results are obtained as shown in Figure 7.16. The estimated ^{9}Li/^{8}He background rates are summarized in Table 7.4.

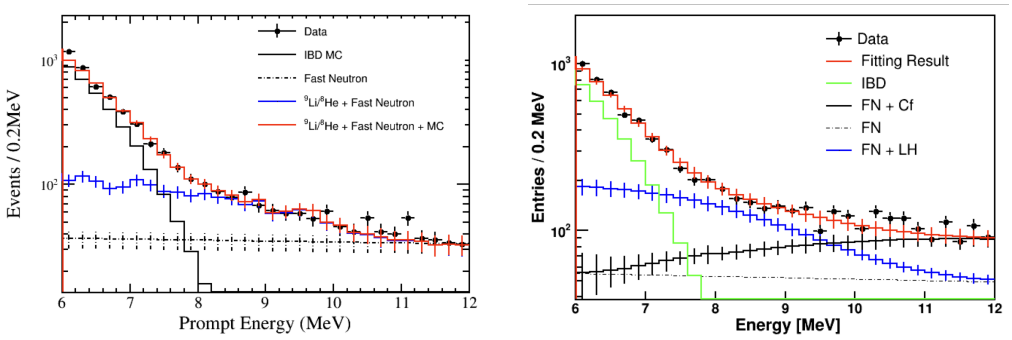

Figure 7.16: Estimation of the remaining ^{9}Li/^{8}He background rate in the signal region using the measured rate in the dominant background region of $E_{prompt} >$ 8 MeV at FD and ND. The background rate in the signal region of $E_{prompt} < 8$ MeV is estimated by extrapolating from the dominant background region using the measured background spectrum.

Detector	Period	^{9}Li/^{8}He (/day)
FD	Set A	1.60 ± 0.35
	Set B	1.49 ± 0.23
ND	Set A	7.44 ± 0.82
	Set B	6.08 ± 0.59

Table 7.4: Estimated ^{9}Li/^{8}He background rates at FD and ND.

7.4 ^{252}Cf Background

The ^{252}Cf background comes from the contamination of Gd-LS by a small amount of ^{252}Cf that was accidentally introduced into both detectors during detector calibrations in October 2012. Because of a loose seal of the source container, Gd-LS seeped into the source container, and a small amount of dissolved ^{252}Cf

leaked into Gd-LS. It is known that a ^{252}Cf decay emits 3.7 neutrons per fission on average with a mean energy of 2.1 MeV per neutron, via α emission (96.9%) and spontaneous fission (3.1%). Data Set B suffers from the ^{252}Cf contamination background in the target region due to released neutrons captured on Gd mostly and H partly. The remaining ^{252}Cf background spectrum peaking at ~11 MeV is obtained from the ^{252}Cf contamination candidate events as shown in Figure 7.17. The remaining ^{252}Cf background rate in the IBD signal region of $1.2 < E_{prompt} < 12$ MeV is estimated by extrapolating from the background dominant region of $12 < E_{prompt} < 20$ MeV using the measured background spectrum, as shown in Figure 7.18. The measured rate of remaining ^{252}Cf background is 0.10 ± 0.01 events per day at FD and close to null at ND.

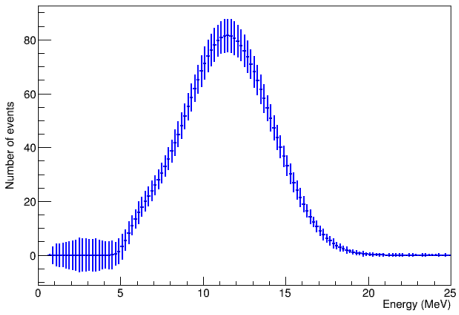

Figure 7.17: Prompt energy spectrum of ^{252}Cf background. The errors represent estimated shape uncertainties.

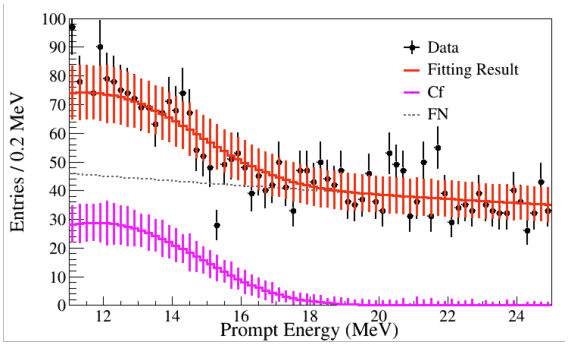

Figure 7.18: Estimation of remaining ^{252}Cf background rate in the IBD signal region using the measured rate in the background dominant region of $12 < E_{prompt} < 20$ MeV at FD.

7.5 Summary of Remaining Background Rates

The total remaining background rates for $1.2 < E_{prompt} < 8$ MeV in the final IBD candidate samples are estimated as 25.45 ± 0.21 (FD) and 17.89 ± 0.42 (ND) events per day. After the background subtraction, the IBD signal rates are 35.64 ± 0.30 (FD) and 298.78 ± 0.63 (ND) events per day. Table 7.5 summarizes the observed IBD and estimated background rates. The fraction of total background is ∼41.6% at FD and ∼5.7% at ND as shown in Figure 7.19.

	ND	FD
IBD candidates	715,443	162,113
Accidental background (/day)	10.63 ± 0.01	18.64 ± 0.01
Fast neutron (/day)	3.04 ± 0.10	0.82 ± 0.13
^{9}Li/^{8}He (/day)	5.95 ± 0.41	1.49 ± 0.18
^{252}Cf (/day)	-	0.100 ± 0.018
Total background (/day)	17.89 ± 0.42	25.45 ± 0.21
After background subtraction(/day)	298.78 ± 0.63	35.64 ± 0.30

Table 7.5: Observed IBD and estimated background rates per day for $1.2 < E_{prompt} < 8$ MeV.

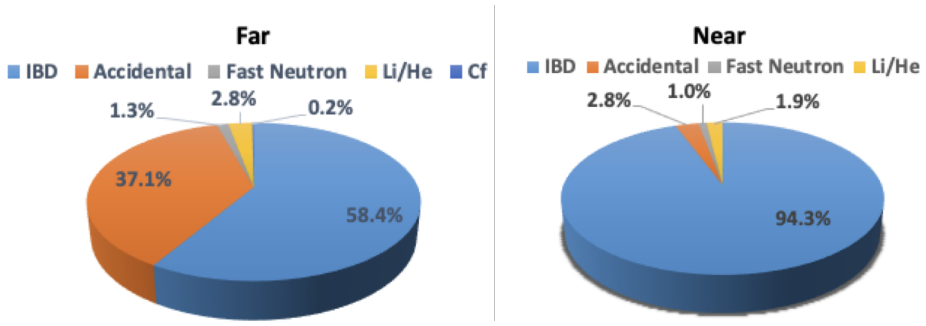

Figure 7.19: Fraction of IBD and backgrounds in total.

Chapter 8

Systematic Uncertainty

Sources of systematic uncertainties are energy scale, backgrounds, detection efficiency, and reactor $\overline{\nu}_e$flux. For this far-to-near ratio measurement the only uncorrelated systematic uncertainties contribute to the errors of measured values. The uncorrelated uncertainty of energy scale is 0.5% while the correlated uncertainty is 1.5%. The energy-dependent detection efficiency is not considered in this analysis. Because of the difference in overburden, we assume no correlated uncertainties of backgrounds between FD and ND. Therefore, to be conservative, the background uncertainty of each detector is fully taken as an uncorrelated systematic one.

8.1 Detector Related Uncertainty

The detector-related uncertainties are either correlated or uncorrelated between ND and FD. The correlated uncertainty is common to both detectors and thus cancels out for this far-to-near ratio measurement. An individual detector efficiency is measured from an IBD signal-enriched sample, and its uncertainty is given by statistical uncertainty and uncorrelated and correlated systematic uncertainties. An expected number of IBD interactions is determined by reactor fluxes, an IBD cross-section, and a total number of free protons in the target. The uncertainty of the IBD cross-section from a theoretical calculation [51, 52, 70] is 0.09% and can be ignored by this relative measurement. The number of free protons in the target and γ-catcher is estimated as $(3.299 \pm 0.023) \times 10^{30}$. The uncorrelated systematic uncertainty of the number of free protons is 0.03%, estimated from the measured volume difference between the FD and ND vessels [67, 71]. The correlated uncertainty is 0.7%, estimated from the hydrogen composition and the density of the liquid scintillator.

The n-H selection criteria are tighter than the n-Gd because of higher back-

grounds. Since FD and ND are identical, Therefore, the n-H detection efficiency is smaller than the n-Gd and its uncertainty is different from the n-Gd, not much different due to identical ND and FD. While both detectors are identical, there may be a small difference and uncorrelated between them. The uncorrelated uncertainty of detection efficiency is included in the measurement of θ_{13} value.

Acceptance and trigger efficiency

The trigger efficiency is determined by the IBD signal loss due to the requirement of ID Nhit > 90. The IBD signal loss due to the acceptance and trigger requirement comes mostly from events occurring at the outer layer of the γ-catcher and emitting minimal scintillating lights with leaving most energy in the buffer region of non-scintillating oil. The RENO Monte Carlo simulation does not reproduce the data Nhit well due to the lack of realistic individual-channel simulation for the p.e. threshold and dark or noise hits. According to a comparison of Nhit distribution between data and MC simulation, a MC equivalent requirement of Nhit > 84 is found to accept an ID trigger. The acceptance and trigger efficiency is estimated from the IBD signal loss due to the requirement using the MC and to be $78.8 \pm 1.5\%$. The efficiency difference between FD and ND is simulated by MC and determined to be 0.02% as an uncorrelated uncertainty. Table 8.1 summarizes the uncertainties including geometrical acceptance as shown in Figure 8.1.

Efficiency (%)	Combined	Uncorrelated
Trigger Efficiency	94.24	0.01
Geometrical and kinematic acceptance	83.61	0.01
Acceptance and trigger efficiency	78.81 ± 1.5	0.02

Table 8.1: Efficiency and uncertainty of acceptance and trigger requirement.

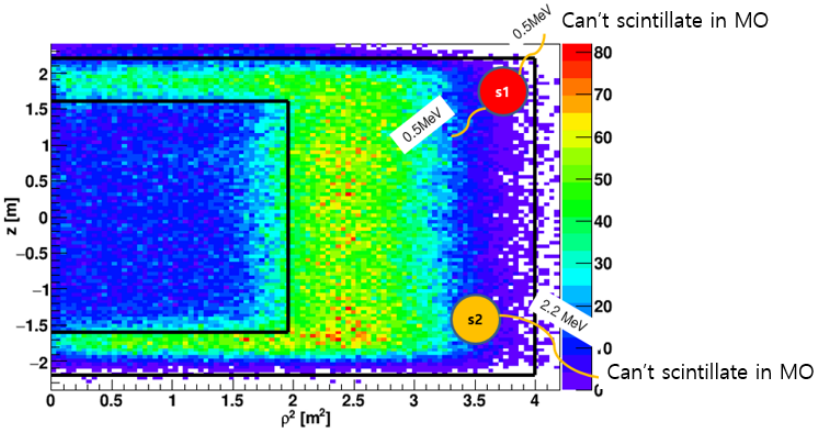

Figure 8.1: Geometrical and kinematic acceptance. Outside of the outermost solid line is filled with non-scintillating mineral oil. When γ-ray enters into the region before scintillating, it can not emit photoelectrons. In this case, the Nhit threshold is not satisfied. The rejected prompt events is $\sim$1.5% and rejected delayed events is $\sim$19.5%

Neutron H capture fraction

The neutron capture fraction on H is estimated based on the ratio of neutron captures on H relative to total neutron captures of the IBD signal in the target and γ-catcher regions. In the target region, neutrons can be captured by H or Gd. The fraction of neutron capture by C is less than 0.1% and can be neglected. The neutron H capture fraction and uncorrelated uncertainty in the target plus γ-catcher region are determined to be (63.61 $\pm$ 0.42)% and 0.04%.

Prompt Energy Requirement

The efficiency of the prompt energy requirement, $1.2 < \mathrm{E_{prompt}} < 8.0$ MeV, is estimated by the fraction of events in the region relative to total IBD events and estimated using MC as given in Table 8.2. The correlated uncertainty is estimated to be 0.1% by varying the energy threshold according to the energy-scale uncertainty of 1.5%. The uncorrelated systematic uncertainty is estimated to be 0.08% by varying the energy threshold according to the energy-scale difference of 0.5% between FD and ND as given in Table 8.3.

Detector	Far	Near	Combined
Efficiency (%)	97.8 ± 0.1	97.8 ± 0.1	97.8 ± 0.1

Table 8.2: Efficiency of prompt energy requirement at FD and ND. The combined efficiency is obtained as a weighted mean.

Criteria of Prompt Energy	Efficiency Difference
−0.5%	0.03%
+0.5%	−0.08%

Table 8.3: Uncorrelated systematic uncertainty of the prompt energy requirement. The uncertainty is estimated by varying the energy threshold according to the energy-scale difference of 0.5% between FD and ND.

Delayed Energy Requirement

The efficiency of the delayed energy requirement, 2.2 MeV ± 2σ, is determined by the fraction of delayed events in the region out of total delayed events of neutron capture on H. An IBD event enriched sample is used for the efficiency estimation and obtained by requiring IBD candidates to have $3.5 < \mathrm{E_{prompt}} < 8$ MeV to eliminate accidental background and $\Delta\mathrm{R} < 450$ mm.

- $\mathrm{E_{prompt}} > 3.5$ MeV
- $\Delta\mathrm{R} < 450$ mm

Figure 8.2 shows the delayed energy distribution of the IBD enriched sample. The efficiency (ε) is estimated from the distribution as below,

$$\varepsilon = \frac{N_{-2\sigma<\mathrm{E_{delayed}}<+2\sigma}}{N_{\mathrm{E_{delayed}}<3.0\ \mathrm{MeV}}} \tag{8.1}$$

where $N_{-2\sigma<\mathrm{E_{delayed}}<+2\sigma}$ is number of events selected by the delayed energy requirement and $N_{\mathrm{E_{delayed}}<3.0\ \mathrm{MeV}}$ is the number of events below 3 MeV. The estimated efficiencies are given in Tables 8.4. The 2σ requirement expects a defined efficiency of 95%. The efficiency of the delayed energy requirement is obtained to be 86.16%. The uncorrelated uncertainty was estimated to be 0.08% based on the energy scale difference as given in Tables 8.5.

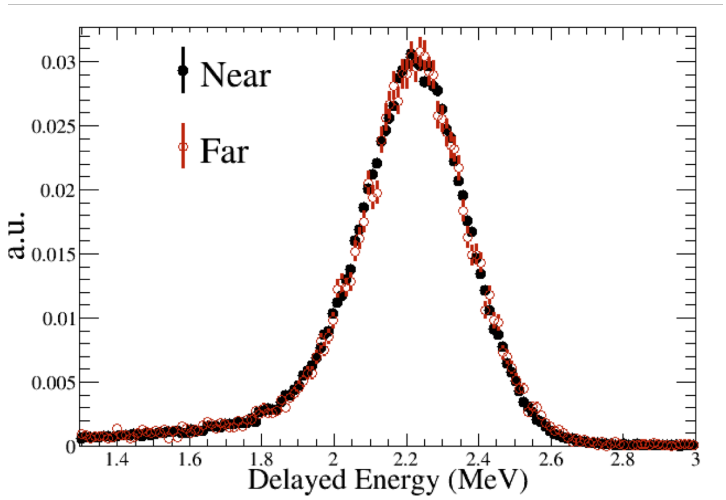

Figure 8.2: Delayed energy distributions of the IBD enriched samples at FD and ND. The delayed signals peak at 2.2 MeV and are selected in the 2σ region around the peak energy.

Detector	Far	Near	Combined
Efficiency (%)	86.24 ± 0.25	86.16 ± 0.08	86.16 ± 0.08

Table 8.4: Efficiency of delayed energy requirement at FD and ND.

Criteria of Delayed Energy	Efficiency Difference
−0.5%	−0.05%
+0.5%	0.08%

Table 8.5: Uncorrelated systematic uncertainty of the delayed energy requirement. The uncertainty is estimated by varying the energy threshold according to the energy-scale difference of 0.5% between FD and ND.

Time Coincidence

The efficiency of the time coincidence requirement is determined by the fraction of IBD events with $2 < \Delta T < 400$ μs out of total IBD events. An IBD signal enriched sample is obtained by requiring IBD candidate events with $3.5 < E_{prompt}$

< 8 MeV in order to eliminate the accidental background. Figure 8.3 shows ΔT distributions of the neutron capture on H for the ND and FD IBD signal enriched samples. A fits to the ΔT distribution is performed by two exponential functions plus a constant. The distributions are well described by

$$N(t) = p_0 e^{-t/p_1} + p_2 e^{-t/p_3} + p_4 \tag{8.2}$$

where p_0, p_1, p_2, p_3 and p_4 are determined by a fit to data. The two exponential functions represent the capture time distribution of the IBD events with neutron captures on H in the target and γ-catcher regions. The constant term represents the accidental background.

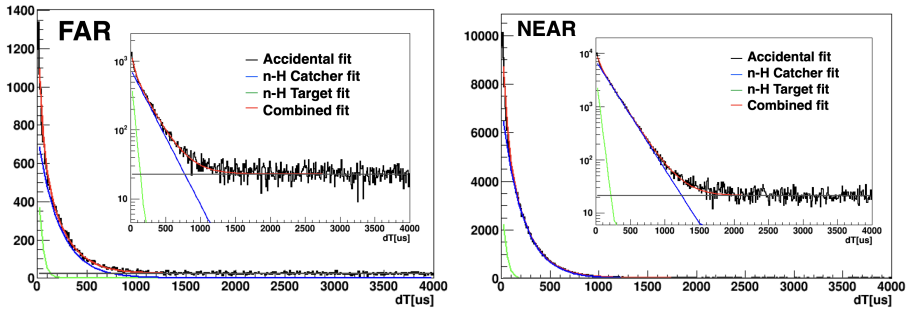

Figure 8.3: Measured time distributions of neutron capture on H at FD and ND. The red solid curves are the fits to the data, and the blue (green) lines are the fitted capture time distributions of the IBD events in the γ-catcher (target) region. The mean capture time in the target region is $\sim$30 μs, shorter than that in the γ-catcher region, $\sim$200 μs, due to influence of Gd with a larger capture cross-section than H.

The efficiency (ε) is obtained by the fraction of IBD events with $2 < \Delta\mathrm{T} < 400$ μs out of the total IBD events that are estimated from the fitted mean values of capture times using the first two exponential function as below,

$$\varepsilon = \frac{N^{exp1}_{2<\Delta\mathrm{T}<400\ \mu\mathrm{sec}} + N^{exp2}_{2<\Delta\mathrm{T}<400\ \mu\mathrm{sec}}}{N^{exp1}_{0<\Delta\mathrm{T}<2000\ \mu\mathrm{sec}} + N^{exp2}_{0<\Delta\mathrm{T}<2000\ \mu\mathrm{sec}}} \tag{8.3}$$

, where $N^{exp1}_{2<\Delta\mathrm{T}<400\ \mu\mathrm{sec}}$ ($N^{exp2}_{2<\Delta\mathrm{T}<400\ \mu\mathrm{sec}}$) is the number of events with $2 < \Delta\mathrm{T} < 400$ μs for the first (second) exponential function and $N^{exp1}_{0<\Delta\mathrm{T}<2000\ \mu\mathrm{sec}}$ ($N^{exp2}_{0<\Delta\mathrm{T}<2000\ \mu\mathrm{sec}}$) is the number of total events estimated from the fitted mean values of capture times using the first (second) exponential function. The estimated efficiencies are given in Table 8.6.

Detector	Far	Near	Combined
Efficiency (%)	85.59 ± 0.17	85.14 ± 0.07	85.20 ± 0.06

Table 8.6: Efficiency of time coincidence requirement at FD and ND.

The efficiency difference of the time coincidence requirement is estimated to be 0.06% as an uncorrelated systematic uncertainty is estimated by the uncertainty of Gd concentration difference, ∼0.1%, between the near and far detectors. The difference of detection efficiency was confirmed by changing the Gd concentration using MC, and this was determined to be 0.06% as an uncorrected uncertainty. Table 8.7 summarizes the efficiency difference for Gd concentration.

Gd Concentration	Efficiency Difference
0.10989%	0.05%
0.11011%	0.06%

Table 8.7: Uncorrelated uncertainty of efficiency for the time coincidence requirement.

Spatial Coincidence

The distributions of spatial correlation ΔR are obtained from the n-H IBD samples as shown in Figure 8.4 A large accidental background is seen at FD. The efficiency of the spatial coincidence requirement, ΔR < 450 mm, is obtained from IBD signal enriched sample with $E_{prompt} > 4.5$ MeV assuming the efficiency 100% at ΔR < 2000 mm,

$$\varepsilon = \frac{N_{\triangle R<450\ mm}}{N_{\triangle R<2000\ mm}} \tag{8.4}$$

where $N_{\triangle R<450\ mm}$ is the number of events with ΔR < 450 mm and $N_{\triangle R<2000\ mm}$ is the number of events with ΔR < 2000 mm. The ΔR distributions of the IBD signal enriched samples are shown in Figure 8.5. The estimated efficiency is given in Table 8.8.

The correlated uncertainty is estimated as 0.05% based on changing the ΔR requirement by the resolution of reconstructed vertex, 0.3 m. The uncorrelated systematic uncertainty is estimated as 0.05% from the efficiency difference between the FD and ND.

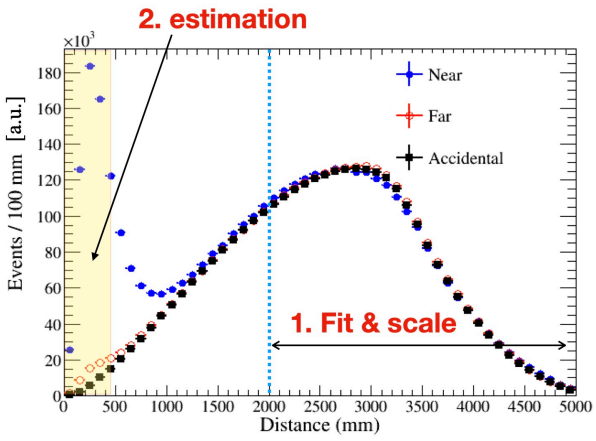

Figure 8.4: Distribution of spatial correlation ΔR obtained from the IBD samples at ND (blue solid circles) and FD (red open circles) without the spatial coincidence requirement. The black solid circles represent the random ΔR distribution obtained from the accidental background.

Detector	Far	Near	Combined
Efficiency (%)	70.29 ± 0.16	70.12 ± 0.05	70.19 ± 0.05

Table 8.8: Efficiency of spatial coincidence requirement at FD and ND.

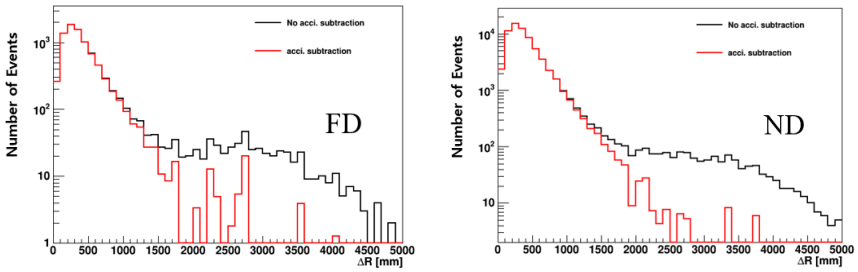

Figure 8.5: Distribution of spatial correlation ΔR after subtraction of accidental background with $E_{prompt} > 4.5$ MeV at FD and ND. The red histograms represent the ΔR distributions of the IBD signals after subtraction of the accidental distribution.

The uncorrelated uncertainty is estimated to be 0.05% from the efficiency difference between FD and ND.

$\mathbf{Q_{max}/Q_{tot}}$

The following Q_{max}/Q_{tot} < requirements are applied to the prompt and delayed candidates:

- Prompt: $Q_{max}/Q_{tot} < 0.07$
- Delayed: $Q_{max}/Q_{tot} < 0.06$

The efficiencies of the Q_{max}/Q_{tot} requirements are obtained using an IBD candidate sample of almost no accidental background events and $Q_{max}/Q_{tot} < 0.08$ that are selected by a stringent spatial correlation requirement of $\Delta R < 450$ mm and the high prompt energies of $E_{prompt} > 3.0$ MeV. The Q_{max}/Q_{tot} distribution of prompt events in this sample is shown in Figure 8.6 and predicts an expected IBD signal loss in the region of $Q_{max}/Q_{tot} > 0.07$, by extrapolating from the region of $Q_{max}/Q_{tot} < 0.07$ using an exponential distribution as expected by a MC simulation.

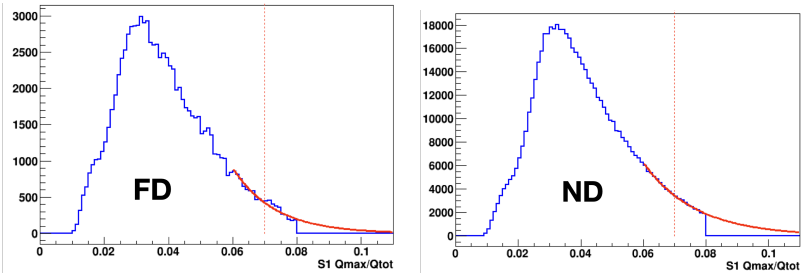

Figure 8.6: Q_{max}/Q_{tot} distribution of prompt events obtained from the IBD signal enriched sample. From these distributions of $Q_{max}/Q_{tot} < 0.08$, an expected IBD signal loss in the region of $Q_{max}/Q_{tot} > 0.07$ is estimated by extrapolating from the region of $Q_{max}/Q_{tot} < 0.07$ using an exponential distribution as expected by a MC simulation.

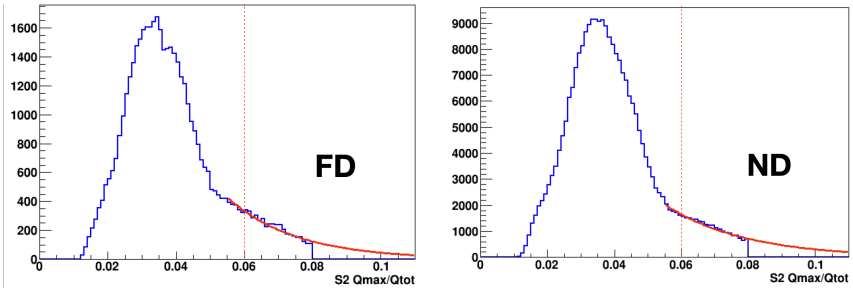

Figure 8.7: Q_{max}/Q_{tot} distribution of delayed events obtained from the IBD signal enriched sample. From these distributions of $Q_{max}/Q_{tot} < 0.08$, an expected IBD signal loss in the region of $Q_{max}/Q_{tot} > 0.06$ is estimated by extrapolating from the region of $Q_{max}/Q_{tot} < 0.06$ using an exponential distribution as expected by a MC simulation. A sudden change of the Q_{max}/Q_{tot} shape comes from the finite size of the γ-catcher.

The estimated efficiency of the Qmax/Qtot requirement is given in Table 8.9 and 8.10.

Detector	Far	Near	Combined
Efficiency (%)	91.93 ± 0.26	91.41 ± 0.08	91.45 ± 0.07

Table 8.9: Efficiency of the prompt Q_{max}/Q_{tot} requirement at FD and ND.

Detector	Far	Near	Combined
Efficiency (%)	86.58 ± 0.25	86.58 ± 0.10	86.58 ± 0.09

Table 8.10: Efficiency of the delayed Q_{max}/Q_{tot} requirement at FD and ND.

Based on comparison of the Q_{max}/Q_{tot} distribution between FD and ND, the Q_{max}/Q_{tot} difference is found to be 0.07% for prompt events and 0.09% for delayed events. Using these Q_{max}/Q_{tot} differences, the uncorrelated uncertainty of the efficiency is estimated to be 0.07% for the prompt Q_{max}/Q_{tot} requirement and 0.09% for the delayed Q_{max}/Q_{tot} requirement.

Cosmic and trigger time veto

Cosmic-induced backgrounds, including fast neutrons, are removed by the timing veto requirements with respect to the trigger and cosmic muon in Chapter 6. As

described in section 6.7, the total IBD signal loss due to all timing requirements at FD is $(21.18 \pm 0.01)\%$ for Set A and $(22.69 \pm 0.10)\%$ for Set B. while the one at ND is $(38.256 \pm 0.035)\%$ for Set A and $(43.056 \pm 0.033)\%$ for Set B. Therefore, the efficiency of the time veto is estimated to be $(77.31 \pm 0.10)\%$ for FD and $(57.75 \pm 0.035)\%$ for ND. The uncertainties are taken to be fully uncorrelated.

Total Detection Efficiency

The efficiencies and their uncorrelated uncertainties of IBD selection criteria are summarized in Table 8.11. The total detection efficiency is estimated to be 15.47 (FD) and 11.55 (ND)%, more than twice less than n-Gd due to tighter requirements. In addition, the uncorrelated uncertainty of detection efficiency is roughly three times larger than n-Gd. Therefore, the systematic error of the measured mixing angle value is larger than n-Gd accordingly.

	Efficiency (%)	Correlated	Uncorrelated
Acceptance and trigger	78.81	1.5	0.02
Neutron H capture fraction	63.61	0.42	0.04
Prompt energy ($1.2 < E < 8$ MeV)	97.83	0.10	0.08
Delayed energy ($2.2 \pm 2\sigma$)	86.16	0.10	0.08
S1 Q_{max}/Q_{tot}	91.45	0.50	0.07
S2 Q_{max}/Q_{tot}	86.58	0.16	0.09
Time coincidence	85.20	0.20	0.06
Spatial coincidence	70.18	0.17	0.05
Cosmic and trigger time veto	77.31(FD) 57.75(ND)		0.10(FD) 0.03(ND)
Target protons (3.299 ± 0.023)		0.70	
IBD cross section		0.09	
Combined	15.47 (FD) 11.55 (ND)	1.8 1.8	0.21 0.19

Table 8.11: Efficiencies of IBD selection requirements.

8.2 Reactor Related Uncertainty

The systematic uncertainties related to the reactor arise from several sources. The expected reactor neutrino flux depends on the baseline distance, fission fraction

of four major isotopes, mean energy released per fission, thermal power of the reactor, and the cross-section of the fission reaction. The main sources of the reactor-related uncertainties are thermal power of the reactor and fission fraction of the four isotopes. The positions of the two detectors and six reactors were surveyed using a global positioning system (GPS), and the baseline distances between the detectors and reactors were obtained with an accuracy less than 10 cm. The thermal powers of the reactors are measured in an indirect way at the secondary steam generator of the reactor with 0.5% uncertainty. The fission fraction uncertainties of the four isotopes are obtained from a pseudo experiment. The reactor antineutrino flux change due to the uncertainty of fission fraction, also obtained from a pseudo experiment, is 0.5%. The maximum change with the varying relative fission fraction is estimated to be 0.6%. The total uncorrelated systematic uncertainty arising from the fission fraction is estimated to be 0.7%. The systematic uncertainties related with the reactor are not associated with the difference between FD and ND. Even though their origin is from the reactor only, the systematic uncertainties related to the reactor are not canceled out by comparing FD and ND, because the flux contributions of each reactor are different at FD and ND due to the difference in baseline. The reactor-related systematic uncertainties of expected reactor antineutrino flux are summarized in Table 8.12. Further details on these uncertainties are described in section 3.4.

Parameter	Uncorrelated	Correlated
Baseline	0.03%	-
Thermal Power	0.5%	-
Fission fraction	0.7%	-
Fission reaction cross section	-	1.9%
Reference energy spectra	-	0.5%
Energy per fission	-	0.2%
Combined	0.9%	2.0%

Table 8.12: Reactor-related systematic uncertainties of expected reactor antineutrino flux.

8.3 Background Uncertainty

The background uncertainties are described in Chapter 7. The uncertainties are of two types: shape uncertainty (energy uncorrelated) and magnitude (energy correlated) uncertainty. They are summarized in Table 8.13. The uncertainty from the ^{9}Li/^{8}He background is dominant for almost entire energy region, except for lower energy region of $E_{prompt} < 2.0$ MeV where the accidental background

uncertainty is large. Maximum oscillation occurs at 1.0 < Eprompt < 2.0 MeV and thus further reduction of the accidental background uncertainty is needed to make the rate and shape analysis possible.

8.4 Summary of Systematic Uncertainty

All uncorrelated systematic uncertainties used to measure θ_{13} and $|\Delta m^2_{ee}|$ are summarized in Table 8.13. Correlated uncertainties are canceled out using the far-to-near ratio method. The background uncertainties are given by fractional errors of the measured background magnitudes.

Uncertainty source		Uncorrelated
Reactor		0.9%
Detection efficiency		0.18%
$\|\Delta m^2_{ee}\|$		0.01%
	Rate (/day)	error(/day)
Total background	2.23 (far)	0.21
	17.89 (near)	0.42
Accidental	18.64 (far)	0.01
	10.63 (near)	0.01
Fast Neutron	0.82 (far)	0.13
	3.04 (near)	0.10
^{9}Li/^{8}He	1.49 (far)	0.18
	5.95 (near)	0.41
^{252}Cf contamination	0.100(far)	0.018

Table 8.13: Summary of systematic uncertainties for this measurement. The uncertainties of reactor-related parts and detection efficiency are canceled out in this far-to-near ratio measurement.

Chapter 9

Results of θ_{13} Determination

This smallest neutrino mixing angle θ_{13} measurement is based on the far-to-near ratio and rate-only analysis. In this Chapter, we describe an algorithm to extract the θ_{13} value from the oscillation amplitude based on minimizing a χ^2.

9.1 Observed IBD Rates

The observed rates of IBD candidates after all of the selection requirements are presented in Chapter 6. The remaining background rates in the final samples are estimated as described in Chapter 7. The observed IBD rates and estimated background rates are summarized in Table 9.1. The observed daily rates of IBD candidates after subtracting backgrounds in the near and far detectors are shown in Figure. 9.1. The rates are sometime low when the reactors were turned off for fuel replacement and maintenance. The expected rates assuming no oscillations are shown for comparison. The observed IBD rate in the far detector is clearly lower than the expected one, indicating reactor $\overline{\nu}_e$ disappearance. The expected rates with the best-fit parameters of neutrino oscillation are also shown and agree well with the observed IBD rates.

Data Set A : before ^{252}Cf contamination		
Detector	Near	Far
Number of selected events	174524	27469
Total Background Rate (per day)	17.78 ± 0.70	23.97 ± 0.35
IBD rate after background subtraction	440.86 ± 1.30	21.82 ± 0.02
DAQ live time (days)	379.66	384.47
Accidental rate	7.95 ± 0.01	21.82 ± 0.02
^{9}Li/^{8}He rate	5.91 ± 0.61	1.42 ± 0.30
Fast neutron rate	3.92 ± 0.33	0.73 ± 0.18

Data Set B : after ^{252}Cf contamination		
Detector	Near	Far
Number of selected events	540936	134643
Total Background Rate (per day)	17.41 ± 0.43	25.41 ± 0.22
IBD rate after background subtraction	270.38 ± 0.58	33.94 ± 0.27
DAQ live time (days)	1879.635	2268.824
Accidental rate	8.79 ± 0.01	22.77 ± 0.01
^{9}Li/^{8}He rate	5.38 ± 0.40	1.62 ± 0.20
Fast neutron rate	3.24 ± 0.14	0.85 ± 0.08
^{252}Cf rate		0.10 ± 0.018

Data Set A + B : total period		
Detector	Near	Far
Number of selected events	715460	162112
Total Background Rate (per day)	17.89 ± 0.42	25.45 ± 0.21
IBD rate after background subtraction	298.78 ± 0.63	35.64 ± 0.30
DAQ live time (days)	2259.288	2653.297
Accidental rate	10.63 ± 0.01	18.64 ± 0.01
^{9}Li/^{8}He rate	5.95 ± 0.41	1.49 ± 0.18
Fast neutron rate	3.04 ± 0.10	0.82 ± 0.13
^{252}Cf rate		0.100 ± 0.018

Table 9.1: Event rate of the observed IBD candidates and the measured background at $1.2 < E_{prompt} < 8.0$ MeV. These rates are given in per day.

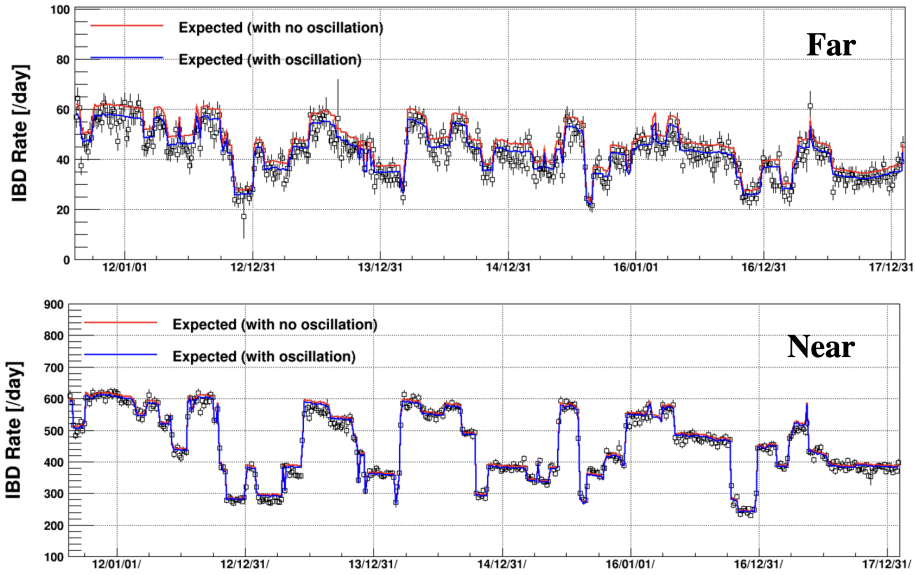

Figure 9.1: Measured daily rates of reactor $\overline{\nu}_e$ after subtracting backgrounds in FD and ND as a function of date (top plot for FD and bottom plot for ND). The blue curves are the expected rates for no oscillation. The red curves are the expected rates with the best-fit parameters and agree well with the measured ones.

9.2 Observed IBD Prompt Spectrum

The energy spectra of the observed IBD prompt events after background subtraction are shown in Figure. 9.2 which shows a shape comparison with the prediction from a reactor $\overline{\nu}_e$ model [72, 73] and the best-fit oscillation results. The fractional difference between data and prediction is also shown in the lower panel. A clear discrepancy is observed in the region of 5 MeV in both detectors. To compare the spectral shape, the MC predicted spectrum is normalized to the observed spectrum in regions excluding $3.6 < \mathrm{E_{prompt}} < 6.6$ MeV. The excess of events is estimated at approximately 2.5% of the total observed IBD events in both detectors. Furthermore, the 5-MeV excess is observed to be proportional to the reactor thermal power where the rate is calculated from the events in excess in the $3.6 < \mathrm{E_{prompt}} < 6.6$ MeV region relative to the nominal model prediction [72, 73].

9.3 Determination of θ_{13} using Far-to-Near Ratio

In the rate-only analysis, the oscillation amplitude of neutrino survival probability is extracted from information on the observed reactor $\overline{\nu}_e$ rates only, without using the prompt energy spectra. We observe a clear deficit of reactor $\overline{\nu}_e$ in the far detector. Even with the unexpected structure around 5 MeV, the oscillation amplitude can be determined from a fit to the measured far-to-near ratio of IBD prompt spectra. The determination is not affected by the presence of the 5 MeV excess because of its cancellation in the ratio measurement. Using the deficit information and a χ^2 fit, a rate-only analysis obtains the value of $\sin^2 2\theta_{13}$ as 0.086 ± 0.006 (stat.) $\pm$ 0.0010 (syst.), where the world average value of $|\Delta m^2_{ee}| = (2.502 \pm 0.06) \times 10^{-3}$ eV^2 is used [22]. The systematic error of $\sin^2 2\theta_{13}$ is reduced from 0.014 to 0.010, mainly due to the reduced uncertainties of backgrounds and detection efficiencies relative to the 1500 days result [64]. Note that the main reduction in the uncertainty comes from more precise determination of ^{9}Li/^{8}He background spectrum and detection efficiencies with more statistics of control samples.

9.3.1 χ^2 Fit to Far-to-Near Ratio

For determination of θ_{13}, a χ^2 with pull parameter terms [74] of systematic uncertainties is constructed using the rate ratio measurement and is minimized by varying the oscillation parameters and pull parameters. The following χ^2 is used

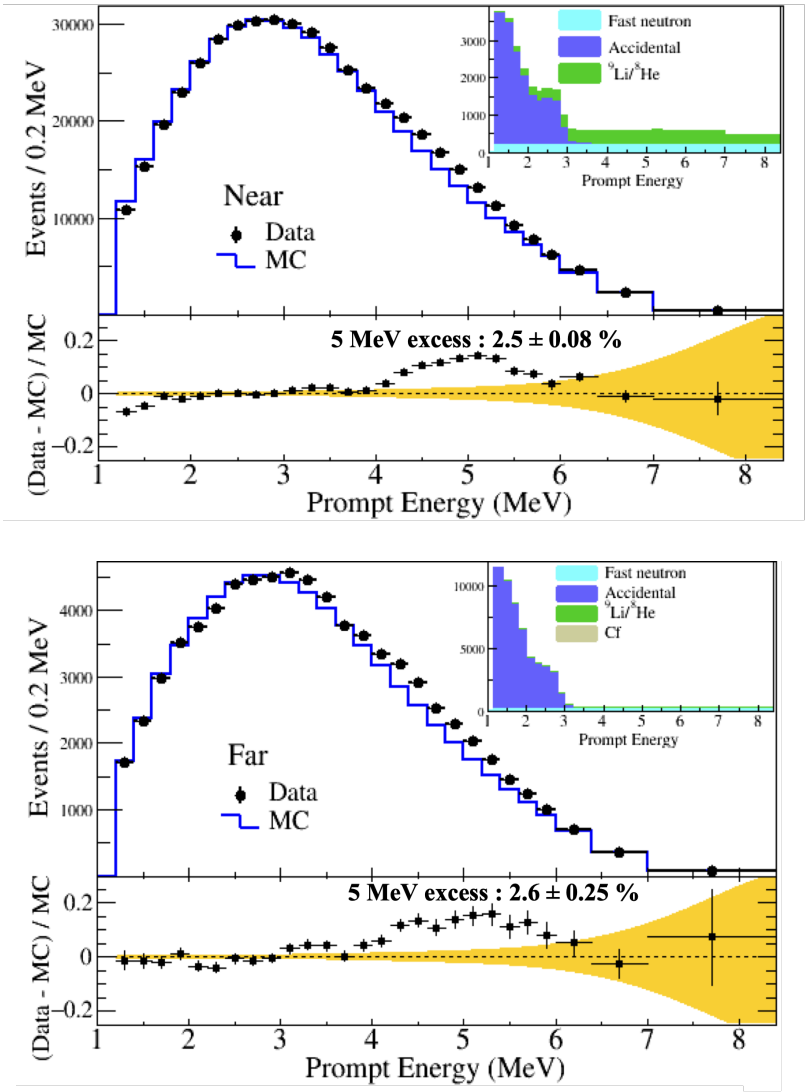

Figure 9.2: Spectral shape comparison of observed and expected IBD prompt events in ND and FD. The observed spectra are obtained by subtracting the remaining background spectra, as shown in the right upside insets. The expected spectrum is obtained from the best-fit oscillation results that are applied to the no oscillation MC spectra. The expected spectra are normalized to data spectra in the regions excluding $3.6 < E_{prompt} < 6.6$ MeV. The discrepancy between data and MC prediction is clearly seen at 4∼6 MeV. The observed excess is correlated with the reactor power and corresponds to 2.5% of the total number of IBD events. The deviation from the expectation is larger than the uncertainty of the expected spectrum (shaded band).

for this rate-only analysis,

$$\chi^2 = \sum_{P=SetA,SetB} \left\{ \frac{\frac{N_{obs}^{F,P}}{N_{obs}^{N,P}} - \frac{N_{exp}^{F,P}}{N_{exp}^{N,P}}}{U^P} \right\}^2 + \chi^2_{pull} \tag{9.1}$$

where

$$N_{exp}^{F,P} = \sum_{r=1}^{6} \left[\left(1 + \xi + \xi_F^{SetB} + f_r\right) \cdot N_{exp}^{F,P,r} \right] - b_F^P \tag{9.2}$$

$$N_{exp}^{N,P} = \sum_{r=1}^{6} \left[\left(1 + \xi_N^{SetB} + f_r\right) \cdot N_{exp}^{N,P,r} \right] - b_N^P \tag{9.3}$$

$$U^P = \frac{N_{obs}^{F,P}}{N_{obs}^{N,P}} \sqrt{\frac{N_{obs}^{F,P} + N_{bkg}^{F,P}}{\left(N_{obs}^{F,P}\right)^2} + \frac{N_{obs}^{N,P} + N_{bkg}^{N,P}}{\left(N_{obs}^{N,P}\right)^2}} \tag{9.4}$$

and

$$\begin{aligned} \chi^2_{pull} &= \left(\frac{\xi}{\sigma_\xi}\right)^2 + \sum_{d=F,N} \left(\frac{\xi_d^{SetB}}{\sigma_{\xi_d}}\right)^2 \\ &\quad + \sum_{r=1}^{6} \left(\frac{f_r}{\sigma_{f_r}}\right)^2 + \sum_{P,d} \left(\frac{b_d^P}{\sigma_{b_d}^P}\right)^2 \end{aligned} \tag{9.5}$$

The parameters in the χ^2 are defined as follows.

- $N_{obs}^{d,P}$: Number of background subtracted IBD, d = detector (far, near), P = data set (Set A, Set B)
- $N_{exp}^{d,P}$: Number of expected IBD, d = detector (far, near), P = data set (Set A, Set B)
- $N_{bkg}^{d,P}$: Number of total background, d = detector (far, near), P = data set (Set A, Set B)
- ξ : Pull parameter of detection efficiency
- σ_ξ : Uncertainty of detection efficiency
- ξ_d^{setB} : Pull parameter of uncommon detection efficiency for data set B only, d = detector (far, near).

- σ_{ξ_d} : Uncertainty of uncommon detection efficiency for data set B only, d = detector (far, near).

- f_r : Pull parameter for the reactor Thermal power and isotope fraction for reactor (r = $1 \sim 6$)

- σ_{f_r} : Uncertainty of the neutrino flux from thermal power for reactor (r = $1 \sim 6$)

- b_d^p : Pull parameter for the accidental, fast neutron, magnitude part of ^{9}Li/^{8}He and ^{252}Cf background, d = detector (far, near), P = data set (Set A, Set B)

- $\sigma_{b_d^p}$: Combined uncertainty for the accidental, fast neutron, magnitude uncertainty of ^{9}Li/^{8}He and ^{252}Cf background, d = detector (far, near), P = data set (Set A, Set B)

The χ^2 values are given separately for two data sets A and B because of the different IBD selection criteria, including the ^{252}Cf background removal requirement for data set B, and thus their different detection efficiencies. Due to the identical detectors, the common detection uncertainty is canceled out and the only difference of detection efficiency uncertainty between them is considered in the one of detectors. The reactor-related pull parameters have a reactor index only and are common to both detectors. The background uncertainties except for the ^{9}Li/^{8}He background are taken into account differently between data sets A and B. The only ^{9}Li/^{8}He spectral shape uncertainty is common to both detectors and data sets A and B because a common ^{9}Li/^{8}He spectrum is used to estimate the remaining background rate for both data sets A and B as well as for both detectors.

9.3.2 Fit Results

The best-fit value obtained from the rate-only analysis is

$$\sin^2(2\theta_{13}) = 0.0864 \pm 0.006 \text{ (stat.)} \pm 0.010 \text{ (syst.)}.$$

The 1σ error of the best-fit value is determined by the fit parameter values at $\Delta\chi^2$ equal to its minimum + 1. With all of pull parameters off, the only statistical error can be obtained and the systematic error is in turn obtained based on the following relationship,

$$\delta^2_{\text{syst.}} = \delta^2_{\text{total}} - \delta^2_{\text{stat.}} \tag{9.6}$$

, where $\delta_{\text{syst.}}$ is the systematic error, δ_{total} is total error, and $\delta_{\text{stat.}}$ is the statistical error. Figures 9.3 and 9.4 show $\Delta\chi^2$ distributions to evaluate the statistical and total errors, respectively. The breakdown systematic errors for individual uncertainty sources are given in Table 9.2. The dominant systematic error for this n-H analysis is due to the uncertainties of detection efficiency and remaining background.

Uncertainty Sources	Systematic error
Reactor	0.003
Detection Efficiency	0.008
Backgrounds	0.006
Δm^2_{ee}	0.001
Combined	0.010

Table 9.2: Systematic errors from various uncertainty sources. The dominant sources of the total systematic error are the uncertainties of detection efficiency and remaining backgrounds.

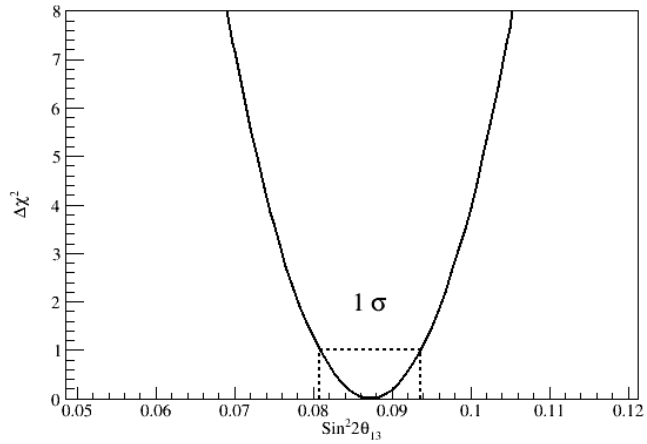

Figure 9.3: Distribution of $\Delta\chi^2$ for evaluating the statistical error only with all of full parameters turned off. The 1 σ value contains only statistic uncertainty.

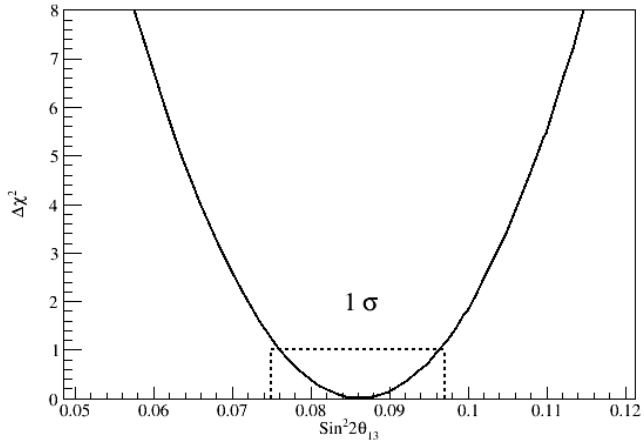

Figure 9.4: Distribution of $\Delta\chi^2$ for evaluating the total error of $\sin^2(2\theta_{13})$ value. The total error is obtained as 0.011.

Chapter 10

Summary and Discussion

Using approximately 2,900 days of data, RENO has observed a clear disappearance of reactor $\overline{\nu}_e$ with two identical detectors to measure a more precise value of theta13, $\sin^2(2\theta_{13}) = 0.086 \pm 0.006$ (stat.) $\pm$ 0.0010 (syst.), based on rate-only analysis. The systematic error of $\sin^2(2\theta_{13})$ has been significantly reduced from 0.014 [64] to 0.010 due to the reduced uncertainties of the ^{9}Li/^{8}He background and the detection efficiency. The statistical error is also reduced from 0.008 [64] to 0.006 due to more data. Figure 10.1 shows comparison of $\Delta\chi^2$ distribution between this measurement and the previous 1,500 days result [64], indicating the improved precision of $\sin^2(2\theta_{13})$ value from 0.016 to 0.011.

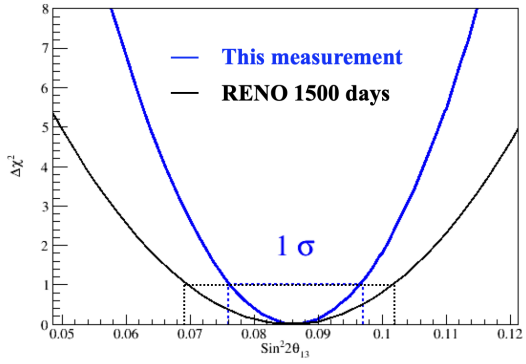

Figure 10.1: Comparison of $\Delta\chi^2$ distribution between this measurement and the previous RENO result [64]. The total error of the $\sin^2 2\theta_{13}$ value is 0.011 for this measurement, improved from 0.016 of the previous error.

Table 10.1 shows the systematic error contributions of $\sin^2(2\theta_{13})$ from various sources. The systematic error of $\sin^2(2\theta_{13})$ is larger than the statistical error of 0.006, and thus must be reduced for further improved measurement of $\sin^2(2\theta_{13})$. The reactor-related systematic uncertainty makes the smallest contribution to the systematic error, and it is difficult to be reduced. On the other hand, the detection efficiency and background uncertainties could be reduced by more statistics on control samples and by better understanding of them. Further reduction of accidental background in the FD data is essential for a rate and spectral analysis to measure the oscillation frequency.

Uncertainty Sources	Systematic Error
Reactor	0.003
Detection efficiency	0.008
Backgrounds	0.006
Total	0.010

Table 10.1: Systematic errors from various uncertainty sources. The dominant sources of the total systematic error are the uncertainties of detection efficiency and remaining backgrounds.

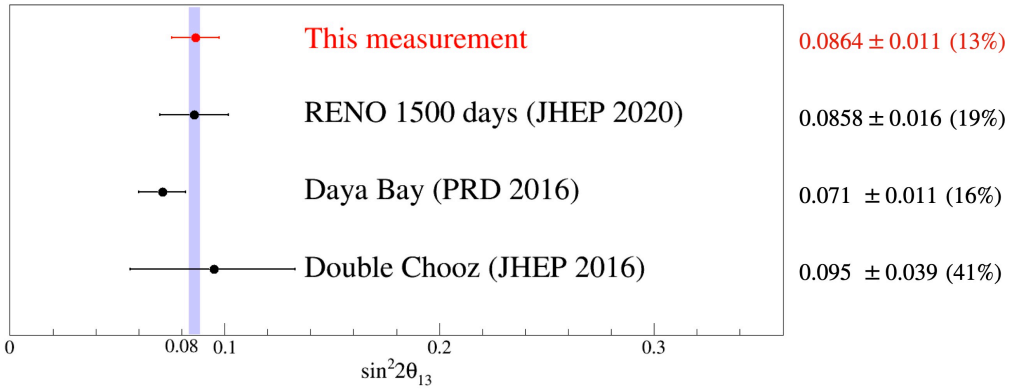

Figure 10.2: Comparison of experimental results on $\sin^2 2\theta_{13}$. The purple shade band comes from the world average value [22], others are experimental results of RENO [64], Daya Bay [75], and Double Chooz [76] are used.

A clear IBD spectral difference from the current reactor $\overline{\nu}_e$ model is observed in the region of 5 MeV in both detectors, with an excess corresponding to about 2.5% of the total observed IBD events. The observed excess is clearly correlated

with the reactor thermal power, indicating the excess arises from the reactor $\overline{\nu}_e$. The observed reactor $\overline{\nu}_e$ rate only is used to extract the oscillation amplitude of neutrino survival probability. We observed a clear deficit in the observed rate, 6.8% for the far detector and 1.1% for the near detector with respect to the expected one, indicating a definitive observation of reactor antineutrino disappearance consistent with neutrino oscillation. Using the deficit information, the obtained best-fit value is $\sin^2(2\theta_{13}) = 0.0864 \pm 0.006$ (stat.) $\pm$ 0.0010 (syst.) where the world average value of $|\Delta m^2_{ee}| = (2.502 \times 10^{-3}$ eV$^2)$ is used. This value is consistent with the previous measurement of n-Gd result, $\sin^2(2\theta_{13}) = 0.0864 \pm 0.0048$ (stat.)within their uncertainties, while the systematic uncertainty is about twice larger than that of the n-Gd result. The error fraction of $\sin^2(2\theta_{13})$ for each uncertainty source is obtained using the pull terms of the χ^2 equation and are summarized in Table 10.1. The systematic uncertainties of detection efficiency and backgrounds mostly contribute to the systematic error of 1.5 times larger than the statistical error. Furthermore, we obtain a ratio of $\sin^2 2\theta_{13}$ between the n-H and n-Gd measurements.

$$\left(\frac{\mathrm{n-H}}{\mathrm{n-Gd}}\right)_{\sin^2(2\theta_{13})} = \frac{0.0864 \pm 0.011\ (tot.)}{0.0896 \pm 0.007\ (tot.)} = 0.964 \pm 0.123\ (tot.), \quad (10.1)$$

where the error is obtained by excluding the correlated uncertainties. This demonstrates good consistency between the n-H and n-Gd measurements while their various uncertainties are independent. Figure 10.3 shows the background subtracted, observed IBD prompt energy spectrum at the far detector compared to the one expected with no oscillation and the one with the best-fit oscillation parameters at the far detector.

In Summary, RENO has performed an independent measurement of $\sin^2 2\theta_{13}$ via neutron capture on hydrogen using 2900 days of data, providing a result consistent with the n-Gd analysis. The measured value is compared with those of Daya Bay and Double Chooz experiments and found to be consistent with their errors, as shown in Figure 10.2. Future improvement of the systematic uncertainties will allow the determination of oscillation amplitude and frequency by spectral analysis, even using the n-H data sample. More precise measurements of $\sin^2 2\theta_{13}$ are necessary for constraining the leptonic CP phase if combined with the experimental results using accelerator neutrino beams. Independent IBD n-H measurements would provide additional information on the precise value of $\sin^2 2\theta_{13}$ as well as cross-check.

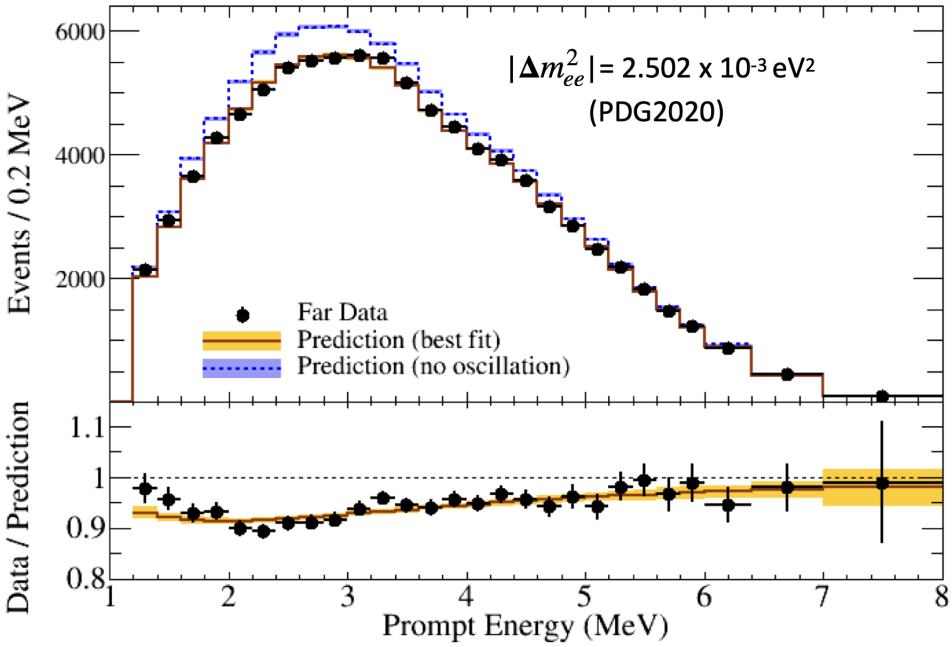

Figure 10.3: Comparison of the observed IBD prompt spectra with dots and no-oscillation predicted spectra with the blue shaded histogram in the FD on the top side of the plot. The no-oscillation prediction is obtained from the measurement in ND. The prediction from the best-fit oscillation amplitude is also shown as a yellow-shaded histogram. The ratio of observed spectrum in FD to the no-oscillation prediction with dots points on the bottom side of plot and the ratio from the MC simulation with the best-fit results folded in (yellow band). Errors include statistical and background subtraction uncertainties.

Appendix A

Development of the flasher PMT requirements

The exact cause for PMT flashing is unknown, but the most likely cause known so far is known to occur as a flashing event on the detector, as electric charges are momentarily released due to a voltage drop in the capacitor at the PMT base. This phenomenon has been reported not only in the RENO experiment but also in SK (Japan), Daya Bay (China), and Double Chooz (France), which are experiments using multiple PMTs. We are working hard so that there is no setback in data analysis by developing and removing them. The event generated in the detector is transmitted as an electrical signal by striking a number of photons simultaneously with multiple PMTs, and the flasher event occurs irregularly independently of the event time in each PMT. As described in Chapter 6., We applied Q_{max}/Q_{tot} (-400 $\sim$ 800 ns) $<$ 0.08 requirement for flasher PMT events as default method. To remove flasher PMT events more precisely, we developed more variables for flasher removal. "qmaxpmt" is the single PMT with the highest charge in one event. If the event is a flasher event, the probability that flashing occurred in "qmaxpmt" is high. "hs_qmaxqtot" is the ratio of the total charge of one event and the highest charge among the individual PMTs of one event with the same meaning as Q_{max}/Q_{tot}. In the case of a flasher event, the "hs_qmaxqtot" value is larger (almost the value is 1). As shown in Figure A.1, "hs_r" is the average charge of PMTs around "qmaxpmt" divided by "qmax" that "qmaxpmt" has, as same meaning with Q_{loc}. This is because the charge occurs only in and near "qmaxpmt" , and there is not much charge in the vicinity, so the distribution of the charge is expressed as the radius (about 80cm). Because signal events are evenly hit, "hs_qmaxqtot" is small, and "hs_r" is large, whereas flasher events mainly appear on the side where the value of "hs_qmaxqtot" is large and "hs_r" is small. When the "hs_qmaxqtot : hs_r" 2D figure is drawn in the part where most

flasher events are irregular and that a specific PMT has a high instantaneous charge, it can be seen that hotspots appear in the range of 0∼0.3 for "hs_r" and 0.05∼0.08 for "hs_qmaxqtot" .

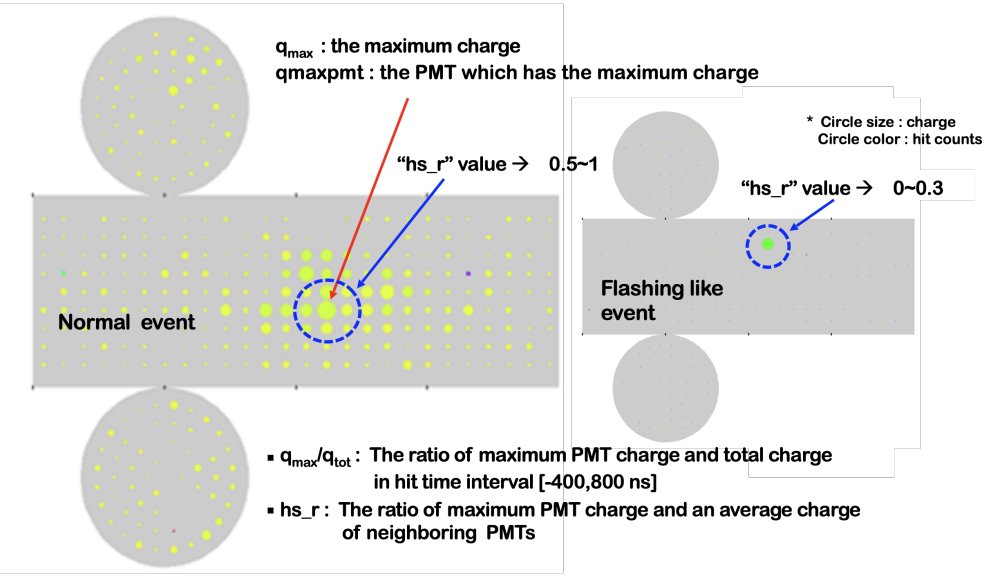

Figure A.1: "Event display" of RENO DAQ program in real-time screen capture image. The left is for a normal event, and the right is for a flashing-like event. Circle size represents the charge of each PMT, and circle color represents the hit counts in an event time window. The blue dot line shows the radius for calculating the average charge around "qmaxpmt " for "hs_r " variable.

A.1 Default method for finding flasher PMT events

Flasher events usually show high Q_{max}/Q_{tot} and low Q_{loc}/Q_{max}. Using these features, as shown in Figure A.2, the highly flashing Q_{max}PMT can be found by using Q_{max}/Q_{tot} and Q_{loc}/Q_{max}. There seems to be no particular hotspot for all the events on the top-left plot. However, in the red box of the top-right plot, there is a specific hotspot. For more efficient removal, we also checked single event rates and investigated highly rated regions (red dotted line on the bottom-left plot). As a result, we also find the abnormal hotspot on the bottom-right plot.

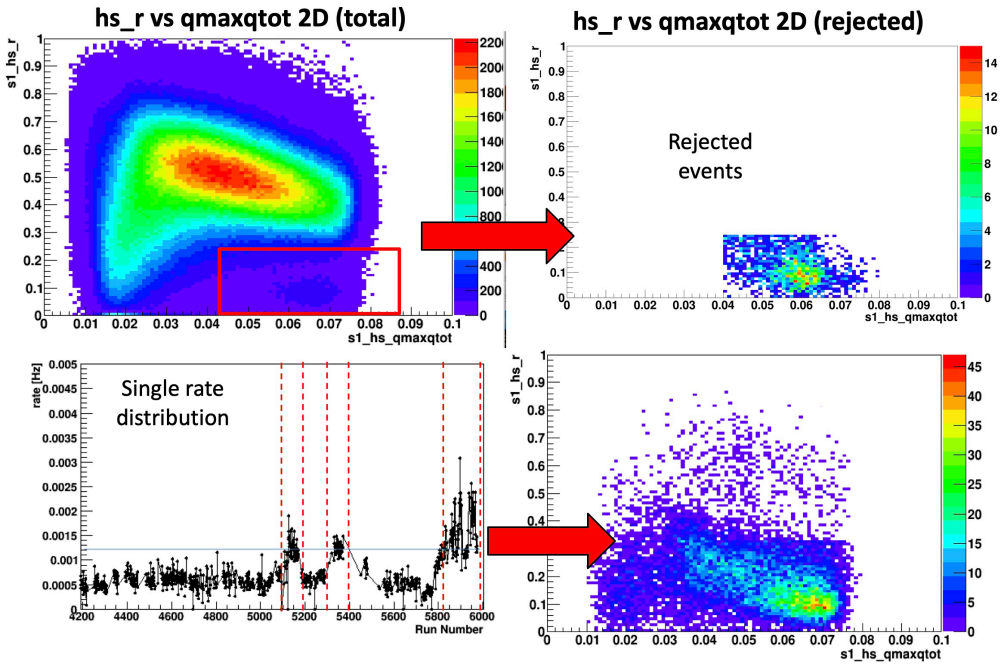

Figure A.2: Default method for finding flasher PMT events using a condition on Q_{max}/Q_{tot} and Q_{loc}/Q_{max}. In the red box, as a hotspot, highly flashing Q_{max}PMT can be found easily.

A.2 Development to find simply flashing PMT

In the previous default flasher cut, hs_r, hs_qmaxqtot, and hs_qmaxpmt were used to find and remove flasher hotspots far away from the signal. The flasher can be removed like this, but it has the disadvantage that the process is too complicated. Therefore, as a new flasher removal method, the single events rate method is a method to remove the flasher by simply examining all PMTs. When a flasher event occurs, the new method is to investigate all the event rates of all PMTs, and it is possible to remove the undiscovered flasher. At this time, since many flasher events have already been removed through pairing in the IBD candidate, and it is difficult to check the event rate for each pmt, the qmaxpmt rate of single events before pairing is examined. Investigate the event rate of all 354 ID qmaxpmts, inspect hs_r and hs_qmaxqtot in the period of high rate, and make and apply a flasher cut. Using this method, it takes time and effort to examine all PMTs, but it can be said to be a general flasher removal method because it is much simpler and clearer than the default method. At the same time, it

is a more effective method than the default method because it can remove more flasher events that were not found in the default method. As shown in Figure A.3, we investigate every single event rate of all PMTs with 3 groups of different energy ranges, the prompt (S1) energy is 0∼3.5, 1.8∼2.4, 3.5∼12 MeV, respectively. The delayed (S2) energy is 1.8∼3 MeV in common.

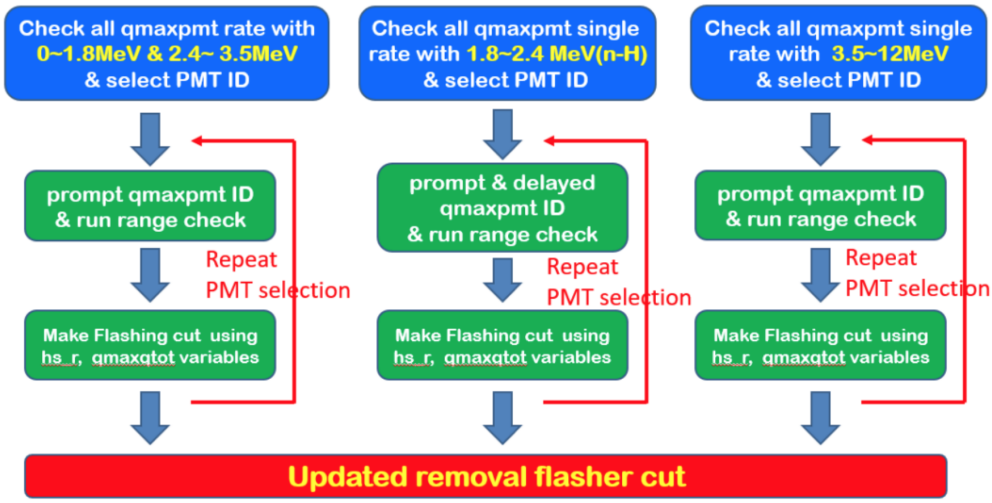

Figure A.3: Block diagram for updated flasher removal. To be more effective and more precise, we check every single event rate of all PMTs with 3 groups of different energy ranges

In the data processing, we applied the primary and secondary flasher removal process. The primary removal is for the vertex & charge correction process. After IBD pairing, the IBD candidate events can be obtained by applying Secondary Cut. As a result, accurate data selection can be obtained through processes such as background measurement and dead time. If either of the two is not applied properly, we cannot estimate a proper θ_{13} value.

A.3 Primary flasher removal

Basically, in the single event of RENO data without any requirement process, various trigger cuts to measure IBD paring events and data processing for selection criteria for IBD events are performed. At this time, charge and spatial correction work for the stability performance of the detector is preceded. The primary flasher exists as a hotspot event before these correction operations, so

the correction factor cannot be obtained. The single event rate of a relatively high peak in a specific period can be confirmed through the rate of single events at the primary level, as shown in Figure A.4. As a condition for flasher removal, hs_r : hs_qmaxqtot in the 2D figure, a hotspot in an area separated from the signal should be selected. In this case, it is difficult to set the removal condition. Therefore, the removal condition at the primary level roughly chooses the removal condition through a single event rate and performs the removal operation as shown in Figure A.5.

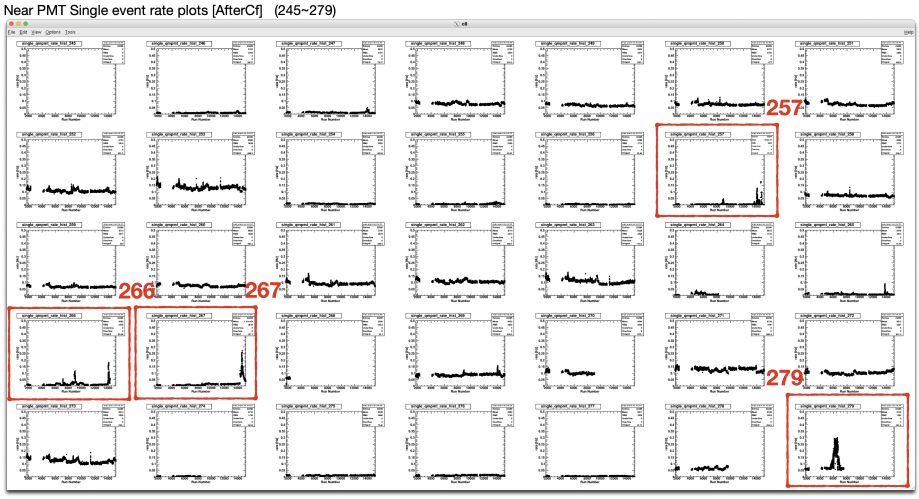

Figure A.4: Single event check of all PMTs sample image. There are 4 highly rated PMTs. The number 257, 266, 267, and 279 is the individual PMT identification number. The X-axis corresponds to the run number of data, and the Y-axis is the single event rate (Hz) of Each plot.

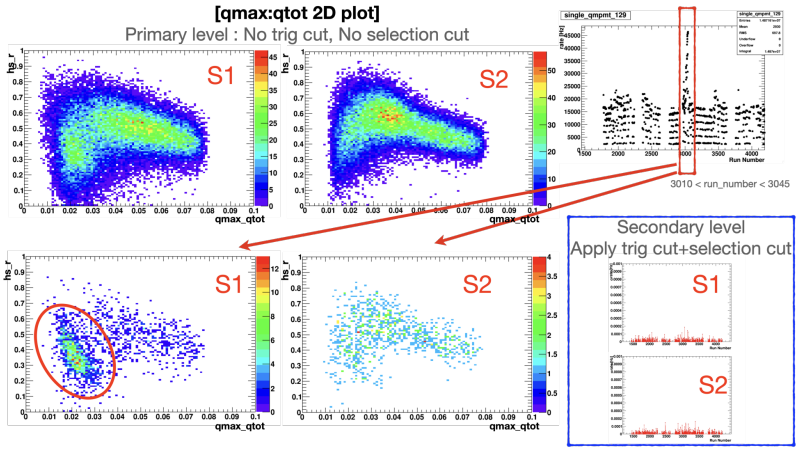

Figure A.5: Primary flasher removal sample for a 129^{th} PMT in FD. The high rate region, as the red box on the top-right side of the plot, indicates flasher events. The default method can not find flasher events because of no hotspot in the top-left and top-middle side plots.

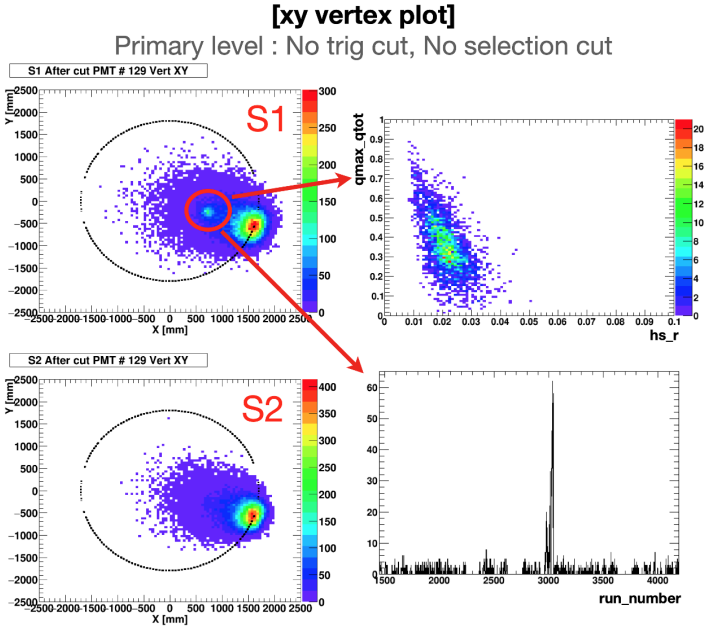

Figure A.6: Primary flasher removal sample using X-Y vertex variables. There is a hotspot in the X-Y 2D plot of prompt events (S1)

Also, when drawing a 2D vertex plot from the same data by cross-checking as shown in Figure A.6. and selecting for removal as a vertex area, we can set the removal conditions more clearly. The removal condition can be chosen as the period showing a high peak in the same single event rate.

A.3.1 Primary flasher removal condition

As mentioned before, when we check every single event rate, we can easily find the flasher event. However, it is quite difficult to set the conditions to remove it.

In order to set the condition to remove only the flasher event, it is necessary to find out an efficient removal method. We find 4 types of flashers by adding the vertex variable. The removal conditions are according to these 4 types as shown in Figures A.7, A.8, A.9, A.10.

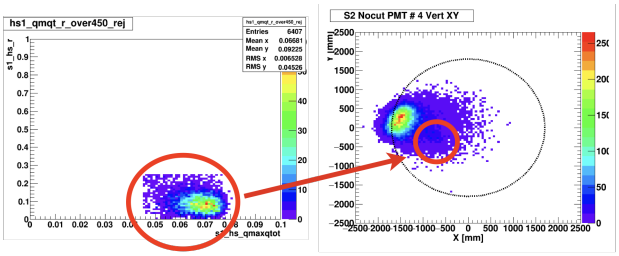

Flasher type 1 : cut using Flasehr variable (hs_r , hs_qmaxqtot)

Figure A.7: Primary flasher removal type 1. The default type is using hs_r and hs_qmaxqtot variables.

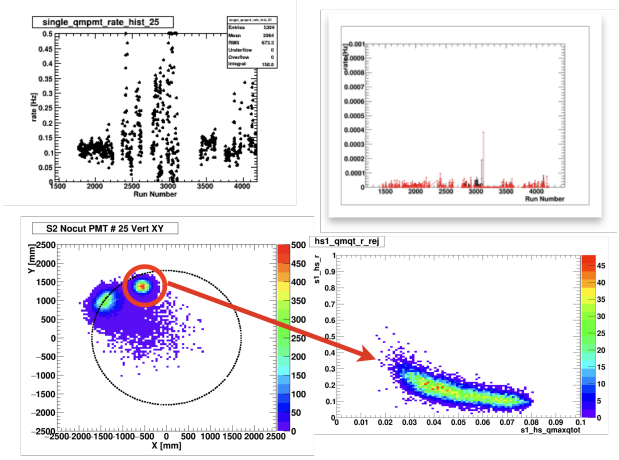

Flasher type 2 : cut using hs_r, hs_qmaxqtot + vertex variable

Figure A.8: Primary flasher removal type 2. Using hs_r and hs_qmaxqtot and additional vertex variables.

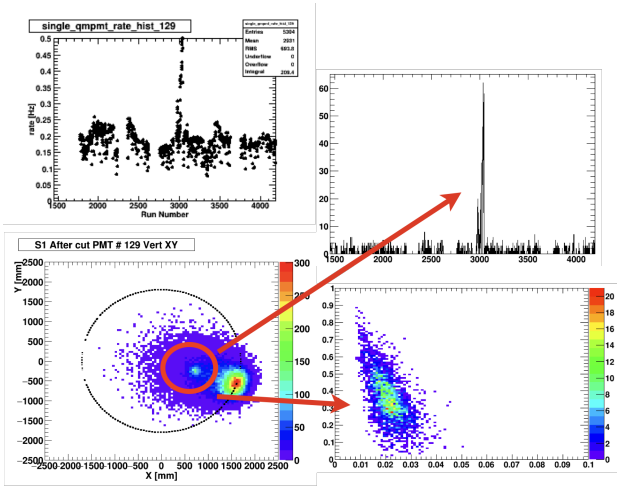

Flasher type 3 : cut using Vertex variable

Figure A.9: Primary flasher removal type 3. Using only vertex variables of each PMT.

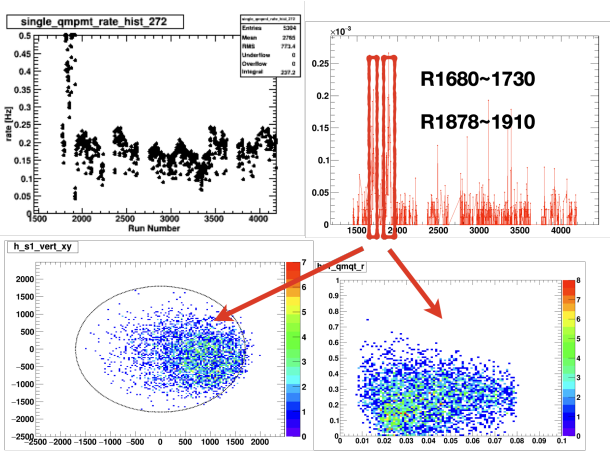

Figure A.10: Primary flasher removal type 4. There are no available variables for efficient removal. There is only one condition for removal using the number of data and PMT corresponding to the high rated

A.4 Secondary flasher removal

The primary flasher removal is only for the accurate vertex correction process and does not actually affect the estimation when we proceed with the IBD pairing process after vertex correction. Secondary flasher removal is applied to IBD data that has been paired for analysis, and the characteristics of the flasher greatly affect the accidental background. Thus, we set the removal condition with ΔR 450 mm value to separate IBD candidates and accidental backgrounds.

2D distribution and prompt spectrum of the events removed by the updated flasher removal from the short-distance data. It is shown to remove the flasher hotspot away from the signal in the 2d distribution as shown in Figure A.11. It can be seen that when applied to the entire energy region as well as the IBD event energy region, many events are generated in the low energy side corresponding to the flasher event. In addition, if you look at the number of removed flashers highlighted in red in the organized table, more than 1350 have been removed compared to the existing cut, and the deadtime is also small, so it can be confirmed that it is very effectively removed. Figure A.12 shows the distribution of vertices removed by the updated flasher removal cut, and it can be seen that flasher events appear at specific hotspots in the vertices as well.

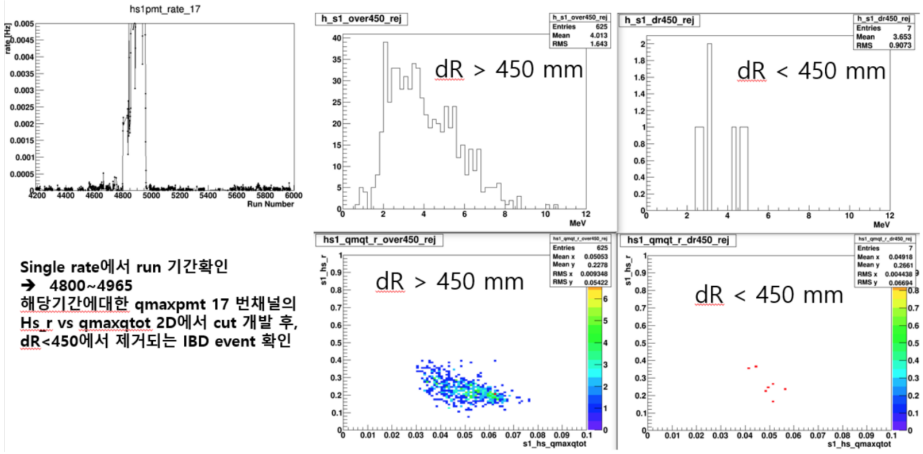

Figure A.11: Secondary flasher removal. For more efficient removal, The data group is divided by ΔR 450 mm.

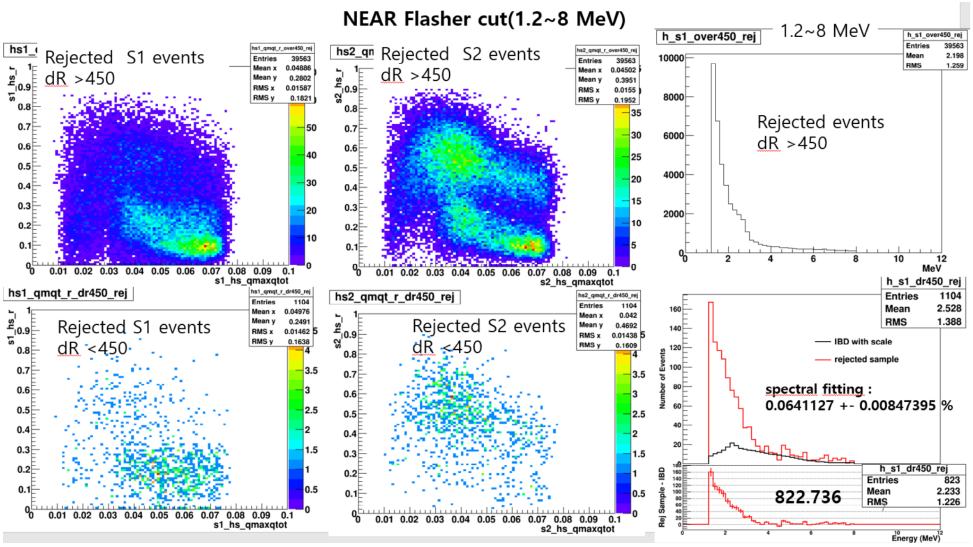

Figure A.12: Secondary flasher removal. For more efficient removal, The data group is divided by ΔR 450 mm.

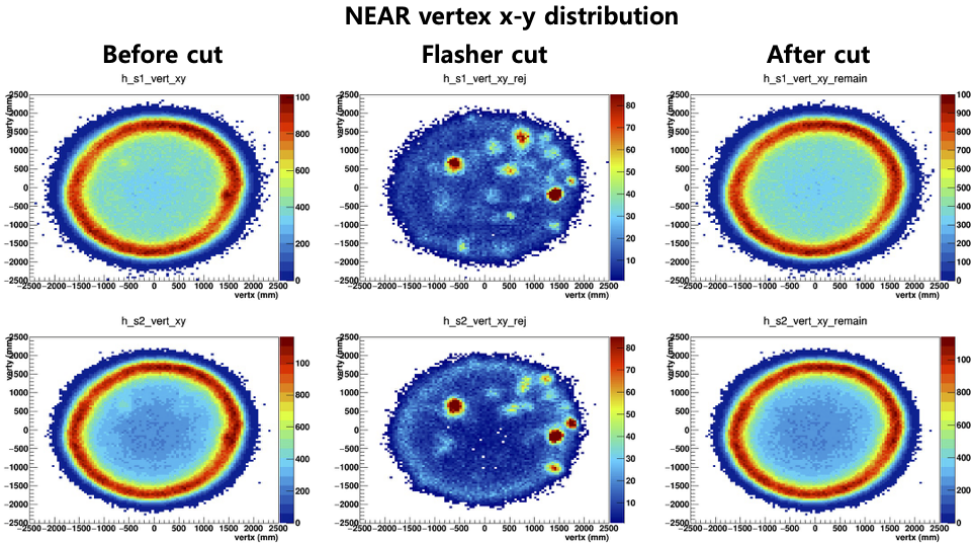

Figure A.13: Final flasher removal check with X-Y axes

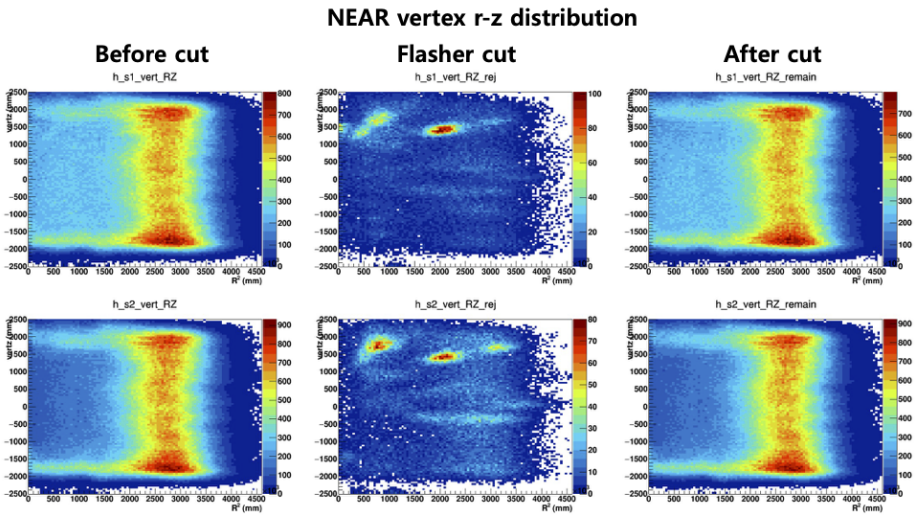

Figure A.14: Final flasher removal check with r-z axes.

Bibliography

[1] B. Pontecorvo, Sov. Phys. JETP **7** (1958) 172.

[2] Z. Maki,M. Nakagawa, and S. Sakata, Prog. Theor. Phys. **28** (1962) 870.

[3] Y. Fukuda *et al.*, (Super-Kamiokande Collaboration), Phys. Rev. Lett. **81** (1998) 1562-1567.

[4] Q.R. Ahmad *et al.* (SNO Collaboration), Phys. Rev. Lett. **89** (2002) 011301.

[5] C. Arpesella *et al.* (Borexino Collaboration), Phys. Lett. B **658** 101-108 (2008).

[6] K. Eguchi *et al.* (KamLAND Collaboration), Phys. Rev. Lett. **90** (2003) 021802.

[7] T. Araki *et al.* (KamLAND Collaboration), Phys. Rev. Lett. **94** (2005) 081801.

[8] K. Abe *et al.*, (Super-Kamiokande Collaboration), Phys. Rev. Lett. D **97** 072001 (2018).

[9] M. G. Aartsen *et al.*, (IceCube Collaboration), Phys. Rev. Lett. **111** (2013) 021103.

[10] A. Albert *et al.*, (The ANTARES collaboration), JHEP **6**, (2019) 113.

[11] K. Abe *et al.* (T2K Collaboration), Phys. Rev. Lett. **112** (2014) 181801.

[12] P. Adamson *et al.* (MINOS Collaboration), Phys. Rev. D. **110** (2013) 251801.

[13] P. Adamson et al. (NOVA Collaboration), Phys. Rev. Lett. 118, 151802 (2017).

[14] F.P. An *et al.* (Daya Bay Collaboration), Phys. Rev. Lett. **108** (2012) 171803.

[15] J.K. Ahn *et al.* (RENO Collaboration), Phys. Rev. Lett. **108** (2012) 191802.

[16] Y. Abe *et al.* (Double Chooz Collaboration), Phys. Rev. Lett. **108** (2012) 131801.

[17] Q.R. Ahmad *et al.*, (SNO Collaboration), Phys. Rev. Lett. **87** (2001) 071301.

[18] J. H. Choi *et al.* (RENO Collaboration), Phys. Rev. Lett. **112** (2016) 211801.

[19] G. Bak *et al.* (RENO Collaboration), Phys. Rev. Lett. **121** (2018) 201801.

[20] N. Cabibbo, Phys. Rev. Lett. **108**, 531 (1963).

[21] B. Pontecorvo,Zh. Eksp. Theo. Fiz. **34**, 247 (1957).

[22] P.A. Zyla et al. (Particle Data Group), Prog. Theor. Exp. Phys. **2020**, 083C01 (2020).

[23] B. Reinhold. "Development and Implementation of a Level-1 Trigger and Timing System for the Double Chooz Reactor Antineutrino Experiment." http://www.physik.rwth-aachen.de/institute/institut-iiib/forschung/ double-chooz/veroeffentlichungen/, 2009. PhD Thesis.

[24] C.L. Cowan Jr., F. Reines, F.B. Harrison, H.W. Kruse, and A.D. McGuire, Science, vol. **124**, no. 3212, (1956) 103104.

[25] H. Kwon *et al.* Phys. Rev. D**24** 1097, (1981).

[26] J. Vuilleumier *et al.* Phys. Lett. B**114** 298, (1982).

[27] G. K. *et al.* Phys. Lett B**138** 449, (1984).

[28] G. Zacek *et al.* Phys. Rev. D**34** 2621, (1986).

[29] A. Afonin *et al.* JETP Lett. **41** 435, (1985).

[30] A. Afonin *et al.* JETP Lett. **45** 247, (1987).

[31] A. Afonin *et al.* JETP Lett. **54** 253, (1991).

[32] G. Vidyakin *et al.* JETP Lett. **59** 390, (1994).

[33] B. Ackhar *et al.* Phys. Lett. B**338** 383, (1994).

[34] Chooz Collaboration, M. Apollonio *et al.* Phys. Lett. B**420** 397, hep-ex/9907037, (1998).

[35] Palo Verde Collaboration, F. Boehm *et al.* Prog. Part. Nucl. Phys. **40** 253, (1998).

[36] Palo Verde Collaboration, F. Boehm *et al.* Phys. Rev. D**64** 112001, (2001).

[37] S.G. Yoon *et al.* (RENO Collaboration), Phys. Rev. D. **104** (2021) L111301.

[38] F.P. An *et al.* (Daya Bay Collaboration), Chinese Phys. C. **45** 073001 (2012).

[39] H.de Kerret *et al.* (Double Chooz Collaboration), Nat. Phys. **16** 558-564 (2020).

[40] Palo Verde Collaboration, Boehm, *et al.*, Physical Review Letters **84** (2000) 3764.

[41] Palo Verde Collaboration, Boehm, *et al.*, Physical Review D **62** (2000) 072002.

[42] Yeh M, Garnov A, Hahn RL. Nucl. Instrum. Methods A **578**:329 (2007).

[43] Park JS, *et al.* (RENO Collab.) Nucl. Instrum. Methods A **707**:45 (2013).

[44] Beriguete W, *et al.* Nucl. Instrum. Methods A **763**:82 (2014).

[45] K. Schreckenbach, G. Colvin, W. Gelletly, and F. Von Feilitzsch, Phys. Lett. B **160**, 325 (1985).

[46] A. A. Hahn *et al.*, Phys. Lett. B **218**, 365 (1989).

[47] H. V. Klapdor and J. Metzinger, Phys. Rev. Lett. **48**, 127 (1982).

[48] P. Vogel, G. K. Schenter, F. M. Mann, and R. E. Schenter, Phys. Rev. C **24**, 1543 (1981).

[49] V. I. Kopeikin, Preprint Kurchatov Institute of Atomic Energy, Moscow IAE-4305/2 (1998).

[50] See a talk given by Larstem Heeger at UW undergraduate colloquium in Feb. 27, 2013.

[51] P. Huber and T. Schwetz, Phys. Rev. D **70**, 053011 (2004).

[52] P. Vogel and J. Engel, Phys. Rev. D **39**, 3378 (1989).

[53] Xin Qian and Jen-Chieh Peng, Rep. Prog. Phys. **82** (2019) 036201.

[54] P. Vogel and J. Beacom, Phys. Rev. D 60, 053003 (1999).

[55] D. H. Wilkinson, Nucl. Phys. A**377**, 474 (1982).

[56] Vogel P, Wen L and Zhang C 2015 Nat. Commun. **6**, 6935.

[57] H. Minakata and S. Watanabe, Phys. Lett. B 468, 256 (1999).

[58] H. Minakata et al., Phys. Rev. D 70, 059901 (E) (2004).

[59] H. Nunokawa, S. Parke, and R. Zukanovich Funchal, Phys. Rev. D **72**, (2005) 013009.

[60] K. Anderson *et al.*, "White paper report on using nuclear reactors to search for a value of $\theta 13$" (2004), hep-ex/0402041.

[61] M. Freund, P. Huber and M. Lindner, Nucl. Phys. B**615**, 331-357 (2001).

[62] Kettell S, *et al.* arXiv:1307.7419 [hep-ex] (2013).

[63] Abe K, *et al.* (T2K Collaboration) Phys. Rev. Lett. **112**:061802 (2014).

[64] Shin, C.D., Atif, Z. et al. (The RENO collaboration), J. High Energ. Phys. 2020, 29 (2020).

[65] T. Mueller at. al., Phys. Rev. C 83, 054615 (2011).

[66] P. Huber, Phys. Rev. C 84, 024617 (2011).

[67] S.H. Seo *et al.* (RENO Collaboration), Phys. Rev. D 98. 012002 (2018).

[68] Kim H.S. NPSM. 631 635, 62 (2012).

[69] H. de Kerret et al. (Double Chooz Collaboration), JHEP **11**, (2018) 53.

[70] C. Bemporad, G. Gratta, and P. Vogel, Rev. Mod. Phys. **74**, 297 (2002).

[71] K.S. Park *et al.* (RENO Collaboration), Nucl. Instrum. Methods A **686** (2012) 91-99 .

[72] T. Mueller at. al., Phys. Rev. C **83**, 054615 (2011).

[73] M. Freund, P. Huber and M. Lindner, Nucl. Phys. B**615**, 331-357 (2001).

[74] G. L. Fogli, L. Lisi, A. Marrone, D. Montanino, and A. Palazzo, Phys. Rev. D **66**, 053010 (2002).

[75] Daya Bay, F. P. An et al., Phys. Rev. D 93, 072011 JHEP 01, 163 (2016).

[76] Double Chooz, Y. Abe et al., Phys. Rev. D 93, 072011 (2016).

국문초록

Measurement of the smallest neutrino mixing angle using reactor antineutrino events with neutron capture on hydrogen at RENO

김상용
물리천문학부 물리학전공
서울대학교 대학원

The reactor experiment for neutrino oscillation (RENO) 는 중성미자의 가장 작은 섞임각으로 알려진 $\theta_1 3$을 영광에 위치한 한빛 원자력발전소에서 나오는 반전자 중성미자를 검출을 통해 성공적으로 측정했다. 2011년 8월부터 발전소 근처에 위치한 두개의 동일한 검출기를 사용하여 발전소로부터 나오는 중성미자의 총량에대한 오차를 상쇄하여 검출기의 계통오차를 크게 줄이는 방법으로 전자 반중성미자의 데이터를 받기 시작했다. 각각의 RENO 검출기는 4겹의 실리더 형태로 각기 다른 액체를 담은 섬광용액 검출기로 가장 안쪽부터 타겟, 감마캐쳐, 버퍼, 비토 검출기로 구성되어 있다. 0.1 %의 희토류 금속인 가돌리늄을 중화반응을 통해 섬광용액에 녹인 16톤의 타겟과 타겟밖으로 나온 감마선을 완전히 잡기위한 28톤의 섬광용액으로만 구성된 감마캐쳐에 있는 자유 양성자가 원자로에서 나오는 반전자 중성미자와 상호작용을 하여 IBD(Inverse beta decay) 이벤트로 검출된다. 지하 시설인 RENO 검출기는 주변 암반 뿐아니라 검출기를 구성하는 섬광용액과 아크릴, 그리고 PMT 등으로부터 ∼3.5 MeV 이하의 환경 방사능이 존재하여 IBD 신호를 검출하는데 방해가되는 배경사건 신호가 된다. 타겟영역에서 상호작용후 나오는 중성자가 가돌리늄에 포획되어 약 28 μs 의 평균 지연 신호로 8 MeV 의 높은 에너지 신호로 검출되는 가돌리늄 이벤트(n-Gd)와는 달리, 타겟과 감마캐쳐 영역에서 수소에 포획되어 나오는 이벤트(n-H)는 2.223 MeV 에너지와 약 $\sim 200\mu$s 의 평균 지연 신호로 검출되기때문에 상당한 배경사건 신호를 가진다. 성공적으로 중성미자의 섞임각 $\theta_1 3$를 측정한 n-Gd 데이터와 마찬가지로 n-H 데이터를 통해서도 독립적인 $\theta_1 3$ 측정이 가능하다. n-Gd 데이터의 타겟 크기보다 약 2배에 달하는 크기로 측정이가능하지만 n-Gd 검출 효율보다 절반에 가까운 검출 효율을 가지는 n-H 데이터는 n-Gd와 대등한 데이터 통계치를 가지기때문에 IBD 이벤트 검출 기준을 더욱 엄격하게 하고 배경사건 신호를 제거하는 분석 알고리즘을 계속해서 개발함과 동시에 검출기 교정과 flasher 이벤트를 효율적으로 제거하는 방법 등을 개발하여 n-H 데이터를 통한 섞임각 $\theta_1 3$를 성공적으로 측정하였다. 이 n-H 데이터를 통한 독립적인 측정을 통해 RENO 실험에서 n-Gd 데이터 분석 결과에 대한 대조 검사가 될 수 있고, 또한 검출기 계통 오차에대한 일관성 조사까지 할 수 있다. 원,근거리 검출 이벤트 수 비교 분석을 통해 얻은 결과는 $\sin^2 2\theta_{13} = 0.086 \pm 0.006(\text{stat.}) \pm 0.010(\text{syst.})$ 로 본 논문은 이 측정에 대한 분석 방법과 그 결과들을 기술하였다.